Master Thesis

Modeling and Simulation of Superelastic Lattice Structures

carried out for the purpose of obtaining the degree of Diplom-Ingenieur (Dipl.-Ing.)

submitted at TU Wien

Faculty of Mechanical and Industrial Engineering

by

Tim Munhowen, BSc

Mat.Nr.:01615514

under the supervision of

Associate Prof. Dipl.-Ing Dr.techn. H. E. Pettermann

Associate Prof. Dipl.-Ing.in Dr.in techn. M. Todt

Institute of Lightweight Design and Structural Biomechanics, E317

Vienna, February 2025

This work has been supported by the European Union Programme Horizon Europe under Grant Agreement No. 10107909 within the framework of the project "Building Actions in Smart Aviation with Environmental Gains".

I confirm, that the printing of this thesis requires the approval of the examination board.

Affidavit

I declare in lieu of oath, that I wrote this thesis and carried out the associated research myself, using only the literature cited in this volume. If text passages from sources are used literally, they are marked as such.

I confirm that this work is original and has not been submitted for examination elsewhere, nor is it currently under consideration for a thesis elsewhere. I acknowledge that the submitted work will be checked electronically-technically using suitable and state-of-the-art means (plagiarism detection software). On the one hand, this ensures that the submitted work was prepared according to the high-quality standards within the applicable rules to ensure good scientific practice "Code of Conduct" at the TU Wien. On the other hand, a comparison with other student theses avoids violations of my personal copyright.

Vienna, February 2025 _____

Contents

Abstract

Superelasticity is a prominent effect in shape memory alloys that enables the recovery of large amounts of strains initially induced by mechanical loads. To predict the influence of superelastic parent material in lattice structures with the aid of the Finite Element method, reliable constitutive material models are required. The aim of this thesis is the verification of a uniaxial hypoelastic material model developed for simulating beam-modeled lattice structures with experimentally determined superelastic material properties. The verification process is based on comparisons with a well established material model for superelasticity. The modeling strategies of three different unit cell designs are presented, and numerical analyses are conducted on them for the load case of uniaxial tension and pure shear. The results of the numerical simulations show that the investigated uniaxial hypoelastic material model is well suited for the analysis of lattice structures of superelastic material. The material model provides a straightforward calibration with a direct link to the experimental data. It is therefore an effective solution for research fields such as additive manufacturing of lattice structures in which frequent shifts of material properties need to be handled, when different processing parameters are investigated.

Kurzfassung

Superelastizität ist eine charakteristische Eigenschaft von Formgedächtnislegierungen, welche die Reversibilität großer Dehnungen, deren Ursprung in mechanischen Belastungen liegt, ermöglicht. Um den Einfluss von superelastischem Material in Gitterstrukturen mit Hilfe der Finite-Elemente-Methode vorherzusagen, benötigt es zuverlässige Konstitutivgesetze. Das Ziel dieser Arbeit ist die Verifikation eines einachsigen hypoelastischen Materialmodells, welches zur Simulation balkenmodellierter Gitterstrukturen entwickelt wurde, deren superelastischen Materialeigenschaften auf experimentell erfassten Daten basiert. Der Verifikationsprozess basiert auf Vergleichen mit einem etablierten Materialmodell für Superelastizität. Die Modellierungsstrategien von drei verschiedenen Variationen von Elementarzellen werden präsentiert, sowie numerische Analysen für den Lastfall des einachsigen Zuges und der reinen Scherung durchgeführt. Die Ergebnisse der numerischen Simulationen zeigen, dass das untersuchte uniaxiale hypoelastische Materialmodell gut für die Analyse von Gitterstrukturen superelastischer Materialien geeignet ist. Das Materialmodell ermöglicht eine unkomplizierte Kalibrierung und ist daher eine effektive Lösung für Forschungsbereiche wie dem 3D-Druck von Gitterstrukturen, bei dem es bei der Untersuchung verschiedener Verarbeitungsparameter oft zu Änderungen der Materialeigenschaften kommt und daher häufige Kalibrierungen des Materialmodells erforderlich sind.

List of Figures

List of Tables

List of Symbols

c_r	critical point as the intersection of both upper limits of stress and temperature
T_d	upper temperature limit for phase transformations
A_f	austenite finish temperature
σ_{tL}^S	stress at which the transformation starts during loading in tension
σ_{tL}^E	stress at which the transformation ends during loading in tension
σ_{tU}^S	stress at which the reverse transformation starts during unloading in tension
σ_{tU}^E	stress at which the reverse transformation ends during unloading in tension
E_A	Young's modulus of the austenite phase
ν_A	Poisson ratio of the austenite phase
E_M	Young's modulus of the martensite phase
ν_M	Poisson ratio of the martensite phase
ε_t	transformation strain
σ_{cL}^S	stress at which the transformation starts during loading in compression
T_0	reference temperature
$E_{tL;T}$	Young's Modulus in the transformation regime (loading)
$E_{tU;T}$	Young's Modulus in the transformation regime (unloading)

List of Acronyms

cASM	*ABAQUS* standard material model for superelasticity applied on a model comprising exclusively continuum elements
bASM	*ABAQUS* standard material model for superelasticity applied on a model comprising exclusively beam elements
UHYP-POLY	hypoelastic polynomial fitted material model for superelasticity
UHYP-MLIN	hypoelastic multilinear material model for superelasticity
ASM	*ABAQUS* standard material model for superelasticity
`UHYPEL`	hypoelastic user-subroutine
CAD	computer aided design
FEM	finite element method
SMA	shape memory alloy
NiTi	nickel titanium alloy
PBF	powder bed fusion
SLM	selective laser melting
LPBF	laser powder bed fusion

1 Introduction

1.1 Background

The evolution of engineered structures is closely related to breakthroughs in the fields of material science, numerical methods, and manufacturing technologies. Over the last decades, each of those fields has seen considerable progress, with one of them specifically standing out, the field of manufacturing technologies.
The recent leaps in development of additive manufacturing methods in conjunction with the rise in computing power have sparked new interest in the advancement of lightweight structures through the use of lattice materials.

Lattice materials are cellular structures that consist of a large number of uniform lattice elements (e.g. slender beams or rods) and are generated by tessellating a unit cell, often periodically, throughout space [1]. This repeating unit cell is the building block of the lattice material and is characterized by the dimension, arrangement, and connectivity of its lattice elements [2]. This means that a great multitude of different unit cell topologies and geometries are possible, and thus also lattice materials.
At the scale of the unit cells, the lattice material shows typical structural behavior in terms of properties and features; however, on the macroscopic length scale, the lattice material is considered to be like a homogeneous material.
The fact that the option of different lattice material parameters is so vast means that a plethora of different variations of lattice material is possible, each with custom-tailored physical properties unlike those of its parent material. To name a few, the properties can come in the form of high strength to weight ratio, auxeticity [3] (i.e. material with a negative Poisson ratio), thermal conductivity [4], porosity [5], high energy absorption [6] and many more. Thus, they are especially commercially attractive in fields of engineering where functionality and low weight are key, such as biomedical engineering and aerospace.
In general, a lattice material is usually designed using CAD-software and then analysed using the Finite Element Method (FEM). The combination of lattice materials

and additive manufacturing has not only revolutionized the achievable complexity of the lattices but also motivated the reassessment of formerly disfavored alloys. Namely, alloys whose manufacturing was considered too difficult and wasteful with traditional manufacturing methods have now regained the interest of many researchers. One type of these materials are the shape memory alloys (SMA), more specifically, the Nickel Titanium (NiTi) alloys.

NiTi alloys are mostly known for two unique characteristics, (1) the *shape-memory effect* and (2) *superelasticity*. While the exploitation of the former has resulted in many interesting engineering applications, the present work is focused on the latter. Superelasticity, or pseudoelasticity, is based on athermal stress-induced phase transformations, which allow large reversible deformations. The phenomenon of superelasticity is difficult to capture correctly and if it is to be implemented as a parent material for lattices in FEM, adequate material models are required which are capable of handling the deformation mechanisms of the lattice microstructure, as well as the material response of the NiTi alloy [7]. Moreover, processing parameters and thermal treatments in additive manufacturing have a significant influence on the resulting material behavior of the produced sample, which means that significant deviations from the idealized constitutive relations of the parent material are to be expected. As a result, an additional requirement arises which is to be fulfilled by the material model, i.e. the model must be capable to handle experimentally captured material data.

1.2 Motivation

In the paper authored by Schasching et al. [7] a hypoelastic material model for beam elements which aims to predict the superelastic material response of additive manufactured lattices is proposed, and a corresponding verification of said material model provided.
In the present work, the verification of the material model is extended with the aid of the Finite Element Method by applying it on lattices with more complex unit cell designs. Simulations are performed on three different unit cell designs and their respective modeling strategies are presented. To verify the modeling strategies and the material model, simulations are performed with (1) the hypoelastic material model presented in [7], (2) a second hypoelastic material model which is a less refined version of the first, and (3) the material model integrated in *ABAQUS* 2023/Standard (*Dassault Systèmes Simulia Corp., Providence, RI, USA*) which is based on the works of Auricchio et al. [8], [9].

By extending the field of use for this material model, a more efficient way of analysing lattices with superelastic material based on beam elements is established. This not only reduces the required computational power but also speeds up the unit cell modeling, which facilitates further research in the field of additive manufactured lattices with superelastic material, as there, flexible material models are needed due to the vast amount of possible processing parameters.

1.3 Scope of the Thesis

To verify the hypoelastic material model from the work of Schasching et al. [7], a second hypoelastic model, which has also been developed by them and is a de facto less refined predecessor, is included in the comparisons. Here, it is used primarily as a "stepping stone" to bridge the comparisons between the *ABAQUS* material model and the hypoelastic model from the paper, as it is designed on the basis of a similar principle.
It is to be noted that for all the simulations conducted in this work, plane stress assumptions are made. Furthermore, the material data used for the simulations are limited to NiTi-based alloy, and are derived from experimental data captured by project partners at the Insitute of Machine and Industrial Design, Brno University of Technology.
To calculate the stress-strain response of the lattice material, two approximations are made. First, a homogenization method in the form of the periodic microfield approach is applied. Second, to evaluate the homogenized stress-strain response of the lattice structure, a method based on linear homogenizations is utilized. A more detailed look at that method is provided later in Section 2.2.

1.4 Outline of the Thesis

Chapter 2 provides the necessary theory on the periodic microfield approach including the symmetry and periodicity boundary conditions. After that, an in-depth look at superelasticity is provided. Moreover, the topic of plane stress is briefly outlined and the differences between pure and simple shear are presented. Then, the three material models for superelasticity are discussed. The last section of Chapter 2 covers the topic of bifurcation of equilibrium.
In Chapter 3, the geometry of the unit cell from which three different variants are derived is presented. Furthermore, the modeling strategies of each variant of the unit cells are outlined. Information is provided on the material parameters that are then used for subsequent analyses. In addition, Chapter 3 includes a detailed description of the load cases and the corresponding boundary conditions.

Chapter 4 presents the results of the analyses, which are also briefly discussed. Lastly, Chapter 5 consists of the conclusion of the thesis.

1.5 Literature Review

The aim of this section is to provide a useful guide on the literature of the research fields connected to the underlying topics of this master thesis. The main findings of several papers are briefly outlined and knowledge gaps highlighted.

A broad overview of the state of the art in metal additive manufacturing is given in the review by Tebianian et al. [10]. Most notably, different types of powder bed fusion (PBF) methods are presented, including selective laser melting (SLM), which is the primary additive manufacturing method used for the fabrication of NiTi alloy structures.

On the subject of shape memory alloys, the book by Concilio et al. [11] serves as an excellent starting literature to gain a solid understanding of shape memory alloys. It covers the essential topics such as the characteristics, applications and manufacturing methods of NiTi. In addition, it also tackles more specific themes, such as the experimental setup needed for the capture of the properties of SMA's and gives an overview of the currently existing constitutive models for shape memory alloys. For supplementary information on the mechanics that cause the superelastic effect, the paper by Tsuchiya [12], the article by Petrini et al. [13], and the lecture notes by Mayrhofer [14] provide good explanations.

The connection between both fields, shape memory alloys and additive manufacturing technologies, is provided in the work of Elahnia et al. [15]. In their review, insights on the processing of NiTi through additive manufacturing methods are given. Safaei et al. [16] focus in their work on the fabrication of NiTi alloys with the laser powder bed fusion technique (LPBF) and outline its potential in biomedical applications. Moghaddam et al. [17] discuss the effects of the process parameters of selective laser melting (SLM) on the superelastic behavior of additively manufactured NiTi and propose a method to improve the superelasticity in compression of as-fabricated NiTi.

A good introduction to lattice materials is given in the work of Fleck et al. [1]. They provide a definition of lattice materials and establish an understanding of the characteristics of the lattice materials with the use of material property charts. Maconachie et al. [2] cover in their review of selective laser-melted lattice materials different types of lattice structures, which are commonly fabricated with the said

manufacturing method. Furthermore, they mention the fields of application, as well as the mechanical properties and microstructure of SLM components.

The modeling strategies used in this work are based on the periodic microfield approach, a micromechanical concept used to homogenize the properties of heterogeneous material. An overview of this multiscale approach, with an emphasis on the field of lattice materials that comprise repeated unit cells, is provided by Böhm [18]. The book includes, most notably, the implementation of the underlying boundary conditions, the requirements, and the limits of their applicability.

In this work, uniaxial tension and pure shear load cases are carried out to verify both the modeling technique and the material models. The book on continuum mechanics by Anand et al. [19] provides the basics on pure shear and how it differs from simple shear. For a more detailed look at the topic, the article by Thiel et al. [20] serves as a good supplementary source, as here the difference between infinitesimal and finite strains and their effect on the properties of shear deformations is presented.

The topic of beam buckling is shortly outlined in this thesis, as this type of instability is encountered for one of the loading scenarios used for the verification process. The book by Luongo et al. [21], more specifically Chapter 2 of that book, offers good introductory literature on the topics of equilibrium of stability and bifurcation. Albeit just a small part of the lecture notes of the course *Non-Linear Finite Elements* by Todt [22], the literature includes nonetheless, qualitative illustrations and explanations on the topic of instabilities. Furthermore, valuable tips on how to approach the problem in the context of a finite element analysis are included which deemed helpful in this thesis.

The literature on existing material models for shape memory alloys is quite extensive. An overview of the currently existing material models is given in the review by Cisse et al. [23]. They categorize them into microscopic thermodynamic models, micro-macro models and macroscopic models. Their review makes clear that the mathematical implementation of the superelastic material behavior is no easy task. In addition, all the material models that are based on different concepts also differ from each other in terms of calibration methods, since each may require different parameters. The practicability to capture those parameters and calibrate the corresponding material models is an issue which is not addressed by many researchers. This issue is partially addressed in the work of Schasching et al. [7] as they propose a material model that is easier to calibrate. Their model is a uniaxial hypoelastic constitutive material model for superelasticity. Their aim is to specifically facilitate further studies of

additively manufactured lattices of superelastic material, where frequent calibration is needed due to the influence of the process parameters on the behavior of the material. The model works exclusively with beam elements, which makes it favorable for the design of large and complex lattice structures. The stress-strain response is described using third-order and linear polynomials.
As a means of verification, they compare their material model with the superelasticity material model built into the commercial software package *ABAQUS* . This material model is based on the work of Auriccio et al. [8], [9].
As a result, the original model by Auricchio et al. shall be mentioned too, as it still has a significant impact on the development of many material models since the publication of their work [8]. Their constitutive material model is capable of handling superelasticity at finite strains with different behavior in tension and compression.
To further highlight the great number of different approaches, the paper of Junker and Hackl [24] is mentioned, in which the development of a purely energy-based material model is presented. They show examples of a functioning finite element implementation of their model and discuss the ways of capturing the parameters needed for the calibration of their model.

Despite the great number of existing material models for shape memory alloys, their applicability for the testing of additive manufactured lattice structures seems restricted. Many material models suffer from two main issues: (1) their parameters are too difficult to capture and (2) the model is not flexible enough to account for material defects resulting from the complex thermal history of additively manufactured structures. Both issues are problematic when different sets of processing parameters are tested, a common practice in additive manufacturing.

2 Theoretical Background

2.1 Periodic Microfields and Unit Cells

Lattice-based structures have been investigated extensively for decades. They gain their unique characteristics from internal substructures, so-called unit cells. These building blocks are what makes lattice structures so special, as their topology and arrangement within the lattice are the roots for the characteristics of the overall lattice structures. Some of these characteristics can come in the form of improvement in structural integrity, introduction of desired anisotropy, and reduction of weight. An example of an infinite lattice structure with a periodically repeating unit cell is illustrated in Figure 2.1.

Since the geometrical complexity of the unit cells can be significant, modeling and analyzing entire lattice structures with the finite element method has become challenging. To capture detailed information on the mechanical response of the structure, a sufficiently small element size must be chosen, leading to high computational costs. Therefore, it rarely makes sense to model the lattice structure as a whole, but approximation methods are needed. In most cases, for this, homogenization methods are used.

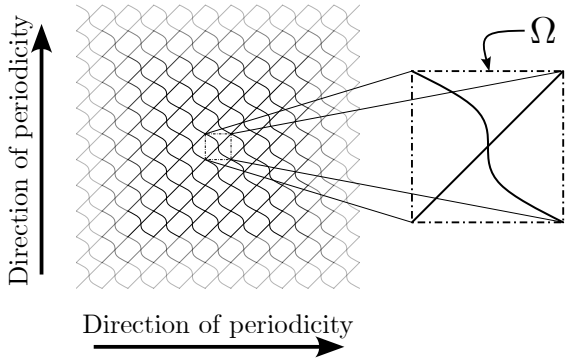

Figure 2.1: Infinite lattice structure with a detailed view of the unit cell. The border domain of the unit cell is denoted with Ω.

Homogenization methods are multiscale methods that link different length scales, which means that effective properties of the macroscopic structure are deduced from the behavior of the microstructure.
To achieve homogenized stresses and strains, two conditions must be met, (1) the tractions at the unit cell interface must be continuous and (2) the deformations must be compatible, meaning neither separation nor overlapping between two neighboring cells must occur.
Since in this work lattice structures with periodically repeating unit cells are investigated, a homogenization method specialized on a periodic medium suffices. Therefore, the periodic microfield approach is utilized to evaluate the lattice structure.
The periodic microfield approach is an approximation method, based on the assumption of uniform macrofields, that makes use of the internal periodic structure of the lattice. Only a small domain, the unit cell, is investigated, which then provides information about the properties of the entire domain, i.e. the lattice structure. This homogenization method has the great advantage of significantly reducing the computational effort and thus allowing for greater design freedom. Since the fundamentals of the periodic microfield approach are based on the periodic characteristics of the observed domain, the boundary conditions of the unit cell must be set accordingly to ensure an accurate representation.
Three different types of boundary conditions exist that are used to meet these requirements. It is differentiated between (1) the periodicity boundary conditions, (2) the symmetry boundary conditions, and (3) the antisymmetry boundary conditions [18]. In this work, only the first two of the listed boundary conditions are used and thus presented.
To properly describe them, a notation system based on the four cardinal directions is introduced. In the following figure 2.2, a quadrilateral two-dimensional unit cell is shown. The four edges are denoted by the letters S (South), N (North), W (West), and E (East). The notation of the corner points of the quadrilaterial unit cell is determined by the two intersecting edges, meaning the corner point lying at the intersection of edge S and edge E is denoted by SE.

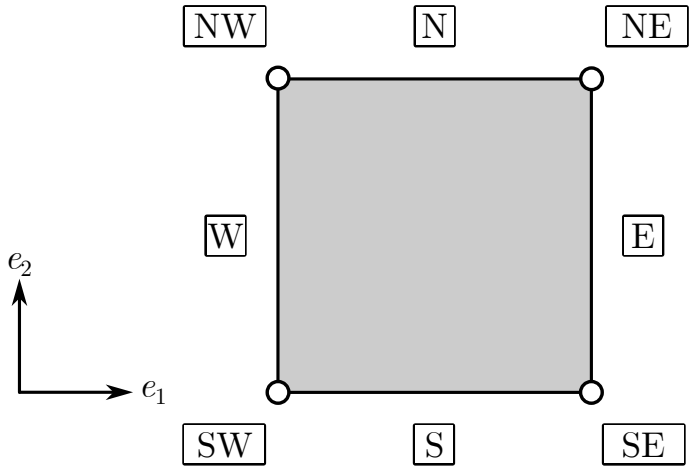

Figure 2.2: Notation system on the basis of the four cardinal directions for a quadrilateral two-dimensional unit cell.

2.1.1 Periodicity Boundary Condition

The periodicity boundary condition is the most general boundary condition for unit cells, as it can handle all kinds of deformation [18]. To ensure homogenized stresses and strains, the regions of the unit cell lying on opposing sides of the boundary Ω, that is, the boundary surrounding the unit cell (see Figure 2.1), must be paired in a way such that they always remain identical in arrangement, shape, and size. In terms of finite element implementation, the paired regions must be meshed identically with equivalent number of nodes and nodal position, ensuring node alignment and thus nodal compatibility among said regions. The mathematical implementation of the periodicity boundary conditions for a quadrilateral two-dimensional unit cell reads

$$\underline{\mathbf{u}}_N(l_1) = \underline{\mathbf{u}}_S(l_1) + \underline{\mathbf{u}}_{NW} \tag{2.1}$$

$$\underline{\mathbf{u}}_E(l_2) = \underline{\mathbf{u}}_W(l_2) + \underline{\mathbf{u}}_{SE} \tag{2.2}$$

$$\underline{\mathbf{u}}_{NE} = \underline{\mathbf{u}}_{NW} + \underline{\mathbf{u}}_{SE} \tag{2.3}$$

where $\underline{\mathbf{u}}$ are periodically varying microscopic displacement vectors at the unit cell boundaries, and l_1, l_2 are parameters describing the lateral coordinate with respect to the 1- and 2-axis. The relation between the displacements of the nodes and edges of the unit cell is described by a "leader-follower" link, i.e. the "leader" determines the displacement of the "follower". As described in Equations (2.1) - (2.3), the "leader edges" and "leader nodes" are S, W, NW, and SE, respectively. Whereas, the "follower edges" and "follower nodes", with regard to the in-plane degrees of freedom, are N, E, and NE. A visual representation of the periodicity boundary conditions is shown in Figure 2.3. The "leader edges" S and W with the "leader nodes" NW and SE dictate the displacement of the "follower edges" N and E as well

as the "follower node" NE. This pairing of edges and nodes ensures that neighboring cells avoid overlapping or the formation of holes, leading to compatible deformations across the unit cell boundary.
In the case of a discretization of the unit cell using structural elements (e.g. beam elements or shell elements), the periodicity boundary conditions must be extended for the rotational degrees of freedom which is expressed through

$$\underline{\mathbf{u}}_{R3|N}(l_1) = \underline{\mathbf{u}}_{R3|S}(l_1) \tag{2.4}$$

$$\underline{\mathbf{u}}_{R3|E}(l_2) = \underline{\mathbf{u}}_{R3|W}(l_2) \tag{2.5}$$

This effectively means that the nodes of the "leader edges", S and W, dictate their rotations to their opposing counterparts, lying on the "follower edges", N and E.
In terms of FEM implementation, these boundary conditions can be realized as linear constraint equations between individual degrees of freedom [18].

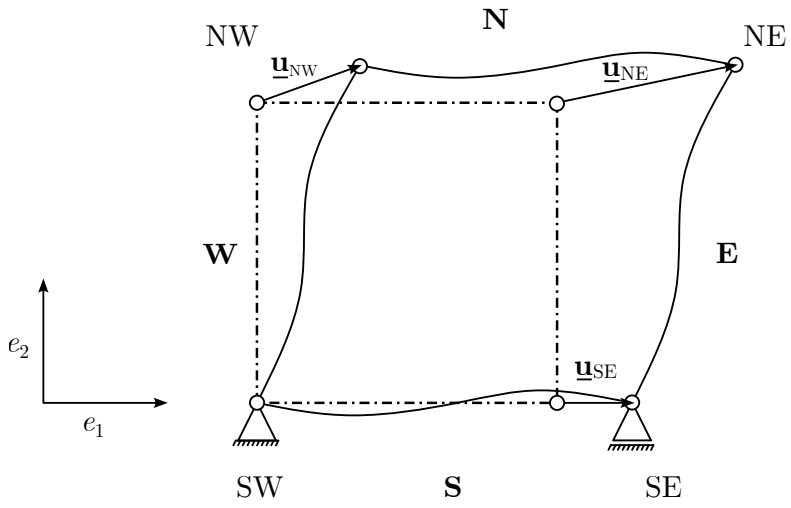

Figure 2.3: Deformed quadrilateral two-dimensional unit cell with periodicity boundary conditions. The dash-dotted square represents the unit cell in its undeformed state. Taken from Reference [18].

2.1.2 Symmetry Boundary Condition

A less general type of boundary condition is the symmetry boundary condition. This type of boundary condition is more restricted in its field of use, as it can only be applied to unit cells with rectangular or hexahedral geometries, where the internal microstructure is mirrored [18]. Furthermore, only mechanical loads that act in directions normal to one or more pairs of edges, and combinations of the above can be handled by the symmetry boundary conditions. Despite these limitations, the symmetry boundary conditions are nonetheless useful in numerous tasks [18]. The symmetry boundary conditions for a two-dimensional quadrilateral unit cell are given as

$$\underline{\mathbf{u}}_{1|E}(l_2) = \underline{\mathbf{u}}_{1|SE} \tag{2.6}$$

$$\underline{\mathbf{u}}_{2|N}(l_1) = \underline{\mathbf{u}}_{2|NW} \tag{2.7}$$

$$\underline{\mathbf{u}}_{1|W}(l_2) = 0 \tag{2.8}$$

$$\underline{\mathbf{u}}_{2|S}(l_1) = 0. \tag{2.9}$$

A "leader-follower" link is here established too. The "leader node" SE determines the horizontal displacement of the "follower edge" E, whereas the node NW dictates the vertical displacement of the edge N. Furthermore, the degree of freedom in the 1-direction of Edge W is locked, as well as the degree of freedom in the 2-direction of S. Schematically, these relations are presented in Figure 2.4.
In the same sense as for the periodicity boundary conditions the usage of structural elements for the discretization necessitates an extension of the symmetry boundary conditions which reads

$$\underline{\mathbf{u}}_{R3|N}(l_1) = \underline{\mathbf{u}}_{R3|S}(l_1) = 0 \tag{2.10}$$

$$\underline{\mathbf{u}}_{R3|E}(l_2) = \underline{\mathbf{u}}_{R3|W}(l_2) = 0 \tag{2.11}$$

and thus locks the rotations of all nodes lying on the border domain Ω.

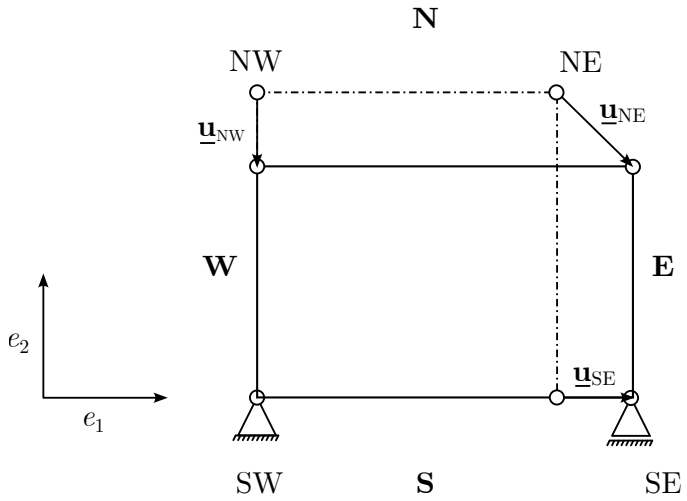

Figure 2.4: Deformed quadrilateral two-dimensional unit cell with symmetry boundary conditions. The dash-dotted square represents the unit cell in its undeformed state. Taken from Reference [18].

2.2 Stress and Strain Calculation Method for Lattice Structures

When it comes to understanding the mechanical behavior of lattice structures, the stress-strain curve is a valuable metric that provides a visualization of the beginning and end of specific regimes, e.g., linear-elastic regimes, start of plastic yielding. More specifically, in the case of superelastic material, it helps to understand and identify the beginning and end of the martensitic transformation. Since superelastic material implies complex material behavior, the stresses and strains of the lattice structures in this work are evaluated with the aid of the Finite Element method using a method based on linear homogenizations. Furthermore, by applying the periodic microfield approach, the determination of the average stresses of a single unit cell suffices. For the case of uniaxial tension they read

$$\sigma_{ii} = \frac{F_{R,i}}{A_i} \tag{2.12}$$

where σ_{ii} is the nominal stress, $F_{R,i}$ are the reaction forces of the "leader node", and A_i the undeformed cross-sectional area lying on the plane with normal vector $\underline{\mathbf{n}}_i$. The subscripts i, j, k refer to the reference coordinate system with the base vectors $\underline{\mathbf{e}}_i$, $\underline{\mathbf{e}}_j$.
The average normal strains are determined via

$$\varepsilon_{ii} = \frac{u_i}{L_i} \tag{2.13}$$

where u_i is the deformation of the "leader node" and L_i is the original length of the unit cell.
Regarding the determination of the average pure shear stresses, the equation reads

$$\sigma_{ij} = \sigma_{ji} = \frac{F_{R,i}}{A_j} = \frac{F_{R,j}}{A_i} \tag{2.14}$$

and the average pure shear strains are expressed through

$$\varepsilon_{ij} = \frac{1}{2}\left(\arctan\left(\frac{u_i}{L_j}\right) + \arctan\left(\frac{u_j}{L_i}\right)\right). \tag{2.15}$$

2.3 Superelasticity in Shape Memory Alloys

Shape memory alloys play a significant role in the fields of aerospace, structural, and biomedical engineering [11] due to their use as functional metallic material. They are the cause of many new devices or further improvements of already existing ones. Their attributes, which allow for the exploration of these new technologies, are the *shape memory effect* and the *superelasticity* (also referred to as pseudoelasticity [13]). The shape memory effect allows for so-called smart materials, capable of returning from their deformed state back to their original shape when exposed to a thermal excursion. In contrast, the superelastic effect is an isothermal process allowing for reversible deformations of up to eight percent strain [12], [11]. Both effects rely on the microstructural properties of the alloy and are a direct result of solid-solid diffusionless phase transformations between the martensite and the austenite phase. Austenite is a high-temperature phase which is often referred to as the parent phase. It has a body-centered cubic crystal structure and is usually unstable at room temperature. However, it can be stabilized by slightly changing the atomic composition of the alloy. In the case of NiTi alloys, the alloy chosen in this work for the verification of the material models, this is achieved by increasing the amount of nickel beyond 50 at.% [25]. The result is a reduction of the austenite finish temperature, the temperature at which the metallic phase consists of only austenite. The martensite phase is lower in symmetry compared to austenite, as it has a tetragonal, orthorhombic, or monoclinic crystal structure. This means that martensite can comprise a wide variety of different crystallographically equivalent variants. Furthermore, the microstructure of martensite has been observed in two forms: twinned and detwinned. Twinned martensite forms through a combination of self-accomodated martensitic variants and is a key factor in the shape memory effect. Detwinned martensite is characterized by a predominant specific variant [11].

A successful martensitic transformation and, thus, superelasticity require the presence of a certain compatibility between the crystal structures of both phases. The typical microstructures of NiTi are shown in Figure 2.5, which confirms compatibility. The austenite phase is represented with its body-centered cubic (bcc) (β) crystal structure and the martensite phase with a monoclinic (α) microstructure [14].

Although superelasticity is the result of an isothermal time-independent process, temperature levels and intervals play a crucial role [11]. The martensitic transformation is a diffusionless process, which means that the temperature range in which the transformation takes place is important, as it must be in a range in which atomic diffusion takes longer than the martensitic transformation, making the latter the favored mechanism [14].

Secondly, the transformation stress that initiates the diffusionless process also de-

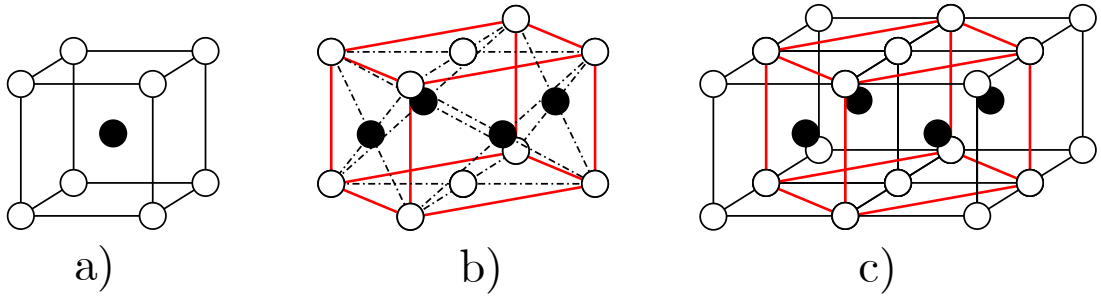

Figure 2.5: Proof of compatibility between the bcc and monoclin crystal structure of NiTi. The white atoms are Ni and the black filled atoms are Ti. a) Austenite phase of NiTi with a bcc crystal structure. b) Martensite phase of NiTi with a monoclin crystal structure. c) Proof of compatibility between bcc and monoclin crystal structure of NiTi. Adapted from Reference [14].

pends on the temperature level, as illustrated in Figure 2.6. More specifically, the stress necessary to start the forward and back transformation increases linearly with temperature. However, a certain threshold of stress and temperature should not be exceeded. Otherwise, the deformation is caused by dislocation movement. Hence, the alloy will deform plastically and no superelastic effect will occur. This critical point c_r is marked in Figure 2.6 as the intersection of the upper stress limit and the upper temperature limit for phase transformations T_d. Moreover, if the temperature is too low and falls below A_f, the stress-induced martensite does not fully revert back to austenite and some residual strain remains in the material [12].
For reasons of clarity, the information presented is summarized with the shaded area in Figure 2.6. It represents the region in which the superelastic effect is guaranteed.

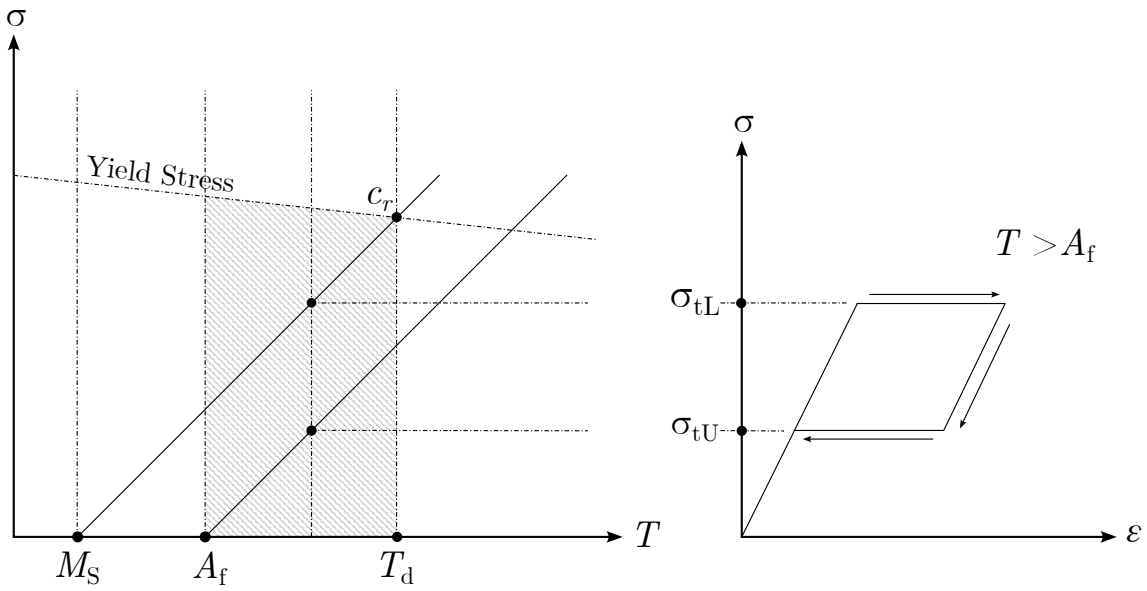

Figure 2.6: Temperature dependence of transformation stress. Left: stress-temperature graph. The shaded area marks the region in which the superelastic effect is assured. The critical point c_r marks the intersection of the upper stress and temperature limit. Right: stress-strain curve. Adapted from Reference [12].

In Figure 2.7a a load-unload cycle of a superelastic material is shown at a temperature above A_f to illustrate the event of superelasticity. The stress-strain curve takes the form of a hysteresis, typical for superelastic material. Three regimes subdivide the curve, each marked by different colors, representing different stages of the microstructure of the material, and are illustrated in Figure 2.7a. In the first regime (0 → a), the material is fully austenitic and shows linear elastic properties. When a certain stress threshold is reached, characterized by σ_{tL}^S and point a, the martensitic transformation begins and a new regime (a → b) is entered. The blue curve representing the said regime and resembling a "plateau", captures the origin of the high reversible strains of superelastic material. A marginal increase in stress is accompanied by a large increase in strains. Here, the phase of the material consists partially of austenite and martensite, as visible in Figure 2.7b (center). At point b, the stress σ_{tL}^E is reached, marking the end of the martensitic transformation. Characterized by the green curve, the crystallographic structure of the material now consists of fully detwinned martensite. If the load is further increased, point c is reached, the elastic regime of the martensite is left, and plastic yielding occurs. The de-twinned martensite is not stable at a temperature greater than A_f. This means that when the load is removed, the stress decreases linearly until the critical stress σ_{tU}^S is reached. A new regime (d → e) is entered in which the retransformation is taking place. When the stress has reverted to σ_{tU}^E, the microstructure is fully transformed back to stable austenite, and a linear elastic regime is entered again.

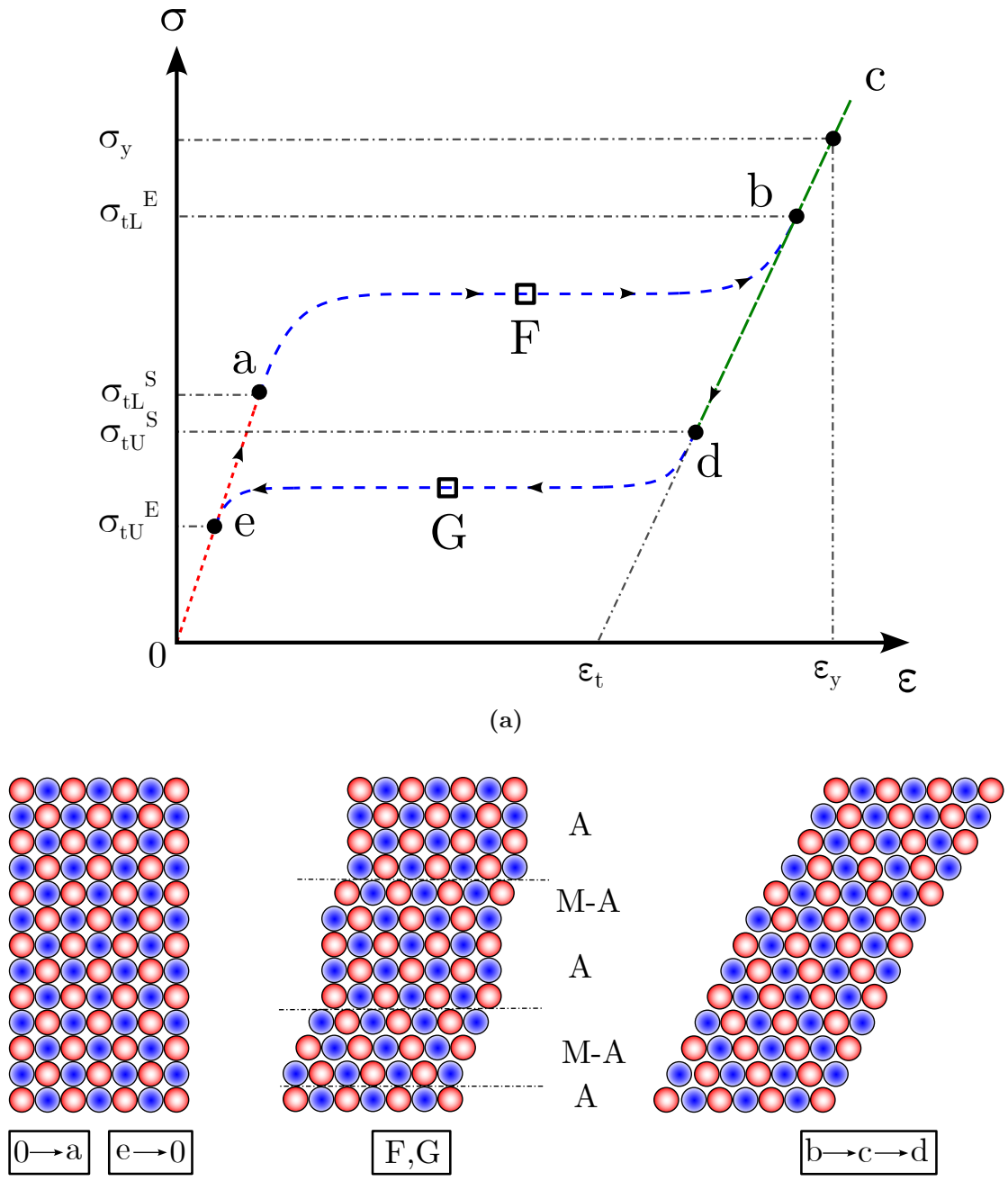

(a)

(b)

Figure 2.7: Relation of stress-strain state and microstructure in the event of superelasticity. (a): Stress-Strain curve of superelastic material. The curve is subdivided into three regions. Red region: the phase of the material is austenitic. Blue region: martensitic transformation takes place. Green region: the phase of the material is martensitic. Adapted from References [12], [13], [26].
(b): Atomic arrangements corresponding to the defined regions.
Left: the phase of the material is austenitic. Center: the martensitic transformation has begun. The material microstructure consists of partly austenite (parent) and martensite phase. Right: the phase of the material consists completely of de-twinned martensite. Adapted from Reference [12].

2.3.1 NiTi Shape Memory Alloy

Today, there exists a wide range of shape memory alloys of different chemical composition. They include gold-based (Au-Cd, Au-CuZn), copper-based (CuAlNi, CuAlBe, CuSn, CuZn), and most prominently the nickel-titanium-based alloys [11]. The shape memory properties of NiTi were first discovered in 1956 by William Buehler at the Naval Ordnance Laboratory (NOL), which explains the commonly encountered acronym NiTiNol [11]. In addition to their functional properties (i.e. the shape memory and superelastic effect), NiTi-based alloys shine with good workability in the martensite phase, good corrosion and fatigue resistance, damping capacity and most notably biocompatibility [13].
These well-documented properties explain why NiTi-based alloys are today the most commonly used shape memory alloys and represent the basis for numerous innovative applications in the fields of biomedical, aerospace, and structural engineering.
Examples of a set of NiTi applications are shown in Table 2.1.

Table 2.1: NiTi-based alloy applications in the field of biomedical, aerospace and structural engineering.

Fields of application	
Biomedical Engineering	Orthodontic field: wires, platal arches, endodontic files Orthopedic field: intraspinal plants, intramedullary nails Vascular field: venous filters, self-expandable vascular stents Neurosurgical field: coils, stent, microguidewires
Aerospace Engineering	hydraulic tubing coupling, actuator for morphed wings, actuator for deployment of solar panels
Structural Engineering	self-rehabilitation device, damping device for bridge structures

2.4 Plane Stress

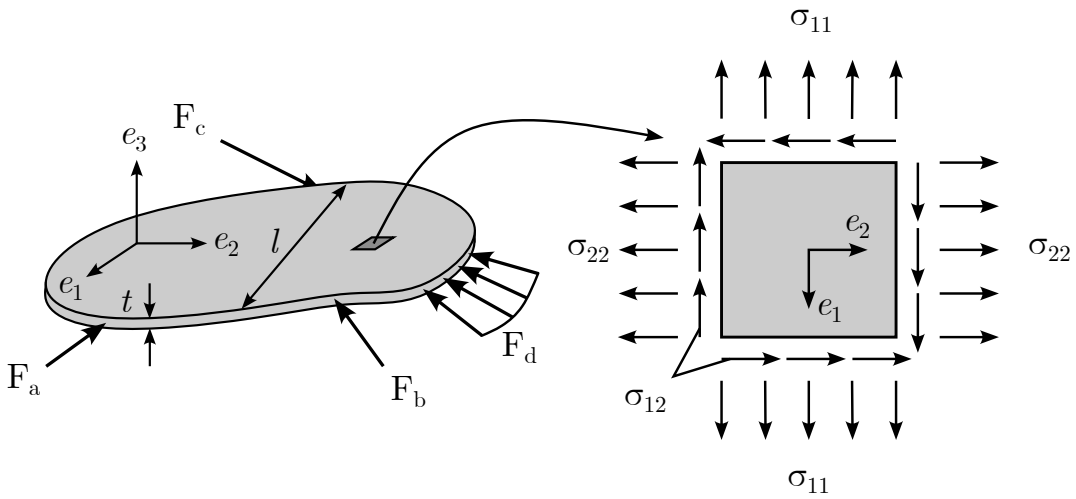

Figure 2.8: Left: solid body, fulfilling the requirements for the assumption of plane stress. Right: detailed view on the stresses acting within the solid body. Taken and adjusted from Reference [27].

In the field of engineering, reducing the complexity of a problem is one of the first steps in solving it. In solid mechanics, given the right circumstances, a common simplification is the reduction from triaxial stress and strain states to plane ones. This leads to a decrease in the number of degrees of freedom, thus rendering analysis more manageable, allowing for solutions of problems which, in the three-dimensional space, are considered to be hard to solve up to unsolvable. In solid mechanics two main assumptions are generally used which allow the reduction down to a two-dimensional problem: the plane strain state and the plane stress state [27]. In this work, only the plane stress state is presented, as it is the stress state used for analysis in this work. The requirements necessary to apply the plane stress assumption are (1) that the thickness t of the solid under investigation must be significantly smaller than its characteristic length l and (2) that the solid is strictly loaded in its plane, as shown in Figure 2.8.

For the plane stress state, the out-of plane stresses are assumed to be zero, thus,

$$\sigma_{33} = \sigma_{13} = \sigma_{23} = 0. \tag{2.16}$$

Whereas, the in-plane stresses remain non-zero. For a solid body with isotropic material properties, the generalized Hooke's law reads in Voigt notation

$$\begin{bmatrix} \sigma_{11} \\ \sigma_{22} \\ 0 \\ 0 \\ 0 \\ \sigma_{12} \end{bmatrix} = \begin{bmatrix} \frac{E(1-\nu)}{(1+\nu)(1-2\nu)} & \frac{\nu E}{(1+\nu)(1-2\nu)} & \frac{\nu E}{(1+\nu)(1-2\nu)} & 0 & 0 & 0 \\ \frac{\nu E}{(1+\nu)(1-2\nu)} & \frac{E(1-\nu)}{(1+\nu)(1-2\nu)} & \frac{\nu E}{(1+\nu)(1-2\nu)} & 0 & 0 & 0 \\ \frac{\nu E}{(1+\nu)(1-2\nu)} & \frac{\nu E}{(1+\nu)(1-2\nu)} & \frac{E(1-\nu)}{(1+\nu)(1-2\nu)} & 0 & 0 & 0 \\ 0 & 0 & 0 & \frac{E}{2(1+\nu)} & 0 & 0 \\ 0 & 0 & 0 & 0 & \frac{E}{2(1+\nu)} & 0 \\ 0 & 0 & 0 & 0 & 0 & \frac{E}{2(1+\nu)} \end{bmatrix} \begin{bmatrix} \varepsilon_{11} \\ \varepsilon_{22} \\ \varepsilon_{33} \\ 0 \\ 0 \\ \gamma_{12} \end{bmatrix} \tag{2.17}$$

or in condensed form

$$\begin{bmatrix} \sigma_{11} \\ \sigma_{22} \\ \sigma_{12} \end{bmatrix} = \begin{bmatrix} \frac{E}{1-\nu^2} & \frac{\nu E}{1-\nu^2} & 0 \\ \frac{\nu E}{1-\nu^2} & \frac{E}{1-\nu^2} & 0 \\ 0 & 0 & \frac{E}{2(1+\nu)} \end{bmatrix} \begin{bmatrix} \varepsilon_{11} \\ \varepsilon_{22} \\ \gamma_{12} \end{bmatrix} \tag{2.18}$$

with $\gamma_{12} = 2\,\varepsilon_{12}$, E being the Young's Modulus, and ν the Poisson ratio.
The inverse relation reads

$$\begin{bmatrix} \varepsilon_{11} \\ \varepsilon_{22} \\ \varepsilon_{33} \\ 0 \\ 0 \\ \gamma_{12} \end{bmatrix} = \begin{bmatrix} \frac{1}{E} & \frac{-\nu}{E} & \frac{-\nu}{E} & 0 & 0 & 0 \\ \frac{-\nu}{E} & \frac{1}{E} & \frac{-\nu}{E} & 0 & 0 & 0 \\ \frac{-\nu}{E} & \frac{-\nu}{E} & \frac{1}{E} & 0 & 0 & 0 \\ 0 & 0 & 0 & \frac{2(1+\nu)}{E} & 0 & 0 \\ 0 & 0 & 0 & 0 & \frac{2(1+\nu)}{E} & 0 \\ 0 & 0 & 0 & 0 & 0 & \frac{2(1+\nu)}{E} \end{bmatrix} \begin{bmatrix} \sigma_{11} \\ \sigma_{22} \\ 0 \\ 0 \\ 0 \\ \sigma_{12} \end{bmatrix} \tag{2.19}$$

or in condensed form

$$\begin{bmatrix} \varepsilon_{11} \\ \varepsilon_{22} \\ \gamma_{12} \end{bmatrix} = \begin{bmatrix} \frac{1}{E} & \frac{-\nu}{E} & 0 \\ \frac{-\nu}{E} & \frac{1}{E} & 0 \\ 0 & 0 & \frac{2(1+\nu)}{E} \end{bmatrix} \begin{bmatrix} \sigma_{11} \\ \sigma_{22} \\ \sigma_{12} \end{bmatrix}. \tag{2.20}$$

In the context of this thesis, plane stress is encountered in the discretization of the unit cell variants and plays a significant role in the viability of the comparisons that are conducted as part of the verification process. To properly compare the same model discretized once using beam elements and once using continuum elements, it is essential that for the second model, plane stress continuum elements are chosen. This requirement traces back to the beam element's characteristic of exhibiting in the depth of the beam a state of plane stress [28].

2.5 Simple Shear and Pure Shear

Shear is an important type of deformation that is of considerable importance in many theoretical and practical problems in engineering. In general, it is differentiated between two types of shear: (1) pure shear and (2) simple shear. In this section, pure and simple shear are presented and their differences outlined.
For the purpose of a better description of both types of deformation, the deformation gradient tensor is first introduced.

2.5.1 The Deformation Gradient Tensor

The deformation gradient tensor allows for a mathematical description of a body's deformation. The deformation of a continuum is characterized by two states in which the body occupies different places in space and time. These states are referred to as (1) the reference configuration, and (2) the current configuration [22]. The first describes a state at time $t = t_0$ in which the continuum B_0 has not yet undergone any deformation and is free of stress. The material points belonging to the undeformed body are characterized by the vector $\underline{\mathbf{a}}$. The second configuration refers to the state at time $t > t_0$ in which the body, referenced as B_d, is in a deformed state, with internal stresses potentially being present. Its material points are described through the vector $\underline{\mathbf{x}}$.
The two-point deformation gradient tensor, defined as

$$\underset{\sim}{F} = \frac{\partial x_i}{\partial a_j}\underline{\mathbf{e}}_i \otimes \underline{\mathbf{e}}_j = \begin{bmatrix} \frac{\partial x_1}{\partial a_1} & \frac{\partial x_1}{\partial a_2} & \frac{\partial x_1}{\partial a_3} \\ \frac{\partial x_2}{\partial a_1} & \frac{\partial x_2}{\partial a_2} & \frac{\partial x_2}{\partial a_3} \\ \frac{\partial x_3}{\partial a_1} & \frac{\partial x_3}{\partial a_2} & \frac{\partial x_3}{\partial a_3} \end{bmatrix} \tag{2.21}$$

allows for the description of a continuum's deformation by forming a relation between an infinitesimal material tangent vector $\mathrm{d}\underline{\mathbf{a}}$ (see Figure 2.9) in the reference configuration and an infinitesimal spatial tangent vector $\mathrm{d}\underline{\mathbf{x}}$ in the current configuration through linear mapping in the form of $\mathrm{d}\underline{\mathbf{x}} = \underset{\sim}{F}(\underline{\mathbf{a}}, t)\mathrm{d}\underline{\mathbf{a}}$ [29].

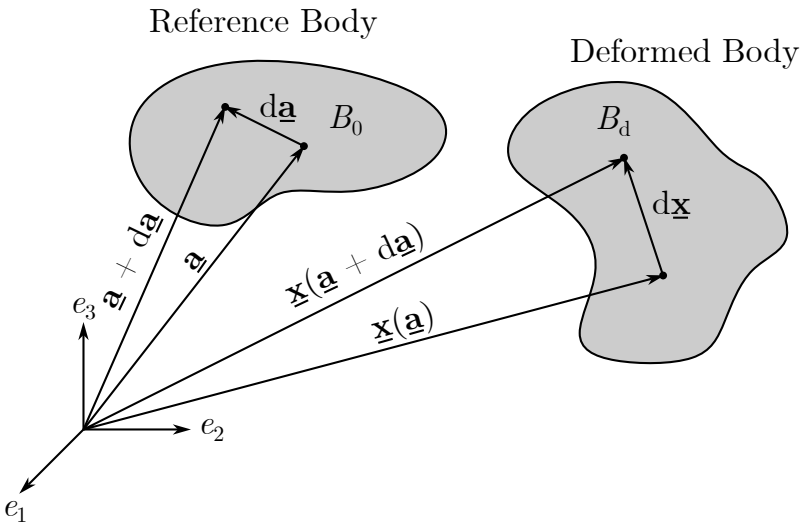

Figure 2.9: Solid body in its reference and current (or deformed) configuration. Taken and adjusted from Reference [22].

The strains in the reference configuration can then be expressed through the Green-Lagrangian strain tensor which reads

$$\underset{\sim}{\varepsilon}_G = \frac{1}{2}\left(\underset{\sim}{F}^T\underset{\sim}{F} - \underset{\sim}{I}\right) \tag{2.22}$$

with $\underset{\sim}{I}$ being the unit tensor.

2.5.2 Pure Shear

In a pure shear event, material lines, initially parallel to the e_1-axis, rotate by an angle of $\gamma/2$ in the mathematically positive direction, while material lines that were parallel to the e_2-axis prior to the shear motion undergo a negative rotation of the same angle $\gamma/2$ [19], see Figure 2.10.
To properly describe the deformation gradient tensor of pure shear, the strain tensor is required. In linear elasticity, the infinitesimal pure shear strain is defined as

$$\underset{\sim}{\varepsilon}_\gamma = \begin{bmatrix} 0 & \gamma/2 & 0 \\ \gamma/2 & 0 & 0 \\ 0 & 0 & 0 \end{bmatrix} \tag{2.23}$$

with $\gamma \in \mathbb{R}$ the shear angle. Thus, resulting in a deformation gradient tensor that reads

$$\underset{\sim}{F}_{\gamma PS} = \underset{\sim}{I} + \underset{\sim}{\varepsilon}_\gamma = \begin{bmatrix} 1 & 0 & 0 \\ 0 & 1 & 0 \\ 0 & 0 & 1 \end{bmatrix} + \begin{bmatrix} 0 & \frac{\gamma}{2} & 0 \\ \frac{\gamma}{2} & 0 & 0 \\ 0 & 0 & 0 \end{bmatrix} = \begin{bmatrix} 1 & \frac{\gamma}{2} & 0 \\ \frac{\gamma}{2} & 1 & 0 \\ 0 & 0 & 1 \end{bmatrix} \tag{2.24}$$

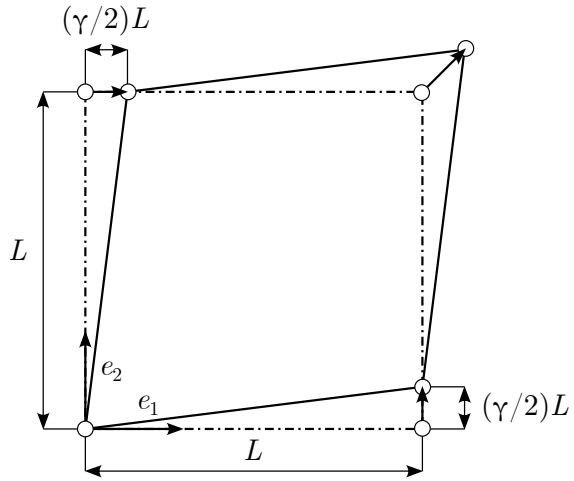

Figure 2.10: Solid body deformed under pure shear. Taken from Reference [19]

Observing the form of the deformation gradient tensor $\underset{\sim}{F}_{\gamma PS}$, it becomes clear that the deformation of pure shear is infinitesimally volume preserving since $\mathrm{tr}(\underset{\sim}{F}_{\gamma PS} - I) = 0$. However, it is to be noted that this is not the case for finite strains, as $\det(\underset{\sim}{F}_{\gamma PS}) \neq 1$.

2.5.3 Simple Shear

In a simple shear event, the material lines that were previously parallel to the e_1-axis remain as such, while the material lines that were parallel to the e_2-axis, prior to deformation, are subjugated to a negative rotation of Θ, see Figure 2.11.

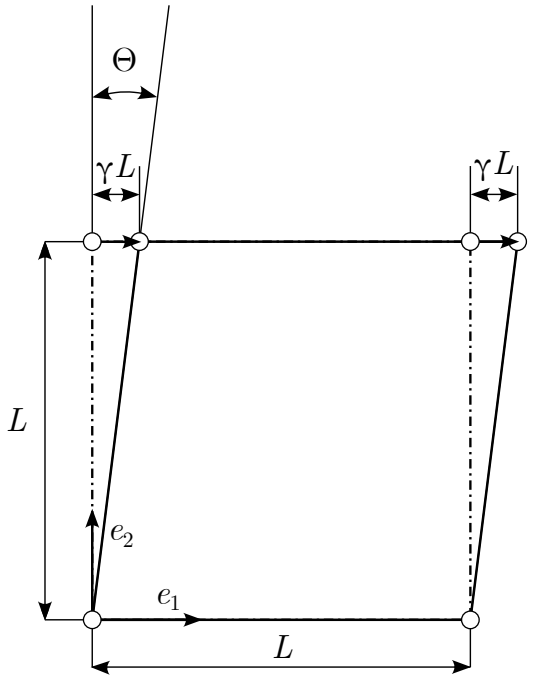

Figure 2.11: Solid body deformed under simple shear. Taken from Reference [19]

Simple shear can be considered as an extension of pure shear, as here the deformation consists of a pure shear event combined with a solid-body rotation. Thus, in linear elasticity, the simple shear deformation consists of the infinitesimal pure shear strain $\underset{\sim}{\varepsilon}_\gamma$, shown in Equation (2.23), and the infinitesimal rotation $\underset{\sim}{\omega}_\gamma$, which reads as:

$$\underset{\sim}{\omega}_\gamma = \begin{bmatrix} 0 & \gamma/2 & 0 \\ -\gamma/2 & 0 & 0 \\ 0 & 0 & 0 \end{bmatrix} \tag{2.25}$$

By adding both Equation (2.24) and (2.25), the deformation gradient tensor for simple shear is formed and can thus be expressed through

$$\underset{\sim}{F}_{\gamma SS} = \underset{\sim}{I} + \underset{\sim}{\varepsilon}_\gamma + \underset{\sim}{\omega}_\gamma = \underset{\sim}{F}_{\gamma PS} + \underset{\sim}{\omega}_\gamma = \begin{bmatrix} 1 & \frac{\gamma}{2} & 0 \\ \frac{\gamma}{2} & 1 & 0 \\ 0 & 0 & 1 \end{bmatrix} + \begin{bmatrix} 0 & \frac{\gamma}{2} & 0 \\ -\frac{\gamma}{2} & 0 & 0 \\ 0 & 0 & 0 \end{bmatrix} = \begin{bmatrix} 1 & \gamma & 0 \\ 0 & 1 & 0 \\ 0 & 0 & 1 \end{bmatrix} \tag{2.26}$$

To emphasize the connection between pure and simple shear, the two deformations are illustrated side by side in Figure 2.12.
Lastly, by inspecting the form of the deformation gradient tensor of simple shear, it is observed that, similarly to pure shear, the deformation gradient tensor $\underset{\sim}{F}_{\gamma SS}$ also

is infinitesimally volume preserving , as $\mathrm{tr}(\underset{\sim}{F}_{\gamma SS} - \underset{\sim}{I}) = 0$. Interestingly, this also holds true for finite strains as $\det(\underset{\sim}{F}_{\gamma SS}) = 1$.

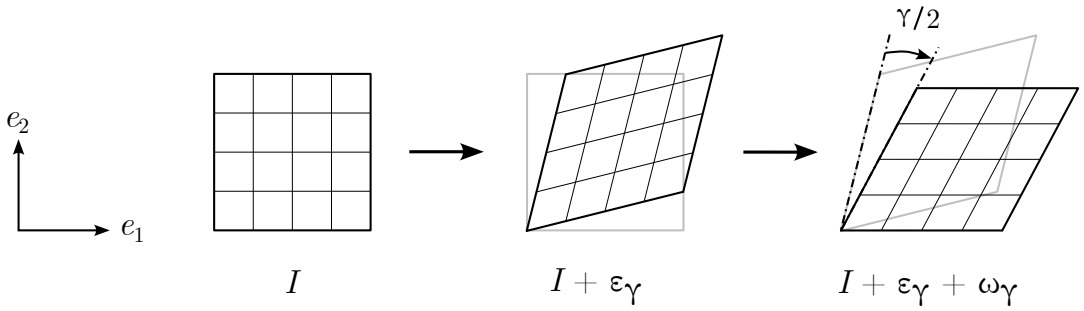

Figure 2.12: Connection between pure and simple shear. Left: no deformation is applied to the solid body. Center: the solid body is deformed under pure shear. The material lines are rotated by $\gamma/2$ respective to the coordinate system. Right: the solid body is deformed under simple shear. Relative to the pure shear deformation, the body is rotated by $\gamma/2$. Adapted from Reference [20].

2.6 Material Models for Superelasticity

In the following section, a closer look is given on the superelastic material models in this thesis. This includes the *ABAQUS* Standard Material Model for Superelasticity, and the two `UHYPEL`-based material models, stemming from the works of Schasching et al. [7]. Their implementation is shortly outlined, and information is provided on the parameters they require for their respective characterization. Last, their limitations are presented and briefly compared among each other.

2.6.1 Superelasticity Model in Abaqus

The *ABAQUS* built-in standard material model for superelasticity (ASM) is based on the two publications by Auricchio et al. [8], [9]. The material model is capable of handling the reorientation of martensite, the stress-induced transformation of martensite into austenite, and the stress-induced transformation of austenite to single variant martensite. In this work, only the latter transformation process is applied, and thus compared to the custom-made material models. Regarding the selection of allowable element types, the ASM model works with each element type available in the *ABAQUS* element library, be they continuum or structural elements. The definition of the key material points characterizing the stress-strain hysteresis is implemented via a set of different parameters, summarized in Table 2.2. As a supplementary visualisation, the key parameters are indicated in Figure 2.13.

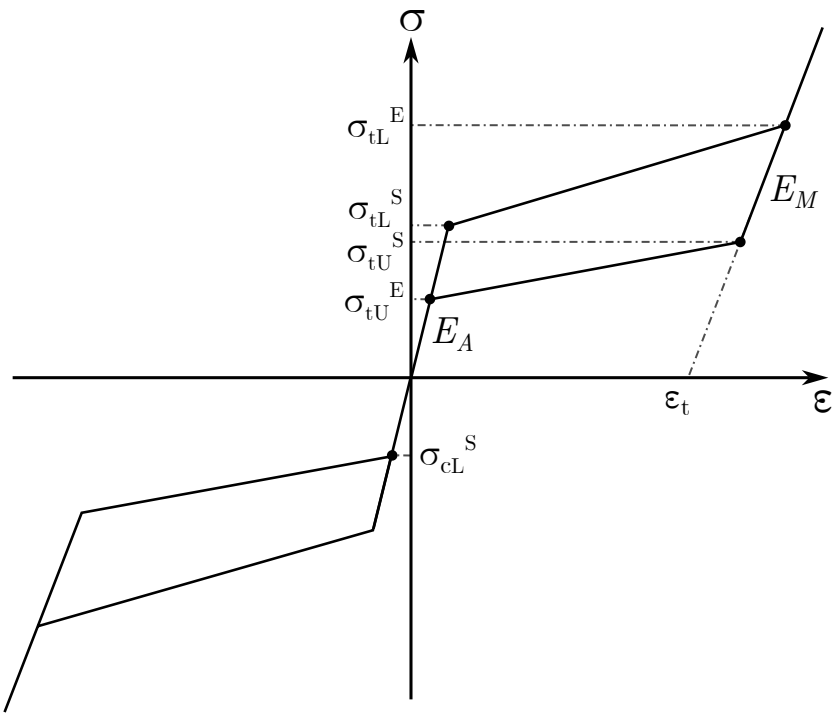

Figure 2.13: Stress-strain response of the ASM model. The key parameters are indicated.

Table 2.2: Parameters used for the calibration of the ASM model.

Parameter	Symbol
Young's Modulus austenite	E_A
Poisson ratio austenite	ν_A
Young's modulus martensite	E_M
Poisson ratio martensite	ν_M
Transformation strain	ε_t
Start of transformation in tension (loading)	σ_{tL}^S
End of transformation in tension (loading)	σ_{tL}^E
Start of reverse transformation in tension(unloading)	σ_{tU}^S
End of reverse transformation in tension (unloading)	σ_{tU}^E
Start of reverse transformation in compression (loading)	σ_{cL}^S
Reference temperature	T_0
Slope of the stress versus temperature curve for loading	$\left(\frac{\delta\sigma}{\delta T}\right)_L$
Slope of the stress versus temperature curve for unloading	$\left(\frac{\delta\sigma}{\delta T}\right)_U$

Another characteristic of the material model is that the temperature dependence of the start and end of the martensitic transformation is taken into account, which explains why the reference temperature is one of the required parameters indicated

in Table 3.5.
In the ASM model, the Young's modulus and Poisson ratio for the region in which the phase transformation occurs are implemented as mixed Young's modulus and Poisson ratio [26]. They are based on the material data input for the respective phases and read

$$E = E_A + \zeta(E_M - E_A) \tag{2.27}$$

$$\nu = \nu_A + \zeta(\nu_M - \nu_A) \tag{2.28}$$

where ζ is the volumetric fraction of martensite, E_A the Young's modulus of austenite, E_M the Young's modulus of martensite, ν_A the Poisson ratio of austenite and ν_M the Poisson ratio of martensite.
Furthermore, the material model is based on an additive strain decomposition in which the total strain increment tensor, $\Delta\underset{\sim}{\varepsilon}$, is assumed to be the sum of the increment in elastic strain, $\Delta\underset{\sim}{\varepsilon}^{el}$, and the transformation strain increment tensor, $\Delta\underset{\sim}{\varepsilon}^{tr}$.
The increment in transformation strain tensor is calculated using the following flow rule, which reads

$$\Delta\underset{\sim}{\varepsilon}^{tr} = \Delta\zeta\frac{\partial G^{tr}}{\partial\underset{\sim}{\sigma}} \tag{2.29}$$

where $\underset{\sim}{\sigma}$ is the stress tensor and the transformation flow potential, G^{tr}, is assumed to follow the Drucker-Prager form

$$G^{tr} = q - p\tan\psi \tag{2.30}$$

where $p = -\frac{1}{3}tr(\underset{\sim}{\sigma})$ is the equivalent pressure stress and q is the von Mises equivalent stress. The transformation surface, F^{tr}, is also assumed to follow the Drucker-Prager form, varies linearly with temperature T, and is expressed through

$$F^{tr} = q - p\tan\beta. \tag{2.31}$$

The angles β and ψ are calculated from the tensile and compressive transformation stress levels, the uniaxial transformation strain, and the volumetric transformation strain provided by the user [26]. As a result of the formulation of the transformation flow potential and the transformation surface, both following the Drucker Prager form, the ASM model is perfectly capable of handling individual superelastic responses for tension and compression. However, in the present work, we do not consider a tension compression asymmetry, and thus the transformation flow potential and the

transformation surface simplify to $G^{tr} = q$ and $F^{tr} = q$, respectively, and therefore follow the von Mises form. For the sake of simplicity, throughout the rest of this thesis the Abaqus Standard Material model for superelasticity is referred to as bASM and cASM. Here, the former abbreviation refers to those cases in which the material model is used in combination with beam elements, and the latter to those scenarios in which continuum elements are used.

2.6.2 Hypoelastic Polynomial Fitted Material Model for Superelasticity

The superelastic material model presented in the work of Schasching et al. [7] is based on the `UHYPEL` interface of *ABAQUS*. The material model is setup exclusively for use with beam elements, i.e. uniaxial stress states. The `UHYPEL` interface in conjunction with beam elements requires as parameters the tangential Young's modulus, $E_T = \frac{\partial \sigma}{\partial \varepsilon}$, and the Poisson ratio, $\nu(\varepsilon)$. Therefore, the stress-strain relation of the superelastic material must be described. This is achieved by curve-fitting data points extracted from experiments conducted on superelastic material samples. Depending on the crystalline phase of the material, different polynomials are used for the curve-fitting operation. For the transition phase, a third-order polynomial is used. The stress-strain relation used for the transformation process of loading and the retransformation process of unloading reads

$$\sigma(\varepsilon) = a\varepsilon^3 + b\varepsilon^2 + c\varepsilon, \tag{2.32}$$

where the coefficients a, b, and c are obtained by curve fitting the experimental data set. For the fully transformed region, i.e the martensite phase, the stress-strain relation is described using linear polynomials and takes the form of

$$\sigma(\varepsilon) = d\varepsilon + k, \tag{2.33}$$

where the coefficient d, similar to the transition, is determined by curve fitting the experimental data set, and the coefficient k is the vertical intercept. The tangential Young's modulus is determined as

$$E_T(\varepsilon) = \frac{\partial \sigma}{\partial \varepsilon} = 3a\varepsilon^2 + 2b\varepsilon + c. \tag{2.34}$$

A typical stress-strain response for the UHYP-POLY model is given in Figure 2.14 illustrating the conditional switch from third-order polynomial to linear polynomial. As a result of the information contained in the curve constructed by the third-order polynomial, several parameters that are required for the calibration of the *ABAQUS*

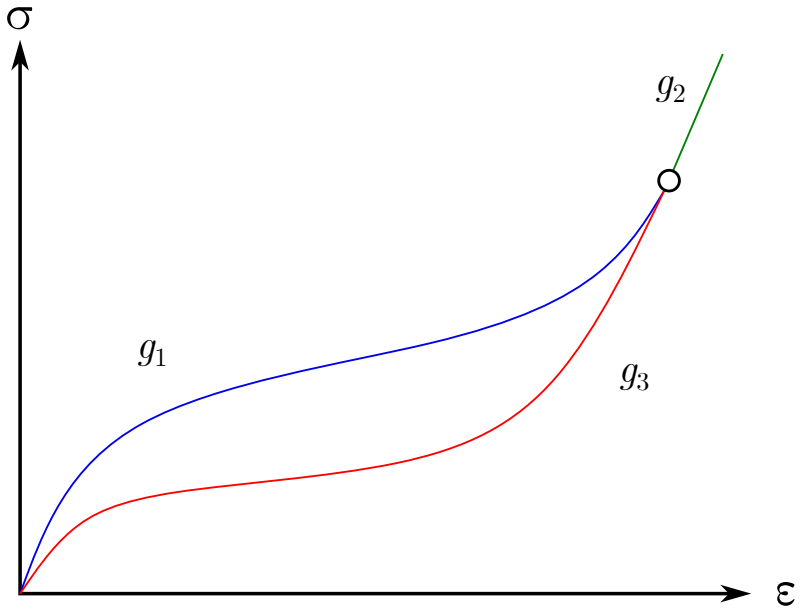

Figure 2.14: Stress-strain response of the UHYP-POLY material model comprising the two poly-fitted functions g_1 (blue) and g_3 (red) of the transformation regime and the linear function g_2 (green) of the martensite phase. The strain-based conditional switches occur at the marked point.

material model are here simplified or no longer needed. First, there is no parameter to determine the linear elastic regime of the austenite phase. The material model considers the transformation to start immediately. Thus, the stresses and strains at the beginning of the martensitic transformation are considered zero. With regard to the retransformation process during unloading, the stresses and strains are considered the same as at the end of the transformation process. Hence, it is no longer required and possible to define the beginning of the retransformation process separately. However, this is not consequential since all the information describing the material is already included in the curve described by the linear and third-order polynomials. Case distinctions are utilized to properly predict cycles of unloading and reloading at intermediate transformation strains [7]. Furthermore, the material model of Schasching et al. [7] does not consider tension-compression asymmetry. Lastly, it should be noted that for user-defined material models *ABAQUS* does not compute the transversal shear stiffness automatically; instead it must be given by the user. The parameters required to fully define the UHYP-POLY model are given in Table 2.3. Throughout this work, the material model proposed by Schasching et al. [7] is referred to as UHYP-POLY.

Table 2.3: Parameters used for the calibration of the UHYP-POLY model.

Parameter	Symbol
Young's Modulus martensite	E_M
Young's modulus of transformation regime (loading)	$E_{tL;T}(\varepsilon)$
Young's modulus of retransformation regime (unloading)	$E_{tU;T}(\varepsilon)$
Poisson ratio	$\nu(\varepsilon)$

2.6.3 Hypoelastic Multilinear Material Model for Superelasticity

The third material model presented in this thesis is referred to as the multilinear material model. Same as the UHYP-POLY model it is also a creation of Schasching et al. [7] and follows similar implementation steps.
Thus, it uses the `UHYPEL` interface too, and is limited to the use of beam elements. Consequently, the main objective consists again in the description of the tangential Young's modulus and the Poisson ratio, as they are both required by the `UHYPEL` interface. The description of the stress-strain relation of the superelastic material is achieved by linear interpolation between selected material points, creating a multilinear function in the process. To define the different subfunctions, the stress-strain hysteresis extracted from the experiments is subdivided into different regions, each representative of distinct states of the crystalline structure present in superelastic material. The stress-strain relation for these different regions is described using linear polynomials and reads

$$\sigma(\varepsilon) = d\varepsilon + k \tag{2.35}$$

where the coefficients d and k are obtained from the linear interpolation between the material points extracted from the experimental data set. Consequently, the tangential Young's modulus becomes a constant for this material model and reads

$$E_T = \frac{\partial \sigma}{\partial \varepsilon} = d. \tag{2.36}$$

To switch from one linear function to another, conditionals are used that are linked to the strain states of the key material points, see Figure 2.15.
Unlike the UHYP-POLY model, the austenite phase is described separately, and thus the transformation process is not considered to start immediately. This also means that opposed to the UHYP-POLY model, the multilinear material model requires in E_A one more parameter. Regarding the predictions of unloading and reloading cycles

within the transformation regime, the UHYP-MLIN model uses the same approach as the UHYP-POLY model and handles this via case distinctions. Furthermore, the model considers the response of the material in tension and compression to be the same.

The material model is expected to deliver less accurate results due to the linear nature of its implementation. Nevertheless, its role in the verification of the UHYP-POLY model is crucial, as it helps to isolate and link possible observations to either the `UHYPEL` interface or the polynomial-fitting.

To simplify further associations with this model, it will be referred to as UHYP-MLIN for the rest of this thesis.

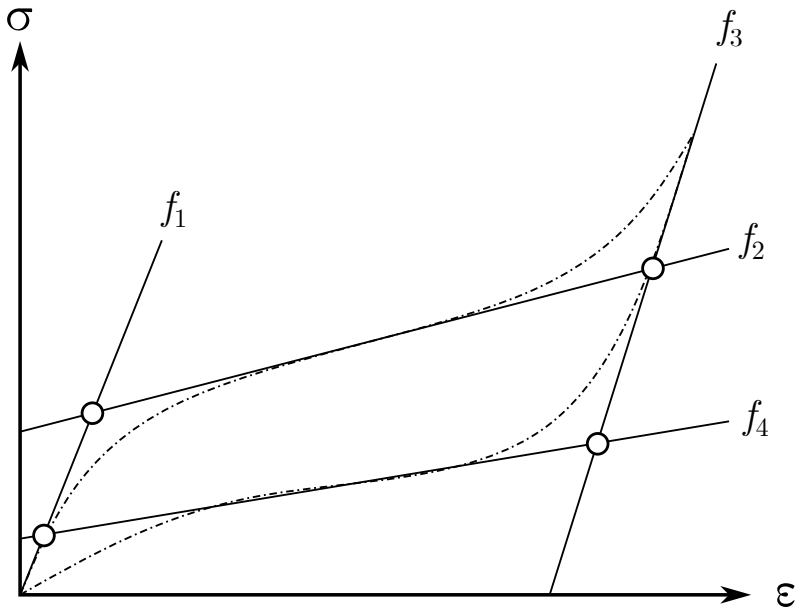

Figure 2.15: Stress-strain response of the UHYP-MLIN material model (solid-lines) juxtaposed to an assumed curve aimed to represent a realistic response (dash-dotted lines). The stress-strain response of the UHYP-MLIN material model comprises four linear functions f_1 to f_4, where strain-based conditional switches occur at the marked points.

2.7 Bifurcation of Equilibrium

The stability of a structure is a concept used to describe the "quality" of equilibrium of a mechanical system [21]. It is an important concept in the field of engineering, as it is essential for the proper assessment of the load-bearing capabilities of a structure. A system subjected to certain loads is regarded stable if its equilibrium condition remains the same when the loads are slightly changed [30]. However, if the system reacts dynamically to the increase in loads and deviates, as a result, from its equilibrium position, then it is considered unstable. Note that the applied load is just one of many parameters that influence the stability of a mechanical structure. For example, geometrical parameters such as the slenderness or length of beams can also change the stability behavior of a mechanical system. Physically, this phenomenon is best explained by the schematics shown in Figure 2.16. A spherical object is shown resting on surfaces of three different curvatures. Each scenario represents a different type of equilibrium.

The figure on the left represents the stable system. In this case, a slight lateral displacement of the object is inconsequential since the concave shape of the curve ensures that the sphere always returns to its initial equilibrium position. The center figure shows the neutral state. In this scenario, the system is at a critical point, where depending on the sign of the perturbation applied to the object, a stable or unstable system is possible. The figure on the right represents the unstable system. A slight lateral displacement applied to the sphere causes it to leave its initial equilibrium position without the possibility of returning.

The loss of structural stability can come in different forms. This includes (1) bifurcation of equilibrium, (2) snap-through, (3) snap-back, and (4) flutter instabilities [22]. The type of structural instability encountered in this work is beam buckling, which falls under the category of bifurcation of equilibrium. Thus, only this type of instability is presented.

Bifurcation of equilibrium refers to a phenomenon in which a mechanical system

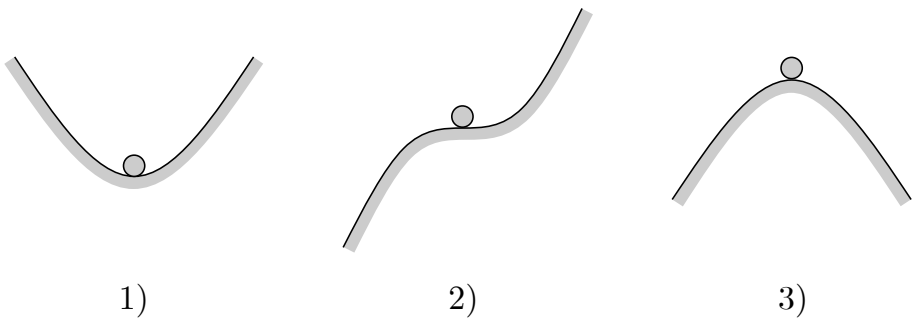

Figure 2.16: Physical example of equilibria of stability. a) stable, b) neutral, c) unstable. Taken from Reference [21].

switches from a current load-displacement path to an energetically more favorable one [22]. This means that by slightly varying certain parameters, a critical point, i.e. the bifurcation point, is reached, and the system branches into two or more equilibrium paths. The system enters the post-critical regime, and depending on the nature of the bifurcation, it can be either structurally stable or unstable.

Bifurcation of equilibrium is encountered in elastic systems subjected to compressive loads. The most common examples are beam, plate, and shell buckling. An effective way to characterize different types of bifurcation and their post-buckle regime, is the use of bifurcation diagrams.

As an explanatory example, the bifurcation diagram corresponding to the buckling of the universally known Euler beam is shown in Figure 2.17. A beam that is constrained at both ends is subjected to the compressive load λP, where λ represents the bifurcation parameter. The annotations S (solid line) and U (dashed line) refer to the stable and unstable regions, respectively. The parameter w represents the deflections of the beam. With increasing λ, the mechanical system reaches the critical bifurcation point λ_C, leaves the pre-critical phase ($\lambda < \lambda_C$), and the equilibrium path branches into three different paths. Of these three branches, the middle one represents the unstable theoretical trivial path ($w = 0 \,\forall\, \lambda$), where the beam remains undeflected, and the other two represent the stable nontrivial paths ($\lambda = \lambda(w)$), where buckling takes place.

A main characteristic of Euler beam buckling is that its mechanical response is insensible to the sign of the deflections, a characteristic phenomenon of symmetric systems. Furthermore, it manifests a stable post-buckling behavior. However, this is not always the case and might change depending on several factors, such as boundary

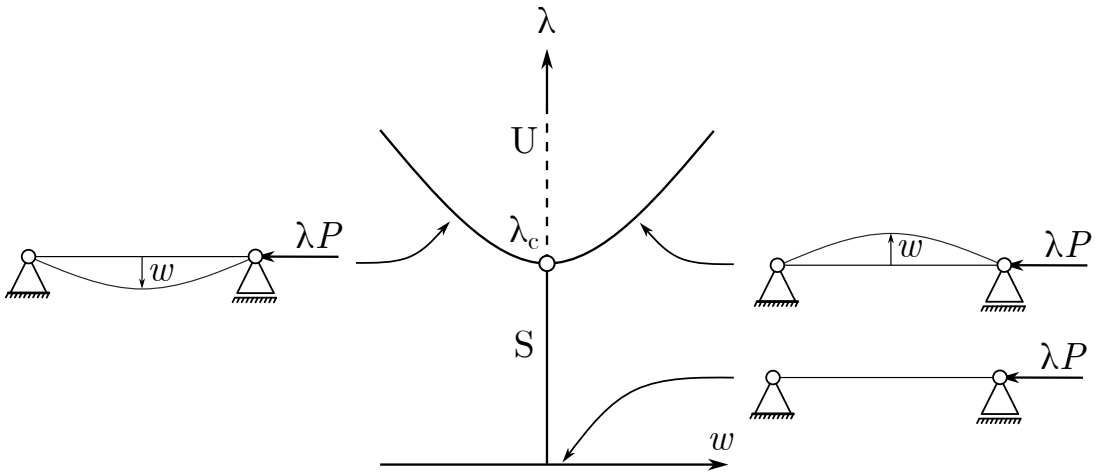

Figure 2.17: Bifurcation diagram of the Euler beam. The initial mechanical system has no imperfections. Adjusted from Reference [21].

conditions, the geometry of the structure, and the material property distribution [30].

Figure 2.18 shows two additional bifurcation diagrams, each with different post-critical regimes. The diagram on the left shows a bifurcation diagram of a symmetric system with an unstable post-buckling regime. Systems of this kind are unstable for $\lambda \geq \lambda_C$, meaning that an increase in load results in the collapse of the structure. An example displaying such a bifurcation diagram is the buckling of a cylindrical shell under axial pressure.

The bifurcation diagram of an asymmetric system is shown on the right. Here, the sign of the deflection determines whether the post-critical regime is stable ($\lambda > \lambda_C$) or unstable ($\lambda \leq \lambda_C$).

Up to this point, only systems without imperfections have been considered. However, real structures always suffer from imperfections, be they in the form of residual stresses, geometrical imperfections, or not perfectly applied loads. To illustrate the effect of imperfections, Euler beam buckling is drawn as an example once again with its bifurcation diagram shown in Figure 2.19. By introducing slight imperfections, which can be considered as perturbations, the bifurcation point is never reached. Instead, the equilibrium path follows the dotted path, approaching the branches of the perfect system.

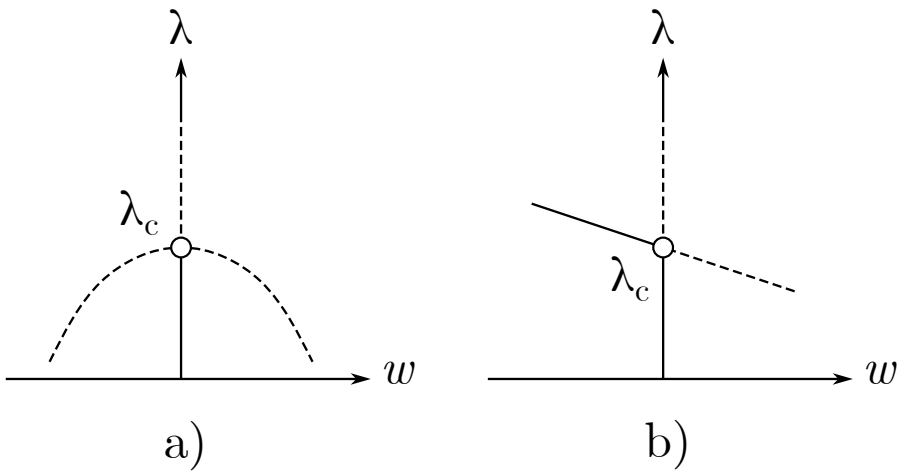

Figure 2.18: Bifurcation diagram a) unstable fork b) transcritical fork. Adjusted from Reference [22].

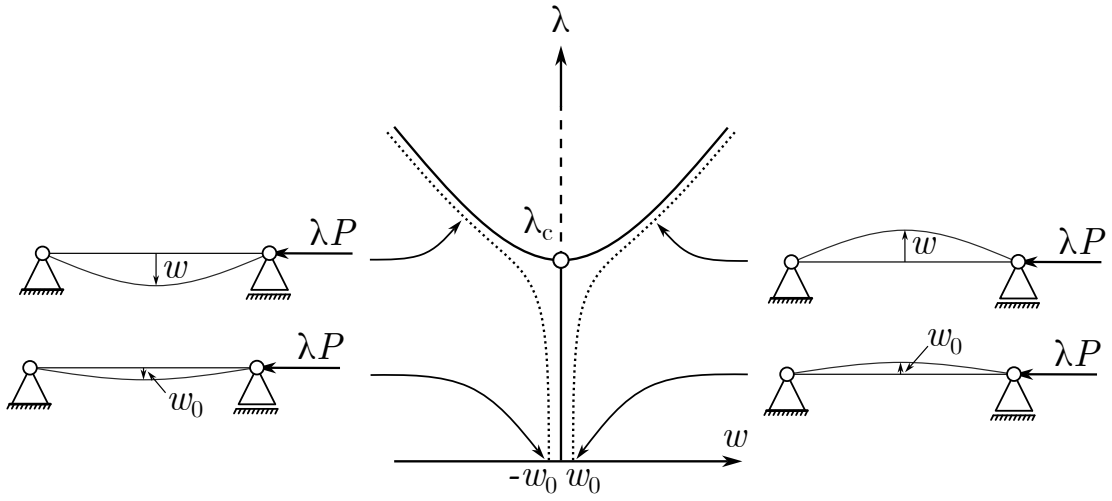

Figure 2.19: Bifurcation diagram of the Euler beam. The initial mechanical system is imperfect. Adjusted from Reference [21].

In terms of finite element modeling, this aspect can be used advantageously. When simulating structures that are prone to buckling, the simulation software attempts to exclusively follow the trivial unstable path, as it always considers a perfect system. As a consequence, the results of the simulation either provide misleading information or have convergence issues. A helping hand is the introduction of slight imperfections that are affine to the eigenform corresponding to the smallest eigenvalue of the system, ensuring a stable equilibrium path [22]. This, however, calls for the investigation of the influence of the imperfection on the mechanical response of the system. The sensitivity analysis is introduced, an investigation in which a relatively high imperfection is applied first to the system whose parameter is then gradually reduced. The slighter the imperfection, the more the response of the imperfect system approaches that of the perfect system, see Figure 2.20. The reduction of the imperfection parameter is then continued until convergence issues arise again.

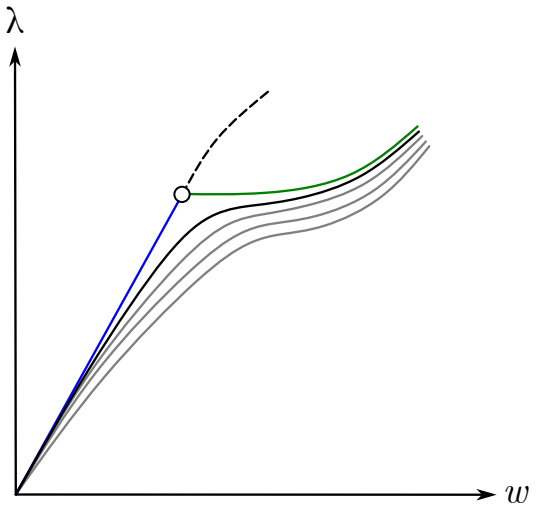

Figure 2.20: Load-displacement diagram of a system with a stable post-buckle regime as an example of a sensitivity analysis. Blue line: pre-buckle regime. Green line: stable post-buckle regime. Black dashed line: unstable trivial path. Solid black line: response of the imperfect system. Gray lines: response of the imperfect system; the greater the imperfection, the further it deviates from the perfect system.

3 Methodology

In the following chapter, the shapes and modeling strategies of the different unit cell variants are introduced. Information on the discretization, more specifically, the element types and amount of elements of each model is provided. The load cases of uniaxial tension and pure shear are presented. The method used to circumvent the instability issues encountered in later parts of this thesis is outlined, and the sensitivity analysis is presented, introducing a way to quantify the influence of the considered method on the mechanical response of the structure. Lastly, a look at the framework of the verification process is given, explaining the different kinds of comparisons conducted and their respective reasoning.

3.1 Geometry of the Unit Cell

In the present work, a total of three different unit cells are investigated, each based on the same initial geometry. They are categorized as the *cross* unit cell, the *slender* unit cell, and the *slender compliant* unit cell. The geometry on which they are based is a cross-shaped structure consisting of four struts of equal length L, each with rectangular cross section. Consequently, the geometry shows mirror symmetry with respect to the 1- and 2-axis of the coordinate system. A sketch of the structure is shown in Figure 3.1 where, t is the thickness of the struts, h the depth of the cell, and A the area used to calculate the stresses. The parameters L_1 and L_2 represent the height and width of the unit cell. The numerical values of these quantities are given in Table 3.1.

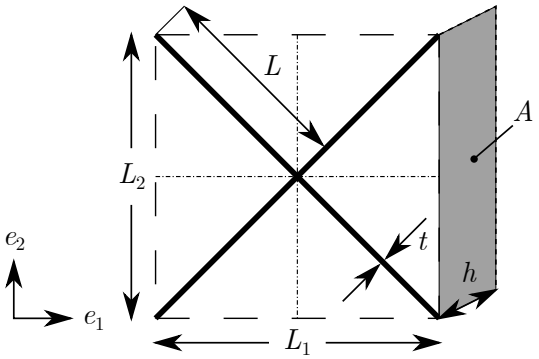

Figure 3.1: General form of the unit cell with its corresponding geometrical parameters.

Table 3.1: Geometrical parameters of the general form of the unit cell.

	Value	Unit
A	10	mm^2
h	1	mm
L	7.07	mm
L_1	10	mm
L_2	10	mm
t	1.41	mm

3.2 Modeling Strategies

Each variant of the unit cell deviates to some extent from its general form. In particular, variations are present in terms of shape due to added geometrical features. Therefore, a description of the modeling strategies for each cell is required, providing information on the element types used, their total number, and the implementation of the added features. In this section, the unit cell variants are modeled using either continuum or beam elements. To simplify the description, the unit cells modeled with the former elements will be referred to as continuum models, while the ones modeled with the latter elements will be referred to as beam models.

3.2.1 Cross Unit Cell

The first variant of the unit cell presented is the *cross* unit cell. Among all unit cells investigated, this unit cell has the shape closest to the general form, as its total dimensions and strut thickness are identical to the general form shown in the previous section.

The *cross* unit cell exists as two separate models; (1) a continuum model and (2) a beam model.

The continuum model is shown in Figure 3.2.

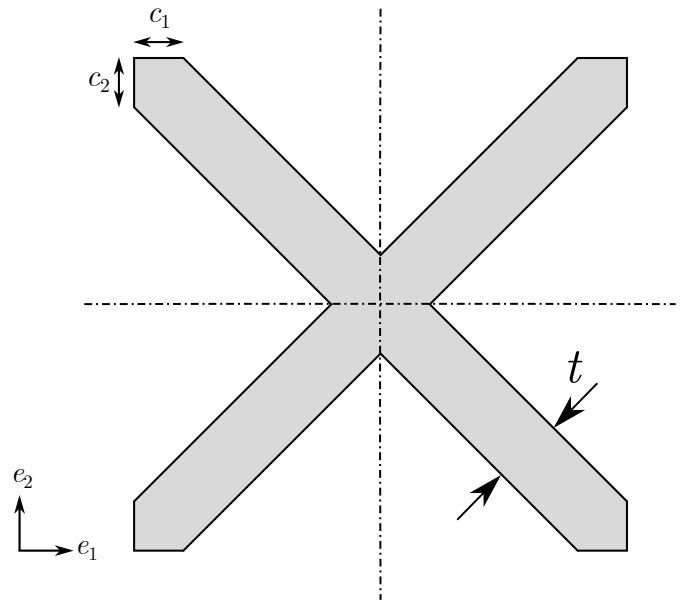

Figure 3.2: *Cross* unit cell

Table 3.2: Geometrical parameters of the *cross* unit cell's features. For the other dimensions see Table 3.1.

	Value	
c_1	1	mm
c_2	1	mm
t	1.41	mm

The model possesses right-angled corners located on the border domain of the unit cell which are a unique feature of all the continuum models presented in this work. The corners are characterized by c_1 and c_2, which define their horizontal and vertical edges. The corresponding numerical values are given in Table 3.2. This particular shape of the corner edges is chosen to conform to the requirements set by the periodic microfield theory. In order to use this continuum model as a basis for the approximation of the behavior of a lattice structure, it is essential that the edges on the border domain are shaped so that the neighboring unit cells fit seamlessly next to each other. Notably, this also means that all edges must be seeded identically, ensuring nodal compatibility along the entire border domain. Thus, each of the eight edges are seeded with eleven equidistant nodes, see Figure 3.3.

For the element type chosen, the *cross* unit cell continuum model, and each subsequent one in this thesis, is discretized with eight-node plane stress continuum elements. They are denoted "CPS8" in the *ABAQUS* element library. In total, the mesh comprises 4220 elements and is shown in Figure 3.4.

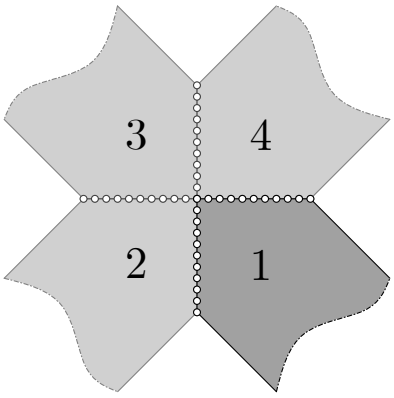

Figure 3.3: Detailed view of the edge seeding. The corner edges of four neighboring unit cells with homologous nodes are displayed. The cell denoted with the number 1, is the original unit cell used for the analysis. The edges are seeded with a total of eleven equidistant nodes resulting in a distance of 0.1 mm between each node. The remaining nodes not lying on the corner edges are not displayed.

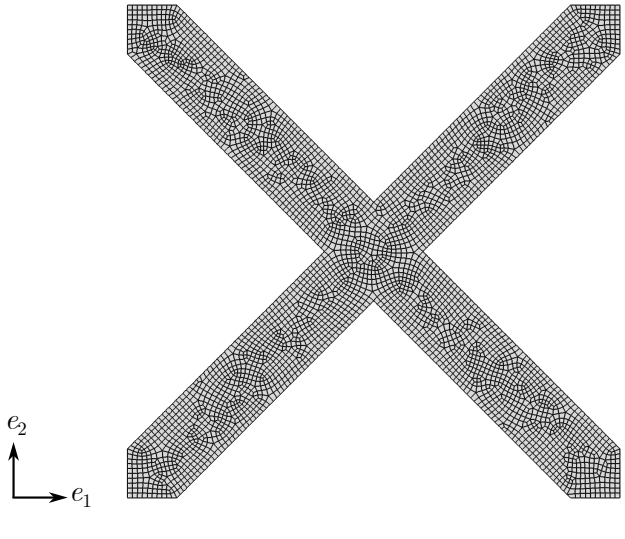

Figure 3.4: Mesh of the continuum model of the *cross* unit cell

As for the beam model of the *cross* unit cell, it does not have features that deviate its form from the general one shown in Figure 3.1. Thus, also its geometry parameters are the same as in Table 3.1. The beam orientation is chosen as shown in Figure 3.5. Each beam model in this thesis is discretized with the same type of elements and shares the same cross-sectional beam shape and total number of section points. The elements used are three-node quadratic Timoshenko beams. Their designation in the *ABAQUS* element library is "B22". The cross section of the beam elements is rectangular with a total of 25 section points along height, t, of the section, see Figure

3.6. Note that the two parameters, height t, and width h, equivalently represent the thickness of the struts and the depth of the unit cell, respectively. The mesh of the beam model is generated with a total of 284 elements.

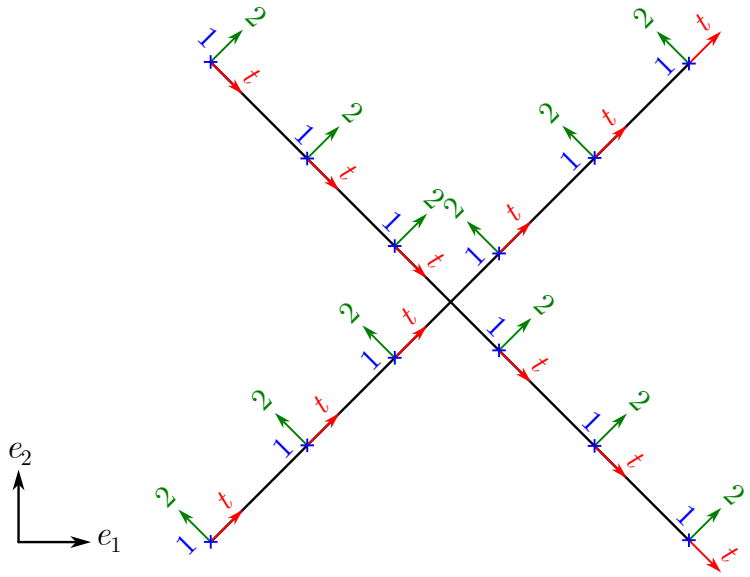

Figure 3.5: Beam orientation of the *cross* unit cell and the *slender* unit cell.

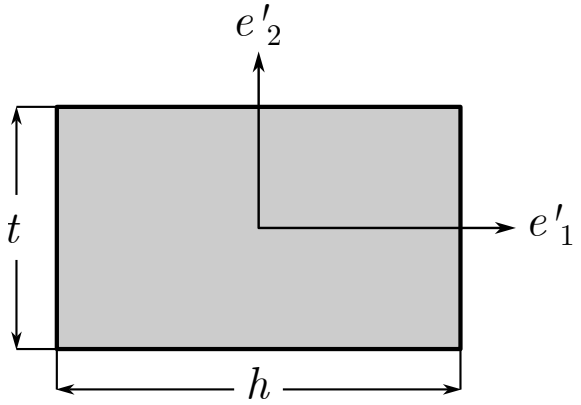

Figure 3.6: Rectangular profile of the beam section with its local coordinate system.

3.2.2 Slender Unit Cell

The *slender* unit cell is a modified version of the *cross* unit cell. Its shape is adjusted to better capture the imperfections of additively manufactured lattices. Starting from each end of the struts, their thickness is gradually reduced, leading to a final thickness of $t = 0.5$mm. The idea is to imitate the material aggregations at the strut intersections while simultaneously investigating a more lightweight version of the *cross* unit cell. The shape of the *slender* unit cell is shown in Figure 3.7 while the geometrical parameters of its unique features are given in Table 3.3.

The overall dimensions in height, width, and depth remain the same as for the general geometry of the unit cell. This variant also exists as a continuum and beam model. Regarding the continuum model, the corner edges on the border domain of the unit cell are shaped and seeded identically to those of the *cross* unit cell, as previously shown. The mesh of the continuum model consists of the same type of element as for the *cross* unit cell, i.e., eight-node plane stress elements, and is shown in Figure

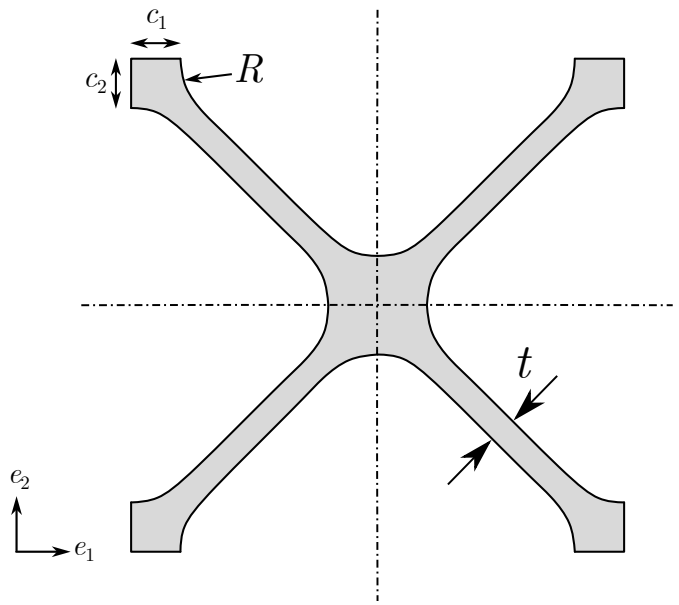

Figure 3.7: *Slender* unit cell

Table 3.3: Geometrical parameters of the *slender* unit cell's features. For the other dimensions see Table 3.1.

	Value	Unit
c_1	1	mm
c_2	1	mm
t	0.5	mm
R	1.56	mm

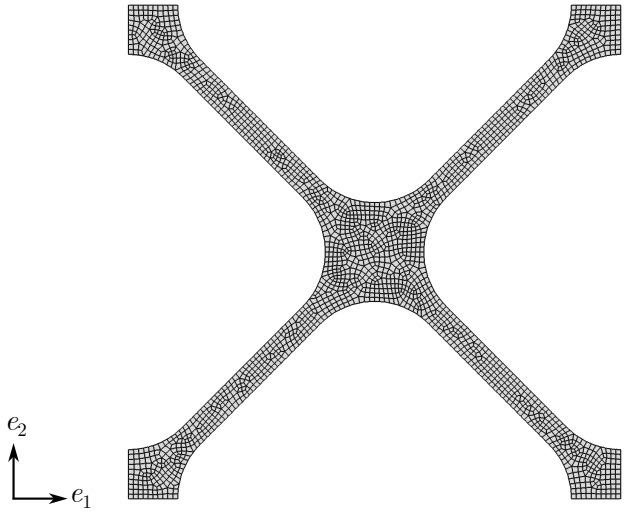

Figure 3.8: Mesh of the continuum model of the *slender* unit cell.

3.8. As a whole, 2078 continuum elements are used.

The beam model is built using a specific modeling technique. Here, each half-strut of the unit cell is divided into six distinct sections with the goal of modeling the change in thickness along the strut length. Each section is assigned different properties, namely different material and geometrical parameters. Then, through mirroring, exploiting the symmetrical properties of the *slender* unit cell, the rest of the beam model is constructed. To properly explain the sections, they are numbered from one to six, starting with the outermost section of the half-srut, see Figure 3.9.

Section 1, marked in black, is the section that defines the end of the half-struts and, therefore, as a result of the symmetry, also the center of the unit cell. For this section linear elastic material properties are chosen with a significantly increased Young's modulus. The aim is to make this section considerably stiff as this is the domain of material aggregation, and thus no significant superelastic deformations are predicted there. Although a slight loss of information is expected, it is deemed insignificant and worth the reduction in the computational power required to run the simulation. For the remaining five sections, the effects of superelasticity are expected, and thus the superelastic models are used.

The gradual change in strut thickness is modeled via Section 2 to Section 5. Here, the total span $L_R = 1.1\text{mm}$ in which the thickness transitions from 1.41 to 0.5 is subdivided into four segments of equal length. Then each section is assigned the thickness equal to the thickness at the midpoint of the corresponding segment belonging to the non-simplified geometry. Lastly, the remaining Section 6 represents the segment where the thickness of the strut remains constant. The numerical values

of the thicknesses assigned to each individual section are given in Table 3.4.
For the beam model, the beam orientation is the same as for the *cross* unit cell. The mesh of the beam model is constructed with the same element type as the *cross* unit cell, and in sum 288 elements are used.

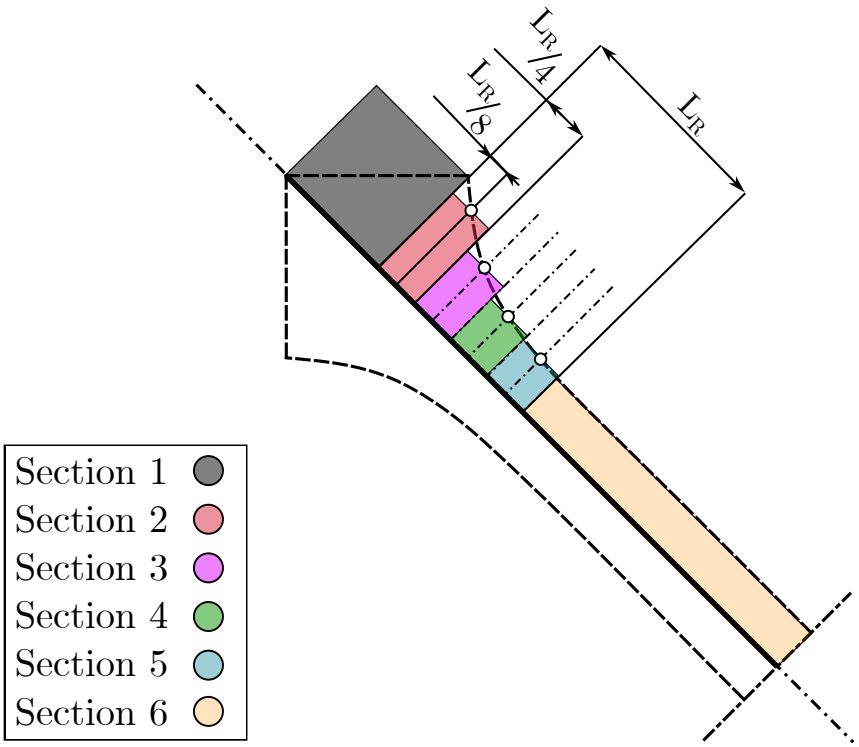

Figure 3.9: Detailed view on the half-strut of the *slender* unit cell. The black dashed line and the solid black line represent the shape of the continuum model and beam model, respectively. The colored segments spanning over L_R represent the different sections assigned to the beam model.

Table 3.4: Characteristics of each section assigned to the beam model of the *slender* unit cell.

	h [mm]	t [mm]	Material
Section 1	1	1.41	linear elastic
Section 2	1	1.16	superelastic
Section 3	1	0.82	superelastic
Section 4	1	0.62	superelastic
Section 5	1	0.52	superelastic
Section 6	1	0.5	superelastic

3.2.3 Slender Compliant Unit Cell

The *slender compliant* unit cell is the third variant of the unit cell. Its shape is based on the *slender* unit cell, which means that the same modeling technique to mimic the roundings transitioning to the smaller strut thickness is applied. However, the *slender compliant* unit cell differs from the *slender* unit cell by the design of its center. As for this unit cell design, the point at which the struts intersect is rotated by 45° introducing increased rotational compliance to the model, see Figure 3.10. Contrary to the two previous variants, this unit cell does not exist as a continuum model but is only modeled using beam elements. Similarly to the beam model of the *slender* unit cell, the struts are subdivided into six sections. The sections have the same material characteristics and lengths as for the *slender* unit cell with the exception of Section 6, which is slightly extended. This is a result of the introduced rotation of the cell center, as this leads to a slight lengthening of the struts. The modeling technique is schematically depicted in Figure 3.11. The beam orientation is set according to Figure 3.12, i.e. in a similar manner as for the *cross* unit cell and the *slender* unit cell. For the generation of the mesh, the number of elements used adds up to 882.

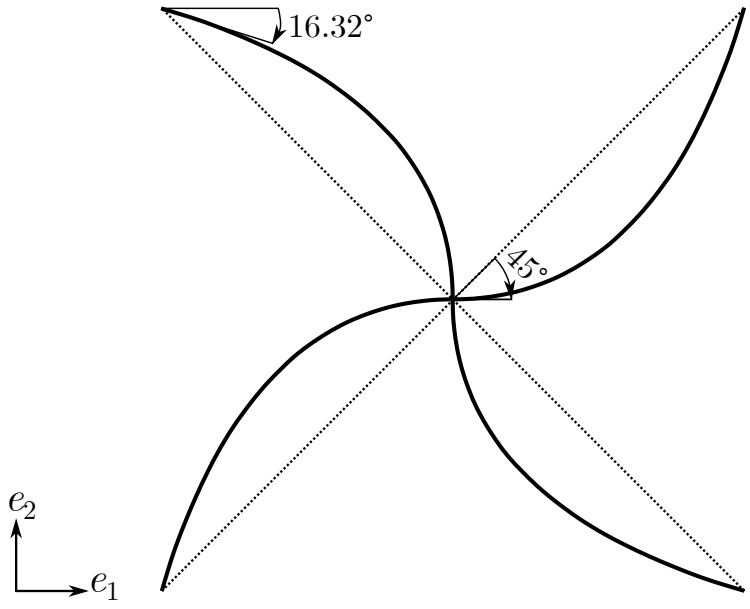

Figure 3.10: Juxtaposition of the beam model of the *slender* unit cell (dotted line) and the beam model of the *slender compliant* unit cell (solid line). The relative rotation of 45° of the unit cell center between both cells is indicated.

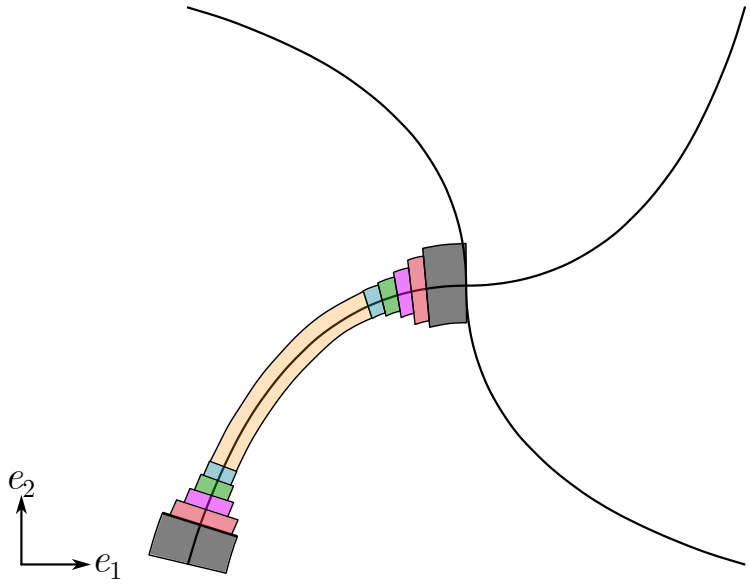

Figure 3.11: Modeling strategy used on the *slender compliant* unit cell. For reasons of clearness, the approximation method is only displayed on one of the four struts.

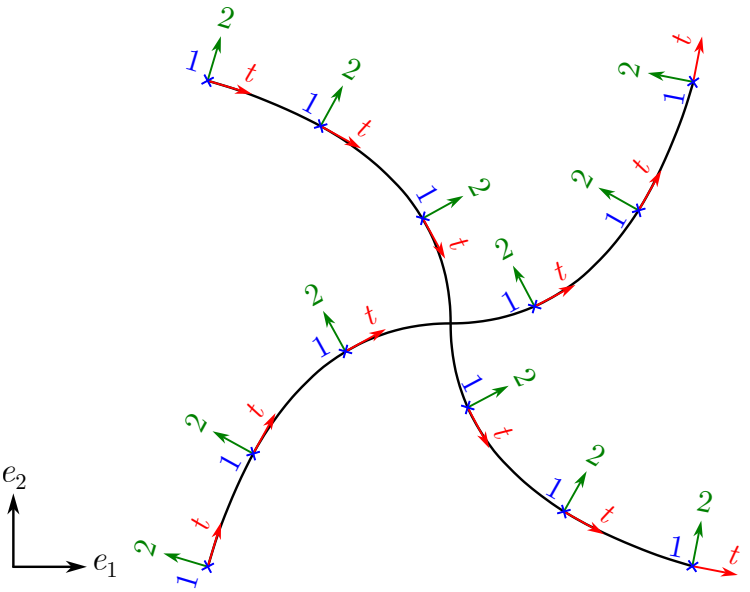

Figure 3.12: Beam orientation of the *slender compliant* unit cell.

3.3 Material Parameters

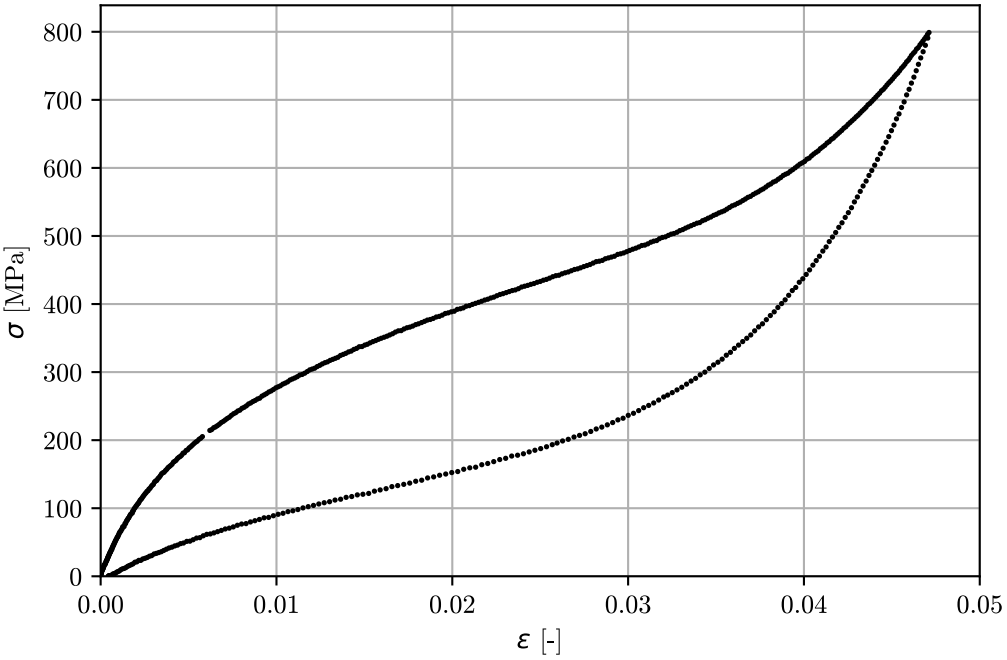

Figure 3.13: Experimental data of the stress-strain response of the parent material. The data set was captured by project partners at the Insitute of Machine and Industrial Design, Brno University of Technology.

To properly characterize the material models used in this work, a set of different material parameters is required. These parameters differ based on the material models, as each model is implemented differently. The calibration of those parameters is based on the experimental data set from Figure 3.13, which is also used in the work of Schasching et al. [7]. As a result, the values for the ASM and UHYP-POLY model are identical to theirs, which ensures that a proper comparison can be made.

3.3.1 Abaqus Standard Material Model for Superelasticity

Since the martensitic transformation is the basis of superelastic behavior, the material properties of the austenite phase, as well as the martensite phase, must be defined. *ABAQUS* requires for the austenite phase and the martensite phase their respective Young's modulus and Poisson ratio. Furthermore, to successfully simulate the superelastic material behavior, a set of parameters is needed which characterize the martensitic transformation, such as the stress at which the transformation starts during loading and the transformation strain. A summary of all the material properties used is given in Table 3.5.

Table 3.5: Material parameters used for the Abaqus superelastictiy model.

	Value	Unit
E_A - Young's Modulus austenite	100000	MPa
ν_A - Poisson ratio austenite	0.3	[-]
E_M - Young's modulus martensite	70000	MPa
ν_M - Poisson ratio martensite	0.3	[-]
ε_t - Transformation strain	0.034	[-]
σ_{tL}^S - Start of transformation (loading)	251.37	MPa
σ_{tL}^E - End of transformation (loading)	574.34	MPa
σ_{tU}^S - Start of reverse transformation (unloading)	213.68	MPa
σ_{tU}^E - End of reverse transformation (unloading)	35.7	MPa
σ_{cL}^S - Start of reverse transformation in compression (loading)	251.37	MPa

3.3.2 Hypoelastic Polynomial Fitted Material Model for Superelasticity

As already discussed in Section 2.6.2 in which the UHYP-POLY model is introduced, the `UHYPEL` interface in conjunction with beam elements requires the tangential Young's modulus and the Poisson ratio. Due to the conditional based implementation of the UHYP-POLY model, its response is characterized by the three tangential Young's moduli: $E_{tU;T}$, $E_{tL;T}$, and E_M. They are defined through the coefficients a, b, c, and d from Table 3.6, using Equation (2.34) which reads $E_T(\varepsilon) = 3a\varepsilon^2 + 2b\varepsilon + c$ for the transition phase, and $E_M = d$ for the martensite phase. The Poisson ratio is assumed to be constant and equates to $\nu = 0.3$.

Table 3.6: Material parameters used for the UHYP-POLY model.

Young's Moduli	coefficients			
	a	b	c	d
$E_{tL;T}$	25791426	-1790820	45940	
E_M				67159
$E_{tU;T}$	23729021	-1082987	17937	

3.3.3 Hypoelastic Multilinear Material Model for Superelasticity

Table 3.7: Material parameters used for the UHYP-MLIN model.

Young's Moduli	coefficient d
E_A	100000
$E_{tL;T}$	8143.2
E_M	70084.656
$E_{tU;T}$	4840.176

Since the UHYP-MLIN model is described by four constant Young's Moduli the coefficient d directly equates to their respective values. They are summarized in Table 3.7. Identical to the previous material models, the Poisson ratio is assumed to be constant and equates to $\nu = 0.3$.

3.4 Load Cases and Boundary Conditions

In the following section, the different load cases are presented that are used to verify the different material models. To properly identify and describe the nodes and edges subjected to various conditions, the notation system based on the cardinal directions mentioned in Section 2.1, is used.

As the goal is to determine the homogenized stresses of the superordinate lattice structures, the setting of adequate boundary conditions is essential. Whether symmetry boundary conditions are sufficient or periodicity boundary conditions are required depends on the symmetry properties of the loading scenarios and the geometry of the chosen unit cells. In this work, uniaxial tension and pure shear loading scenarios are considered.

As superelastic material is generally characterized by its stress-strain hysteresis, a load-unload cycle for each load case is evaluated.

Each load is applied in a single step, which means that the load must vary over time. The load variation is defined such that it linearly ramps up, reaching the full magnitude at $t = 0.5$s, and then linearly ramps down again to zero at $t = 1$s. This loading process is used for each analysis performed, unless stated otherwise.

For all the analyses performed in this work, the Newton-Raphson solution procedure is used, and geometric nonlinearities considered.

3.4.1 Uniaxial Tension

First, uniaxial tension scenarios are presented for the continuum models. Here, only the *slender* unit cell is used to present the boundary conditions of the continuum model, as its constraints are identical to those of the *cross* unit cell continuum model. As shown in Figure 3.14, for the continuum model, the degrees of freedom in the 1-direction are locked along the left edge denoted by W. Whereas, the degrees of freedom of the nodes along edge S are locked in the 2-direction. A displacement U_1 of $L_1/10$ is prescribed at node SE to achieve a tensile strain of 0.1 at maximum applied load. Since both continuum models possess mirror symmetry with respect to the 1- and 2-axes and since the uniaxial tension load case is symmetric too, symmetry boundary conditions suffice for the proper evaluation of the models. This means that for the nodes located on edge E, their degree of freedom in the 1-direction is coupled to the leader node SE. Thus, they are also subjected to the displacement U_1. Whereas, the degree of freedom in the 2-direction of the nodes on edge N is coupled to the leader node NW.
For the sake of clarity, the boundary conditions and the couplings of the individual nodes are summarized in Table 3.8.

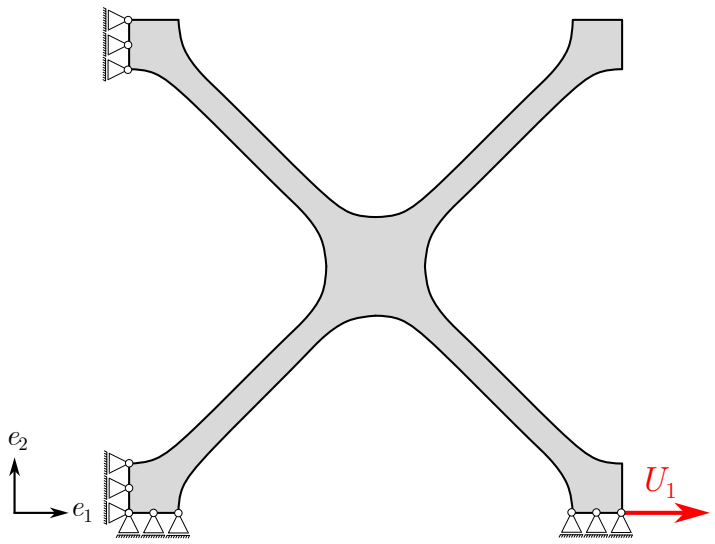

Figure 3.14: Schematics of the uniaxial tension load case with symmetry boundary conditions for the continuum model of the *slender* unit cell. The same conditions apply to the continuum model of the *cross* unit cell.

Table 3.8: The symmetry boundary conditions applied to the continuum models (*cross* unit cell and *slender* unit cell) for the case of uniaxial tension. The starred nodes, NW and SE, are the "leader nodes".

Node	Edge	u_1	u_2	u_{R3}
NW*		0	-	-
NE		$= u_{1\|SE}$	$= u_{2\|NW}$	-
SE*		1	0	-
SW		0	0	-
	N	-	$= u_{2\|NW}$	-
	E	$= u_{1\|SE}$	-	-
	S	-	0	-
	W	0	-	-

With respect to the boundary conditions of the symmetrical beam models, a nearly identical approach is chosen. Here, the node SW is locked both in the 1- and 2-direction. Whereas, the node NW has its degree of freedom in 1-direction locked. The node SE located on the bottom right has its degree of freedom in the 2-direction locked. Furthermore, a displacement U_1 in the 1-direction is applied to it, see Figure 3.15. Lastly, each node located on the border domain of the unit cell has their out-of-plane rotational degree of freedom locked.

Here, symmetry boundary conditions are sufficient as well, and thus the couplings are similar to those of the continuum models. That is, the same leader nodes SE and NW each impose their displacement on the follower node NE. Where the node NE is coupled via the degree of freedom in the 1-direction to the node SE and via the degree of freedom in the 2-direction to the node NW.

A summary of the boundary conditions is given in Table 3.9.

Regarding the boundary conditions of the beam model of the *slender compliant* unit cell, the symmetry boundary conditions are no longer applicable due to the asymmetry of the model with respect to the 1-2 coordinate system. Therefore, periodicity boundary conditions must be applied. As a result, three leader nodes exist now, i.e. the node NW, SE and SW. For both the degree of freedom in the 1- and 2-direction, node NE is coupled to node NW and SE in such a way that its displacements in those directions equal the sum of the two. Furthermore, the out-of-plane rotational degree of freedom of the nodes located on the border domain are no longer locked but an additional coupling of degree of freedom is introduced. Here, the node NW, NE and SE follow the rotations of the node SW. Table 3.10 summarizes the boundary conditions for uniaxial tension for the *slender compliant* unit cell.

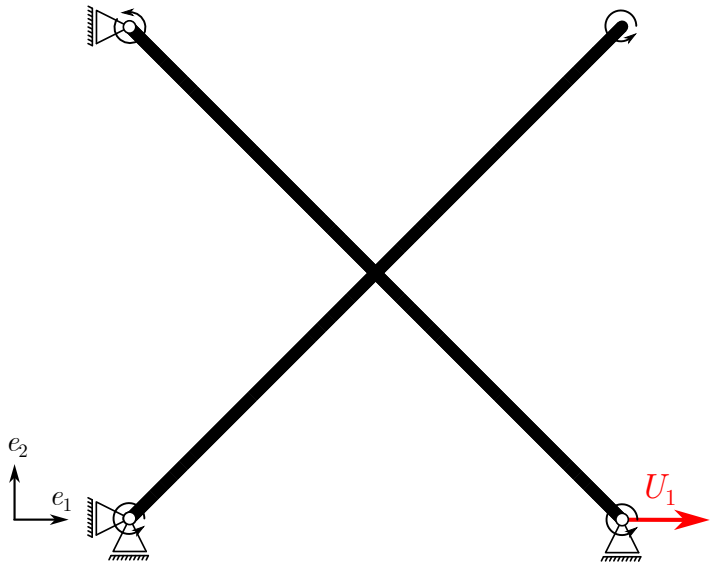

Figure 3.15: Schematics of the uniaxial tension load case with symmetry boundary conditions for the beam model of the *cross* and *slender* unit cells.

Table 3.9: The symmetry boundary conditions applied to the symmetrical beam models (*cross* unit cell and *slender* unit cell) for the case of uniaxial tension. The starred nodes, NW and SE, are the "leader nodes".

Node	u_1	u_2	u_{R3}
NW*	0	-	0
NE	$= u_{1\|SE}$	$= u_{2\|NW}$	0
SE*	1	0	0
SW	0	0	0

Table 3.10: The periodicity boundary conditions applied to the beam model of the *slender compliant* unit cell for the case of uniaxial tension. The starred nodes, NW, SE and SW, are the "leader nodes".

Node	u_1	u_2	u_{R3}
NW*	0	-	$= u_{R3\|SW}$
NE	$= u_{1\|NW} + u_{1\|SE}$	$= u_{2\|NW} + u_{2\|SE}$	$= u_{R3\|SW}$
SE*	1	0	$= u_{R3\|SW}$
SW*	0	0	-

3.4.2 Pure Shear

As for the pure shear loading scenario, different boundary conditions apply. This load case is only applied to the beam models of the *slender* unit cell and the *slender compliant* unit cell. Here, only the node SW is fixed by having its degree of freedom in the 1- and 2-direction locked. A total of two displacements are prescribed, U_1 and U_2, which equal to $L_1/10$ and $L_2/10$, respectively. The former displacement is applied at node NW whereas the latter displacement is applied at node SE, see Figure 3.16. These specific values are chosen for the displacements to achieve a shear strain of 0.1 at maximum applied load. Since the pure shear loading scenario shows no symmetry with respect to the principal directions of the main coordinate system, periodicity boundary conditions must be applied. They are defined as previously for the beam model of the *slender compliant* unit cell. For reasons of clearness, the boundary conditions and the coupling of the nodes are summarized in Table 3.11.

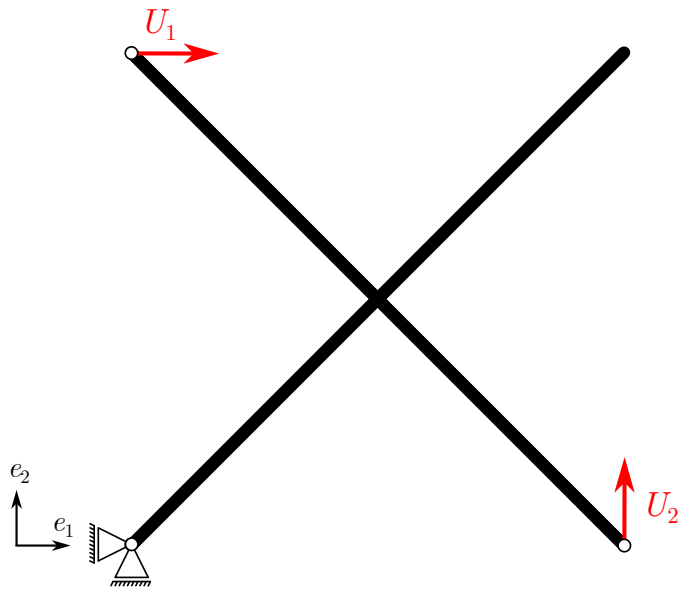

Figure 3.16: Schematics of the pure shear load case with periodicity boundary conditions for the beam model of the *slender* unit cell. The same conditions apply for the *slender compliant* unit cell.

Table 3.11: The periodicity boundary conditions applied to the beam models (*slender* unit cell and *slender compliant* unit cell) for the case of pure shear. The starred nodes, NW, SE and SW, are the "leader nodes".

Node	u_1	u_2	u_{R3}
NW*	1	-	$= u_{R3\|SW}$
NE	$= u_{1\|NW} + u_{1\|SE}$	$= u_{2\|NW} + u_{2\|SE}$	$= u_{R3\|SW}$
SE*	-	1	$= u_{R3\|SW}$
SW*	0	0	-

3.4.3 Beam Buckling and Sensitivity Analysis

For the *slender* unit cell, in the case of pure shear, buckling is expected due to the increased compressive stress in the strut connecting both corner nodes NW and SE, invoked by that type of load case. As a result, a small perturbation moment is introduced to investigate the non-trivial bifurcation path. The moment M_p is applied to the center of the unit cell, acting in the negative out-of-plane direction. This perturbation moment is applied in the same load step as the displacement. Thus, to investigate the influence of the perturbation moment on the deformation behavior of the unit cell at the load reversal point, two different load-time variatons are considered. They are presented in Figure 3.17 and Figure 3.18, where the first figure illustrates the scenario in which the imposed imperfection ramps down before the load reversal point is reached, and the second figure the case in which the perturbation moment ramps down when the load reversal point has already been passed. For the sake of simplicity, throughout the rest of this thesis, the former load-time variation is referred to as the pre-load amplitude, while the latter is referred to as the post-load amplitude.

Finally, a sensitivity analysis is conducted to investigate the influence of the perturbation moment on the structural behavior of the unit cell. This is achieved by doing multiple analyses, starting with an adequately large perturbation moment, and then reducing the amplitude of the perturbation for each subsequent analysis incrementally until convergence issues arise.

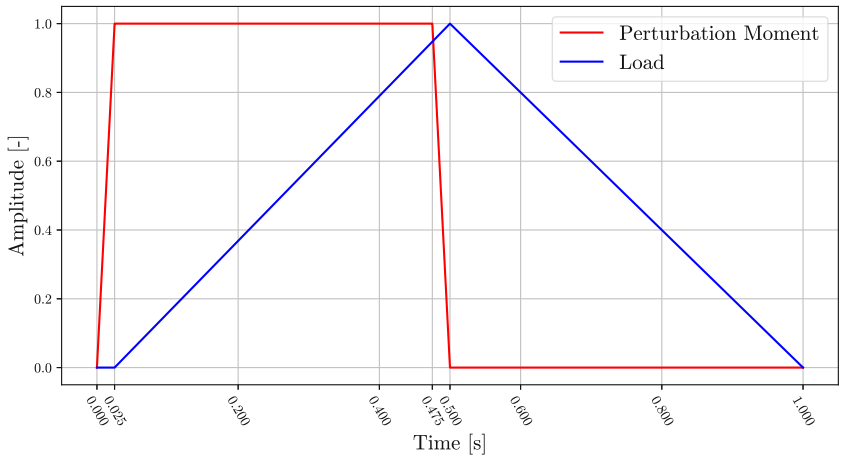

Figure 3.17: Amplitude plotted against time. The plot in red shows the amplitude of the perturbation moment. The plot in blue shows the amplitude of the load. The perturbation moment ramps down before the load reversal point is reached.

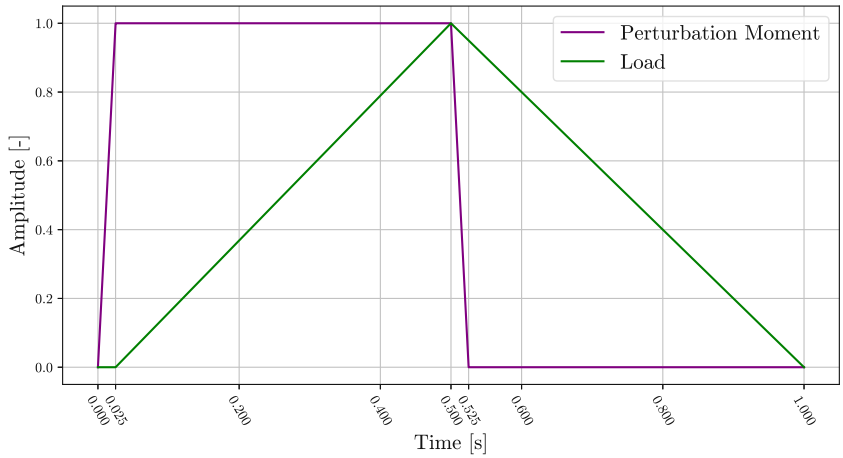

Figure 3.18: Amplitude plotted against time. The plot in red shows the amplitude of the perturbation moment. The plot in blue shows the amplitude of the load. The perturbation moment ramps down after the load reversal point is reached.

3.5 Comparison-based Verification Framework

The verification of the modeling strategies and the UHYPEL-based material models requires an appropriate process. This section aims to provide a framework that guides through the different comparisons, their reasoning, and establishes a logical connection among them.

The verification process comprises a total of seven comparisons (or verification steps), summarized in Table 3.12. Starting with the *cross* unit cell, for the load case of uniaxial tension, the stress-strain response of the continuum model is compared to the response of the beam model. In doing so, the quality of the results of the beam model is examined to determine if the use of exclusively beam models suffices for subsequent comparisons involving the hypoelastic material models. In a second comparison, for the beam model of the *cross* unit cell and for the load case of uniaxial tension, the three superelasticity material models are compared against each other. With this comparison, it is intended to verify the UHYPEL-based material models for that specific variant of unit cell and load case.

Following this, the modeling strategy applied for the creation of the beam model of the *slender* unit cell is intended to be verified by comparing it with its continuum-based equivalent. This comparison is only conducted in uniaxial tension and only with the ASM model. The fourth comparison is similar to the second, as it also covers the uniaxial tension load case for each material model, however, this time it is based on the *slender* unit cell. Subsequently, the same comparison is conducted for the pure shear load case.

The last two comparisons handle the verification of the hypoelastic material models for the *slender compliant* unit cell. First, in uniaxial tension, bASM, UHYP-POLY

and UHYP-MLIN are juxtaposed. Then, they are compared once more for the pure shear load case.

Table 3.12: Overview of the comparisons conducted with the aim of verifying the modeling strategies and the UHYPEL-based material models.

N°	Load Case	Analysis	Aim of Comparison
1	Uniaxial Tension	*cross* UC - cASM *cross* UC - bASM	confirm that beam modeling is sufficient
2	Uniaxial Tension	*cross* UC - bASM *cross* UC - UHYP-MLIN *cross* UC - UHYP-POLY	verification of material models
3	Uniaxial Tension	*slender* UC - cASM *slender* UC - bASM	verification of modeling strategy
4	Uniaxial Tension	*slender* UC - bASM *slender* UC - UHYP-MLIN *slender* UC - UHYP-POLY	verification of material models
5	Pure Shear	*slender* UC - bASM *slender* UC - UHYP-MLIN *slender* UC - UHYP-POLY	verification of material models
6	Uniaxial Tension	*slender compliant* UC - bASM *slender compliant* UC - UHYP-MLIN *slender compliant* UC - UHYP-POLY	verification of material models
7	Pure Shear	*slender compliant* UC - bASM *slender compliant* UC - UHYP-MLIN *slender compliant* UC - UHYP-POLY	verification of material models

4 Results and Discussion

In the following chapter, the results of the conducted analyses are presented and discussed. The presentation of the results is structured in line with the comparison-based verification framework. This means that a set of comparisons is presented with the main goal of verifying the UHYPEL-based material models. Each comparison comprises in total two investigations.
This means that first the homogenized stress-strain curves with the individual material models are studied. Then, the transformation strain contour plots are studied at two distinct strain states; (1) the state of first full local transformation and (2) the state at which the maximum load is applied. The comparisons are based on two load cases, i.e. the uniaxial load case and the pure shear load case.
For both load cases, the stresses and strains are determined via the method discussed in Section 2.2.
All the *ABAQUS* input files that were used to generate the figures in this chapter can be found at DOI: 10.5281/zenodo.14887805 .

4.1 Verification Step 1

The first step in the verification process constitutes in identifying the differences between the cASM and the bASM model of the *cross* unit cell for the uniaxial load case with the aim of determining the applicability of beam models when studying lattice structures with superelastic parent material.

4.1.1 Investigation of the Stress-strain Relation

Figure 4.1 shows the stress-strain curve obtained for both the bASM and the cASM model. Throughout the entire loading procedure, the beam model displays reduced stiffness resulting in a considerable deviation in stress at maximum strains from its continuum counterpart. A relative stress error of -17.9% is captured at $\varepsilon_{11} = 0.1$. This difference in stress is most likely linked to the beam model's inability to factor in the material aggregations that form at the intersection of the struts.
During unloading, and especially in the retransformation regime, the behavior of the beam model agrees well with that of the continuum model.

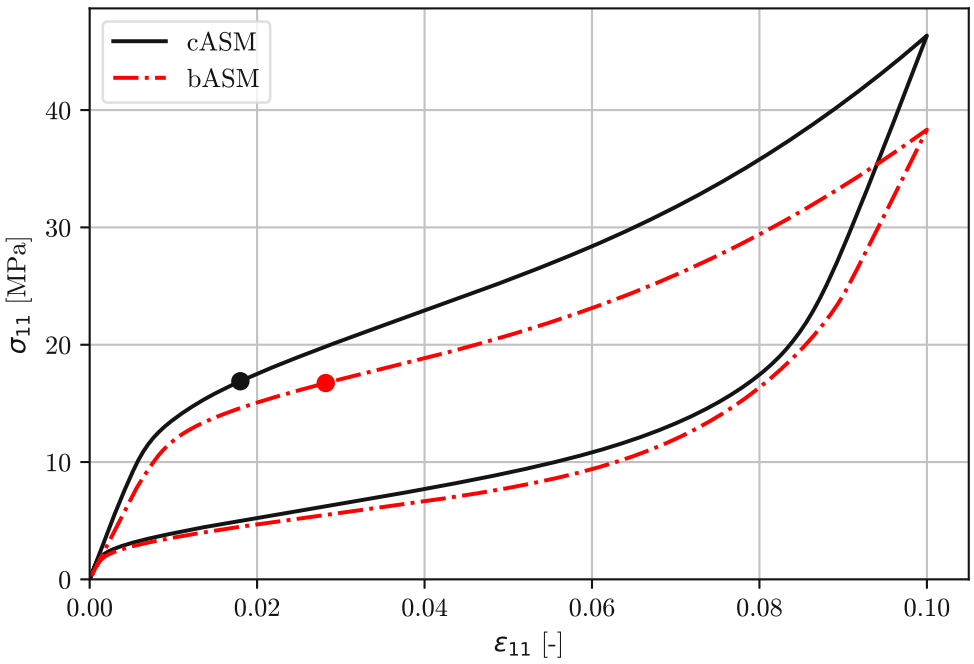

Figure 4.1: Stress-strain curves of the two models, cASM and bASM, for the uniaxial tension load case of the *cross* unit cell. The two point markers indicate the state of first full local transformation for each individual material model.

4.1.2 Evaluation of the Transformation Zone

Figures 4.2 to 4.5 show the maximum in-plane principal transformation strains at two distinct strain states for the cASM and the bASM model. The two markings in Figure 4.1 serve as an indicator to locate the corresponding contour plots of Figure 4.2 and Figure 4.3 in the stress-strain curves. Note that the legends in the corresponding figures display as strain measure *TE, Max. In-Plane Principal (Abs)*. This specific measure is chosen, with emphasis on the notion *(Abs)*, as with this option, both the information provided by the *Max. In-plane Principal* strain measure and the *Min. In-Plane Principal* strain measure is included, and thus, showing both the compressive and tensile strains in one contour.
The first strain state indicates full local transformation. The contours of Figure 4.4 to Figure 4.5 confirm that the first full local transformation is in the same regions for both models. Interestingly, these regions of fully transformed material appear for both the cASM and the bASM models at different strains but at close stress levels. At maximum load, the contours show a consistent strain distribution. The evaluation of both contour plots reveals the development of the strains throughout the loading scenario, which start from the outermost region of each individual strut and evolve towards the center of the strut.

4.1.3 Remarks

The results suggest that the beam model is capable of representing the *cross* unit cell with adequate accuracy. However, an adjusted modeling strategy is desired to compensate for the shortcomings regarding the missing representation of the material aggregation at the intersection point.

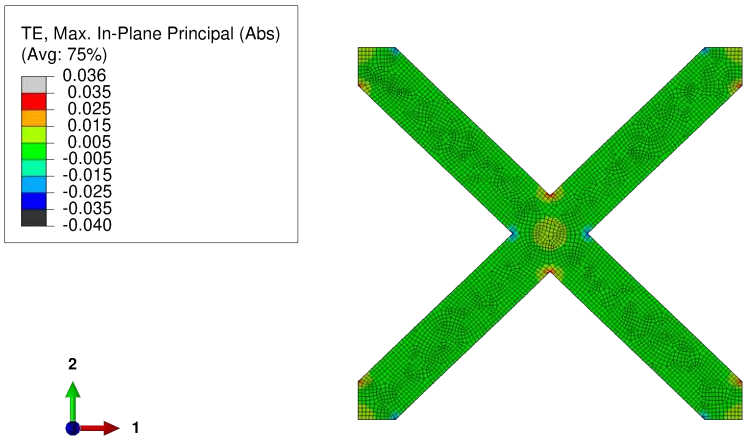

Figure 4.2: Uniaxial tension - Maximum in-plane principal transformation strain contour of the cASM model for the *cross* unit cell with a deformation scale factor of 1. The contour is evaluated at $\varepsilon_{11} = 0.018$. The upper (red) and lower (blue) limit of the legend indicate full transformation.

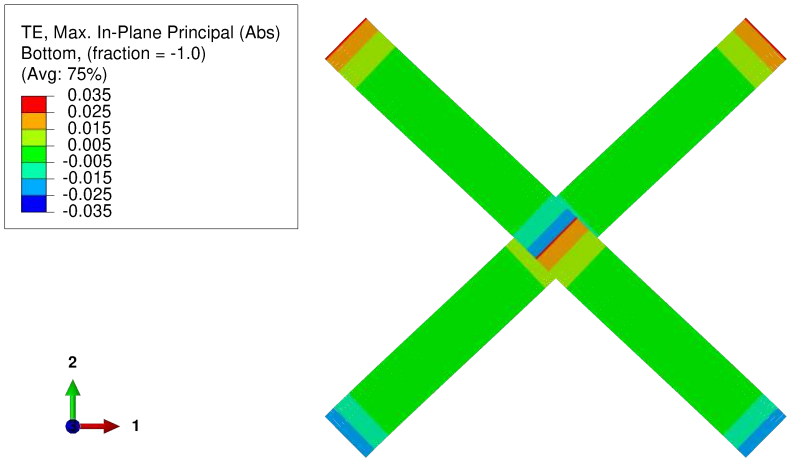

Figure 4.3: Uniaxial tension - Maximum in-plane principal transformation strain contour of the bASM model for the *cross* unit cell with a deformation scale factor of 1. The contour is evaluated at $\varepsilon_{11} = 0.0282$. The upper and lower limit of the legend indicate full transformation.

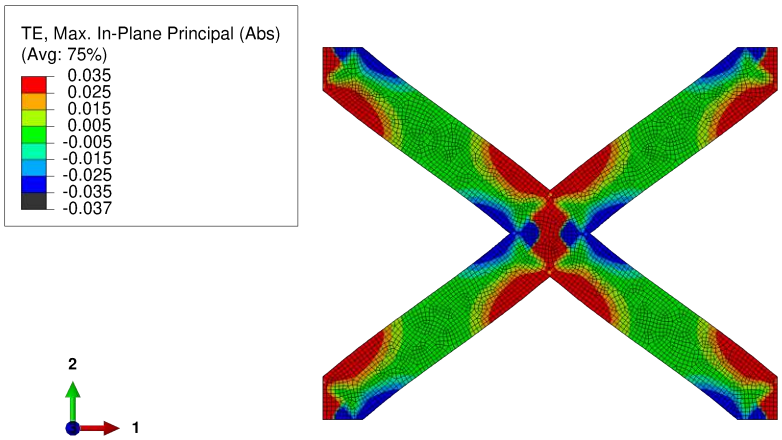

Figure 4.4: Uniaxial tension - Maximum in-plane principal transformation strain contour of the cASM model for the *cross* unit cell with a deformation scale factor of 1. The contour is evaluated at $\varepsilon_{11} = 0.1$. The upper (red) and lower (blue) limit of the legend indicate full transformation.

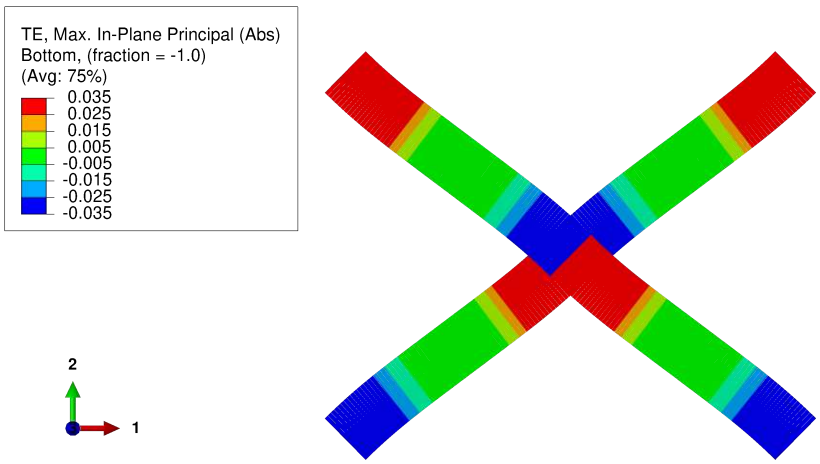

Figure 4.5: Uniaxial tension - Maximum in-plane principal transformation strain contour of the bASM for the *cross* model unit cell with a deformation scale factor of 1. The contour is evaluated at $\varepsilon_{11} = 0.1$. The upper and lower limit of the legend indicate full transformation.

4.2 Verification Step 2

In the following, the beam models, bASM, UHYP-MLIN, and UHYP-POLY are compared for the *cross* unit cell with the load case of uniaxial tension. This comparison serves as a first step in the verification of the `UHYPEL`-based material models.

4.2.1 Investigation of the Stress-strain Relation

The juxtaposition of the stress-strain curves of the three material models in Figure 4.6 reveals that both the bASM model and the UHYP-MLIN model are in good agreement in the low-loading regime. However, the UHYP-POLY model deviates quite visibly from the other two, showing nonlinear behavior right from the beginning. With increasing strains, all three material models converge, reaching nearly identical stress levels at maximum strains. In the unloading regime, the retransformation for the bASM model starts at higher stresses compared to the other two. The UHYP-POLY and the UHYP-MLIN model show parallel behavior during retransformation, but diverge in the low-loading regime. Upon approaching the austenite phase, the UHYP-MLIN model converges with the bASM model and ends with the same linear slope, while the UHYP-POLY model approaches the unloaded state in a nonlinear manner.
The nonlinearities observed in the low-loading regime during both loading and unloading come as expected, as the UHYP-POLY model is directly linked by polynomial-fit to the experimentally determined material data of the parent material shown in Figure 3.13.

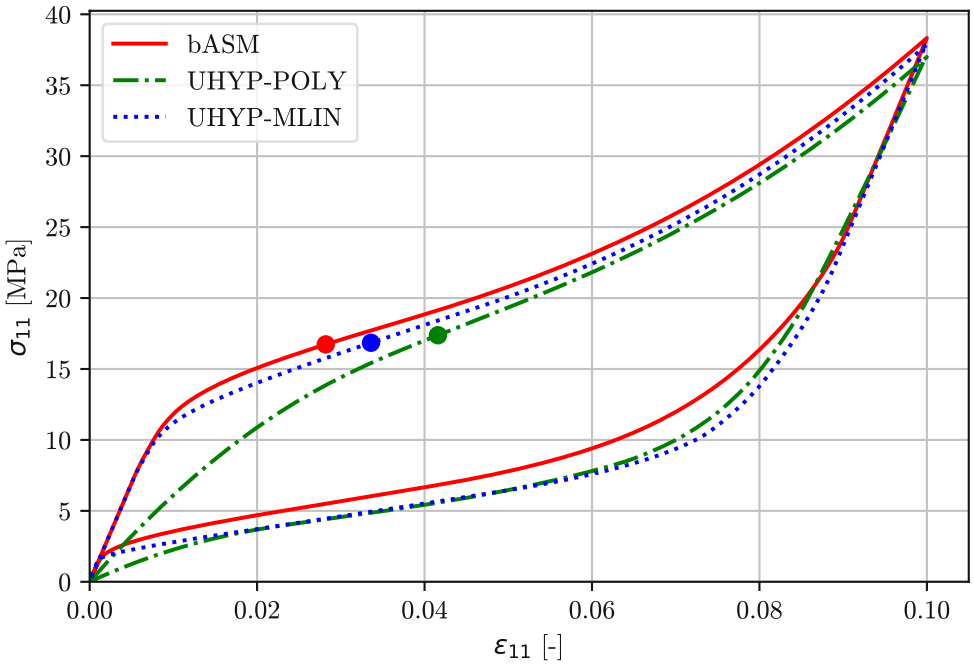

Figure 4.6: Stress-strain curves of the three models, bASM, UHYP-POLY, and UHYP-MLIN for the uniaxial tension load case of the *cross* unit cell. The three point markers indicate the state of first full local transformation for each individual material model.

4.2.2 Evaluation of the Transformation Zone

Before the strain contours are discussed, the different legends in Figure 4.8 and Figure 4.9 must be explained. For the contour plots of the UHYP-MLIN model, the legend displays *SDV_TE*, which is a strain measure exclusively implemented for that material model and which is equivalent to *TE, Max In-Plane Principal (Abs)*. Therefore, the same upper and lower limits are adopted.
The legend of the contour plots corresponding to the UHYP-POLY model display *SDV_INDICATORTRANSFORMED*. This measure is unique to that specific material model and indicates full transformation based on transformation strain measures. Thus, the upper and lower limit, 1.0 and -1.0, correspond to the transformation strains of 0.034 and -0.034, making it valid to compare with the other two.

Figures 4.7 to 4.9 show that for each material model, the regions of first full local transformation are close to identical. Similar to the previous comparison, the state of first full local transformation appears to be reached for each model at different strains but resembling stress levels, see markings in Figure 4.6. At maximum strains, the figures 4.10 to 4.12 show that there are no significant dissimilarities between the three models. This indicates that for the `UHYPEL`-based material models, the

strain evolution throughout the *cross* unit cell shows an analogous pattern to that previously described for the cASM and the bASM model.

4.2.3 Remarks

The UHYPEL-based material models are able to capture the uniaxial load case for the *cross* unit cell reasonably well. The most significant differences are observed in the case of the UHYP-POLY material model. They are rooted in the implementation of the material model itself and its inherent link to the nonlinear behavior of the parent material. Nevertheless, the results agree well with those reported by Schasching et al. [7] for the compression load case of the infinite lattice.

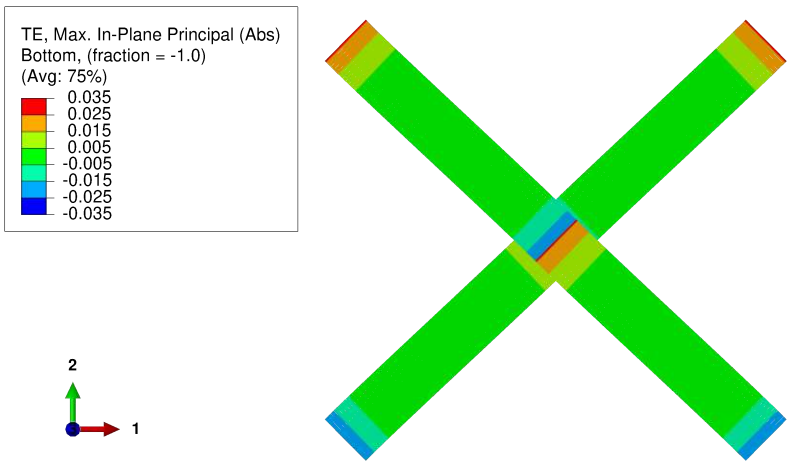

Figure 4.7: Uniaxial tension - Maximum in-plane principal transformation strain contour of the bASM model for the *cross* unit cell with a deformation scale factor of 1. The contour is evaluated at $\varepsilon_{11} = 0.0282$. The upper and lower limit of the legend indicate full transformation.

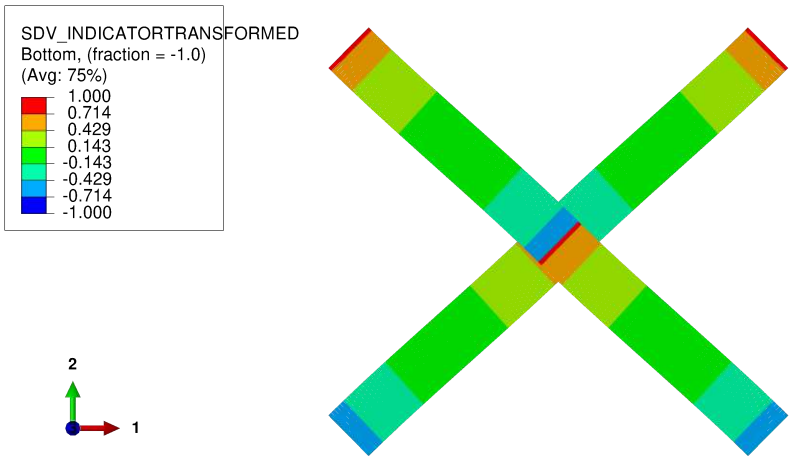

Figure 4.8: Uniaxial tension - Maximum in-plane principal transformation strain contour of the UHYP-POLY model for the *cross* unit cell with a deformation scale factor of 1. The contour is evaluated at $\varepsilon_{11} = 0.0416$. The upper and lower limit of the legend indicate full transformation.

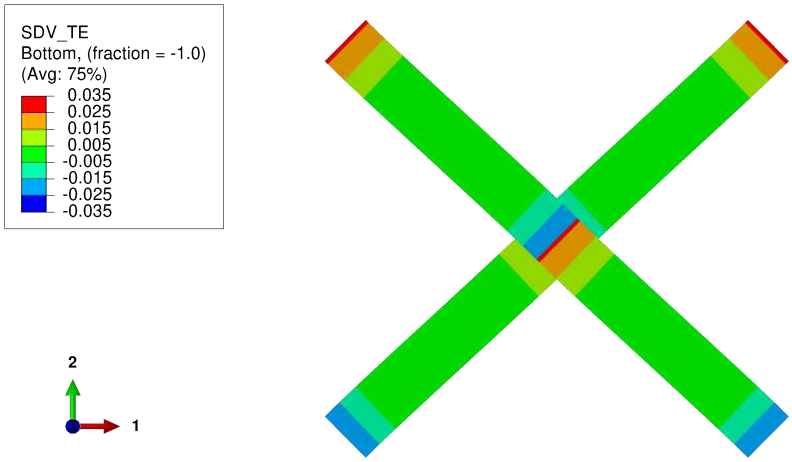

Figure 4.9: Uniaxial tension - Maximum in-plane principal transformation strain contour of the UHYP-MLIN model for the *cross* unit cell with a deformation scale factor of 1. The contour is evaluated at $\varepsilon_{11} = 0.0336$. The upper and lower limit of the legend indicate full transformation.

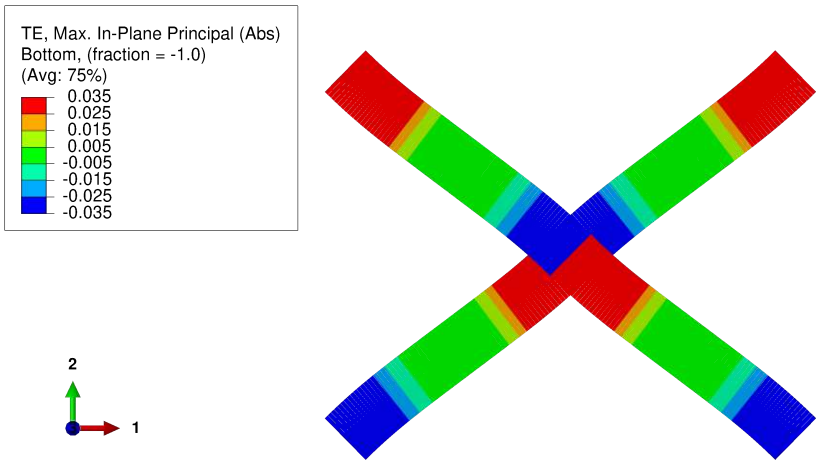

Figure 4.10: Uniaxial tension - Maximum in-plane principal transformation strain contour of the bASM model for the *cross* unit cell with a deformation scale factor of 1. The contour is evaluated at $\varepsilon_{11} = 0.1$. The upper and lower limit of the legend indicate full transformation.

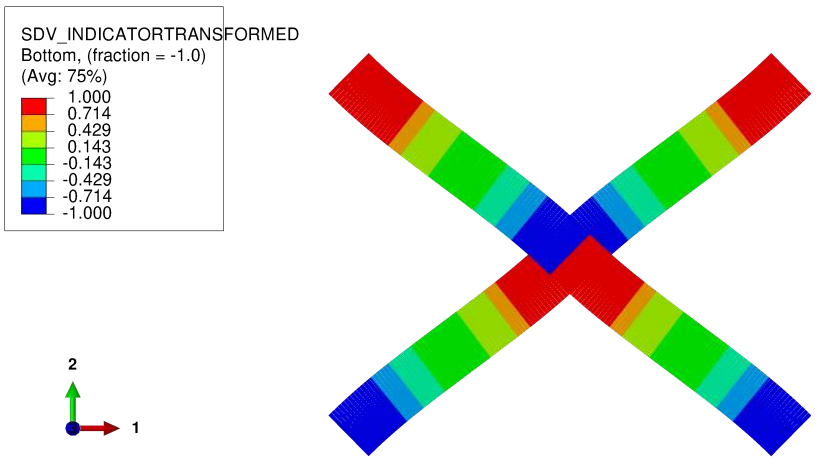

Figure 4.11: Uniaxial tension - Maximum in-plane principal transformation strain contour of the UHYP-POLY model for the *cross* unit cell with a deformation scale factor of 1. The contour is evaluated at $\varepsilon_{11} = 0.1$. The upper and lower limit of the legend indicate full transformation.

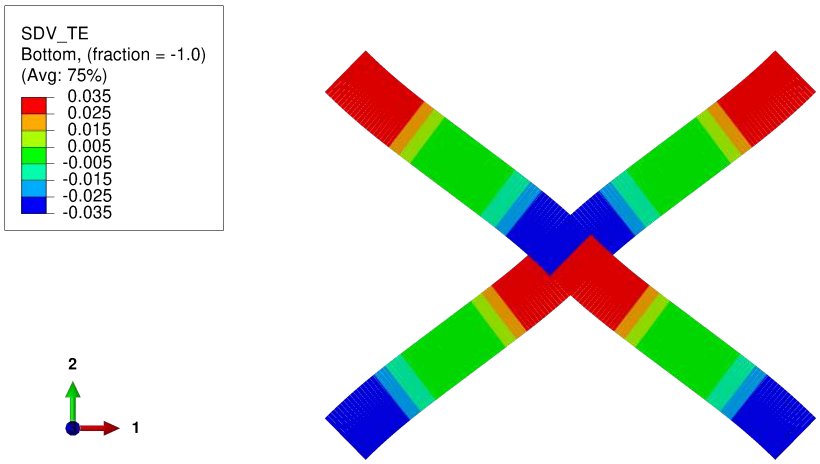

Figure 4.12: Uniaxial tension - Maximum in-plane principal transformation strain contour of the UHYP-MLIN model for the *cross* unit cell with a deformation scale factor of 1. The contour is evaluated at $\varepsilon_{11} = 0.1$. The upper and lower limit of the legend indicate full transformation.

4.3 Verification Step 3

To extend the verification of the UHYPEL-based material models, a more complex unit cell is studied, i.e. the *slender* unit cell. To confirm the modeling strategy applied to the beam model of the *slender* unit cell, the results of the cASM and the bASM model for the uniaxial tension load case are presented and compared.

4.3.1 Investigation of the Stress-strain Relation

The obtained stress-strain curves displayed in Figure 4.13 are in good agreement. The beam model shows marginally higher stresses at maximum strains with a relative error of 6.5% at $\varepsilon_{11} = 0.1$. This is a significant improvement as opposed to the beam model of the *cross* unit cell and comes as expected as with this modeling strategy, a region of high stiffness is introduced in the center and the outer corner regions of the unit cell. This compensates for the inability of the beam model to take into account the material aggregation at the intersection of the struts, as previously seen for the *cross* unit cell.
Regarding the unloading regime, no notable differences are visible between the two models.

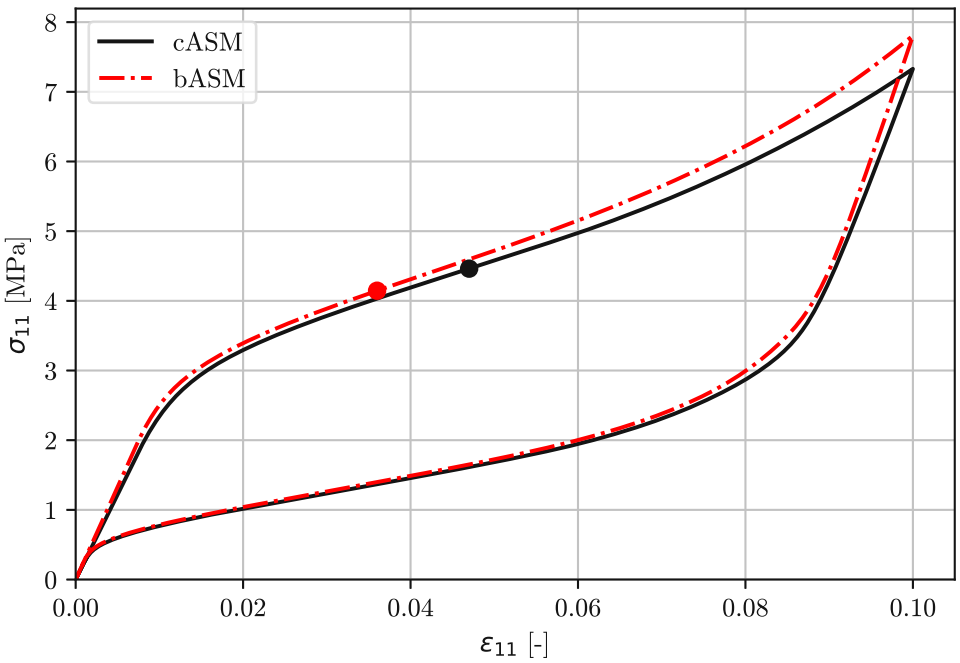

Figure 4.13: Stress-strain curves of the two models, cASM and bASM, for the uniaxial tension load case of the *slender* unit cell. The two point markers indicate the state of first full local transformation for each individual material model.

4.3.2 Evaluation of the Transformation Zone

Again, Figure 4.14 and Figure 4.15 show that the region in which full local transformation appears first is consistent across both models but occurs at different strain states. This time, although in relative close proximity, it cannot be stated that the homogenized stress levels are the same. At maximum strain, the contours are again in good agreement with each other, see Figure 4.16 and 4.17. The strain distribution for the *slender* unit cell starts at the end of the roundings, where the struts are lowest in thickness, and bending occurs. The strains then develop towards the center of the struts throughout the loading process.

4.3.3 Remarks

The contour plot of Figure 4.16 confirms the assumption of low strains in the center region. Thus, the choice of attributing the properties of linear elastic material with significantly increased stiffness to the center of the unit cell reflects the behavior of the structure quite well. The beam model in conjunction with the modeling strategy is thus, well suited for the upcoming verification processes of the `UHYPEL`-based material models. Note that the contour plot displays the region of linear elastic material in gray, as no transformation strains are computed in that region. This holds true for each of the following contour plots where this modeling strategy is applied.

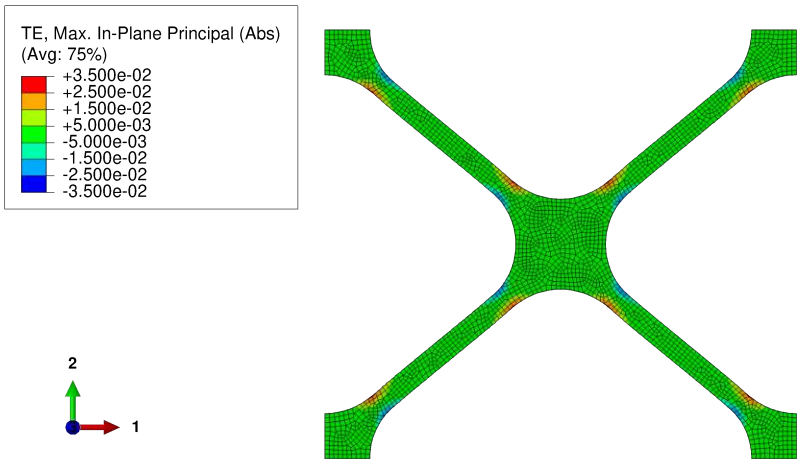

Figure 4.14: Uniaxial tension - Maximum in-plane principal transformation strain contour of the cASM model for the *slender* unit cell with a deformation scale factor of 1. The contour is evaluated at $\varepsilon_{11} = 0.047$. The upper and lower limit of the legend indicate full transformation.

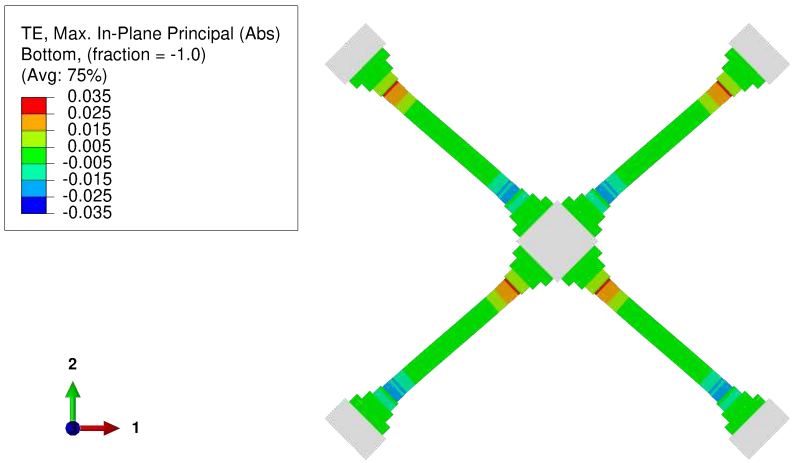

Figure 4.15: Uniaxial tension - Maximum in-plane principal transformation strain contour of the bASM model for the *slender* unit cell with a deformation scale factor of 1. The contour is evaluated at $\varepsilon_{11} = 0.036$. The upper and lower limit of the legend indicate full transformation.

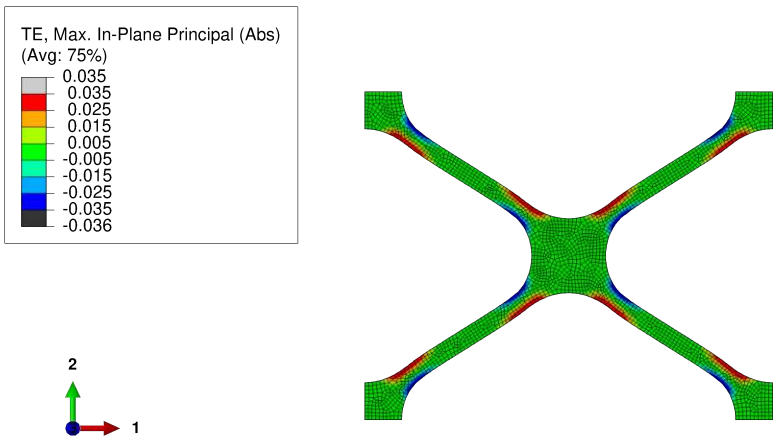

Figure 4.16: Uniaxial tension - Maximum in-plane principal transformation strain contour of the cASM model for the *slender* unit cell with a deformation scale factor of 1. The contour is evaluated at $\varepsilon_{11} = 0.1$. The upper (red) and lower (blue) limit of the legend indicate full transformation.

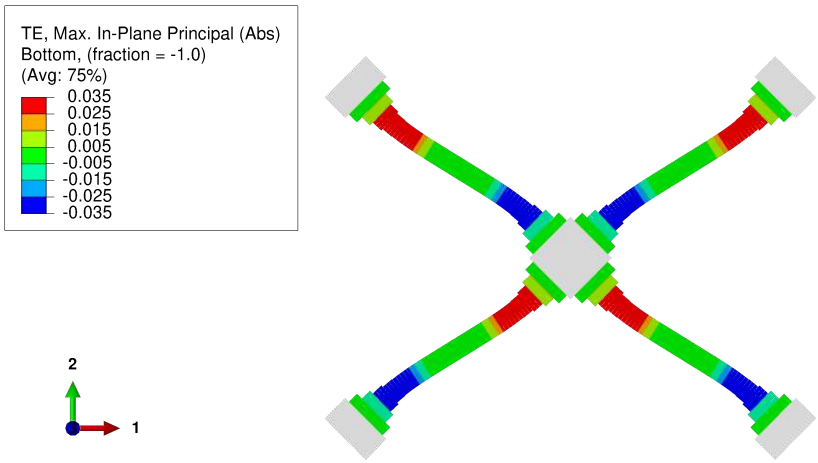

Figure 4.17: Uniaxial tension - Maximum in-plane principal transformation strain contour of the bASM model for the *slender* unit cell with a deformation scale factor of 1. The contour is evaluated at $\varepsilon_{11} = 0.1$. The upper and lower limit of the legend indicate full transformation.

4.4 Verification Step 4

As the modeling strategy for the *slender* unit cell is deemed applicable for further use, the UHYPEL-based material models are now investigated for that variant of the unit cell. More specifically, a comparison between the bASM and the UHYPEL material models is conducted for the load case of uniaxial tension.

4.4.1 Investigation of the Stress-strain Relation

The stress-strain relationship in Figure 4.18 shows similar differences as for the *cross* unit cell, that is, UHYP-MLIN and bASM are in the low-loading regime nearly identical while UHYP-POLY shows reduced stiffness and immediate nonlinear behavior in said regime. When approaching the point of maximum strains, the three material models yield converging stresses, with the bASM model reaching the highest stresses of the three.

In the unloading regime, the retransformation for the bASM model initiates first, an observation that has also been made for the *cross* unit cell, and which can thus be attributed to the ASM material model directly. The differences between the material models in the unloading regime are analogous to those previously observed for the *cross* unit cell, with the UHYP-MLIN and the UHYP-POLY being similar in the high strain regime, and dissimilar in the low strain regime. The nonlinear character of the UHYP-POLY model in the low-strain regime during loading and unloading traces back again to the behavior of the parent material and the material model's inherent link to it.

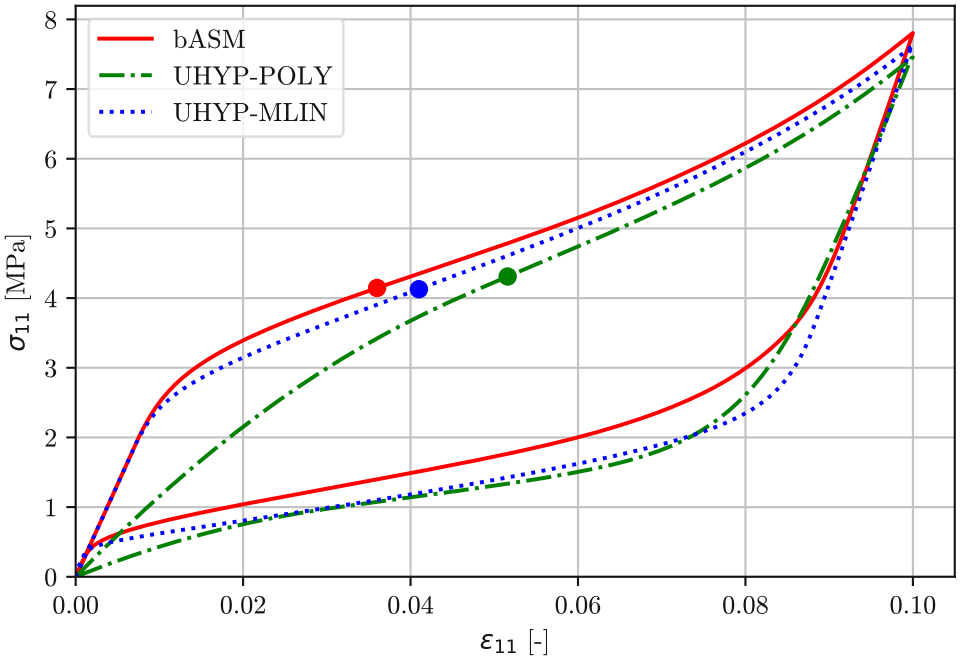

Figure 4.18: Stress-Strain curves of the three models, bASM, UHYP-POLY, and UHYP-MLIN for the uniaxial tension load case of the *slender* unit cell. The three point markers indicate the state of first full local transformation for each individual material model.

4.4.2 Evaluation of the Transformation Zone

The transformation strain contours of the corresponding material models are given once again at the two distinct strain states. Figures 4.19 to 4.21 show that there are no significant disparities between the three material models. Likewise to the *cross* unit cell, regions of first full local transformation appear for each material model at different strains, but nearly the same stress levels, see Figure 4.18. The evolution of the strain distribution remains the same for each material model, as just described for the cASM model of the *slender* unit cell.
At maximum strains, the three material models show no significant differences, see Figure 4.22 to 4.24.

4.4.3 Remarks

The UHYPEL-based material models have proven themselves capable of capturing the response of the more complex variant of the unit cell reasonably well. The reported differences mainly trace back to the implementation of the individual material models and how true their calibration is to the parent material.

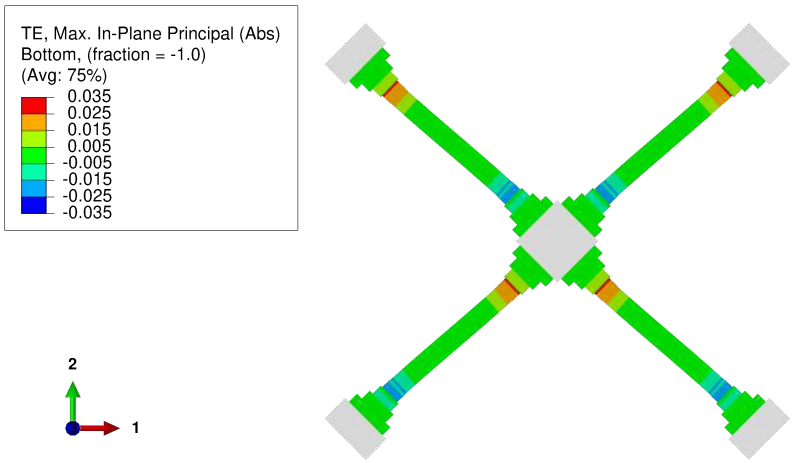

Figure 4.19: Uniaxial tension - Maximum in-plane principal transformation strain contour of the bASM model for the *slender* unit cell with a deformation scale factor of 1. The contour is evaluated at $\varepsilon_{11} = 0.036$. The upper and lower limit of the legend indicate full transformation.

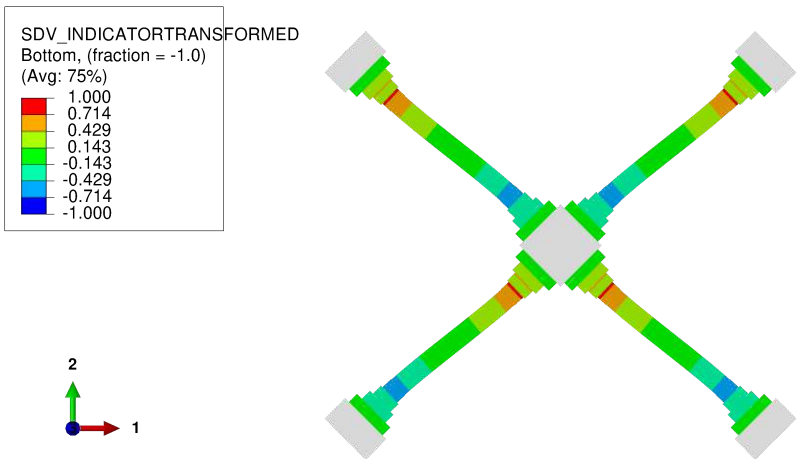

Figure 4.20: Uniaxial tension - Maximum in-plane principal transformation strain contour of the UHYP-POLY model for the *slender* unit cell with a deformation scale factor of 1. The contour is evaluated at $\varepsilon_{11} = 0.0516$. The upper and lower limit of the legend indicate full transformation.

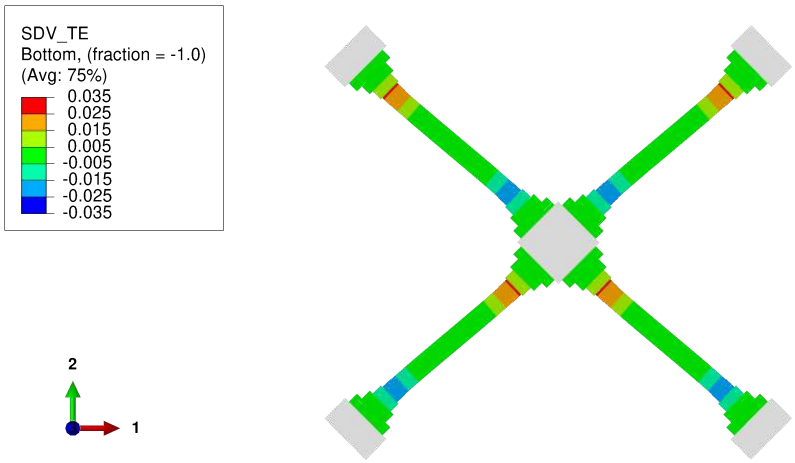

Figure 4.21: Uniaxial tension - Maximum in-plane principal transformation strain contour of the UHYP-MLIN model for the *slender* unit cell with a deformation scale factor of 1. The contour is evaluated at $\varepsilon_{11} = 0.041$. The upper and lower limit of the legend indicate full transformation.

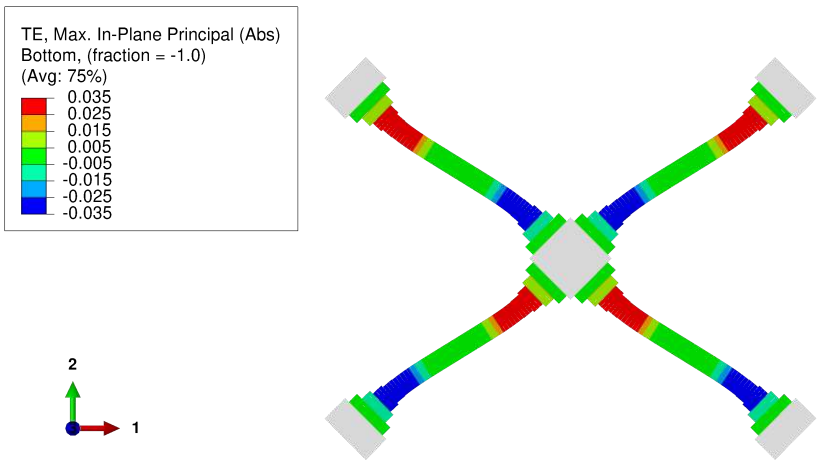

Figure 4.22: Uniaxial tension - Maximum in-plane principal transformation strain contour of the bASM model for the *slender* unit cell with a deformation scale factor of 1. The contour is evaluated at $\varepsilon_{11} = 0.1$. The upper and lower limit of the legend indicate full transformation.

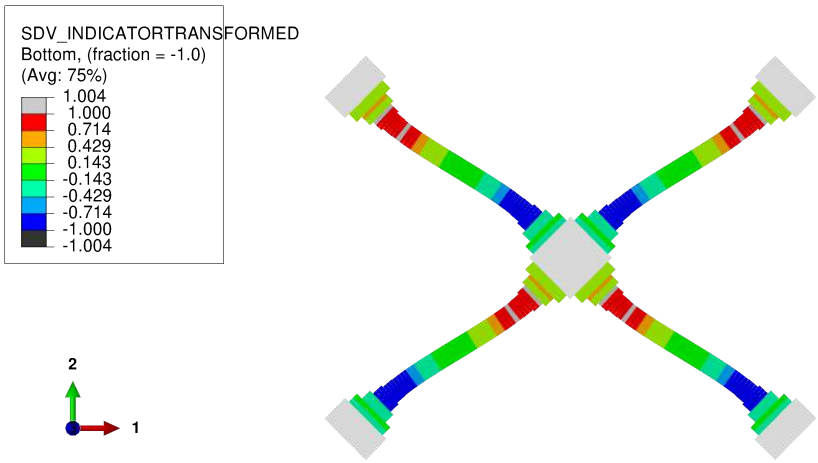

Figure 4.23: Uniaxial tension - Maximum in-plane principal transformation strain contour of the UHYP-POLY model for the *slender* unit cell with a deformation scale factor of 1. The contour is evaluated at $\varepsilon_{11} = 0.1$. The upper (red) and lower (blue) limit of the legend indicate full transformation.

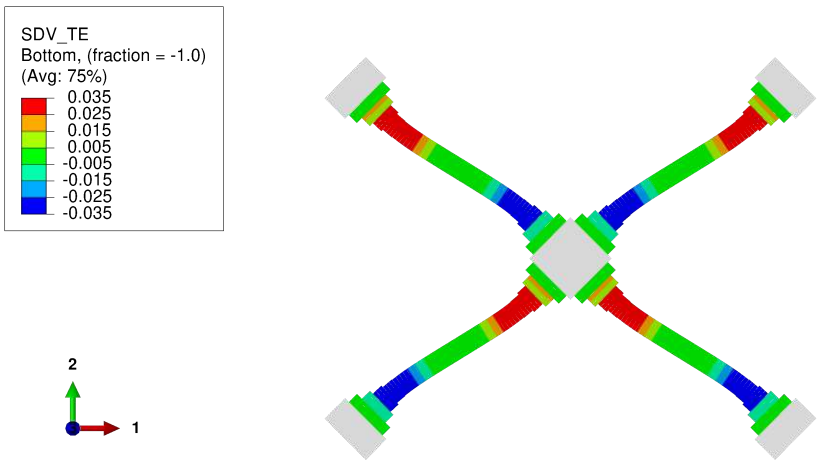

Figure 4.24: Uniaxial tension - Maximum in-plane principal transformation strain contour of the UHYP-MLIN model for the *slender* unit cell with a deformation scale factor of 1. The contour is evaluated at $\varepsilon_{11} = 0.1$. The upper and lower limit of the legend indicate full transformation.

4.5 Verification Step 5

After the verification for the uniaxial tension load case, the three material models are investigated for the pure shear load case of the *slender* unit cell.

4.5.1 Investigation of the Stress-strain Relation

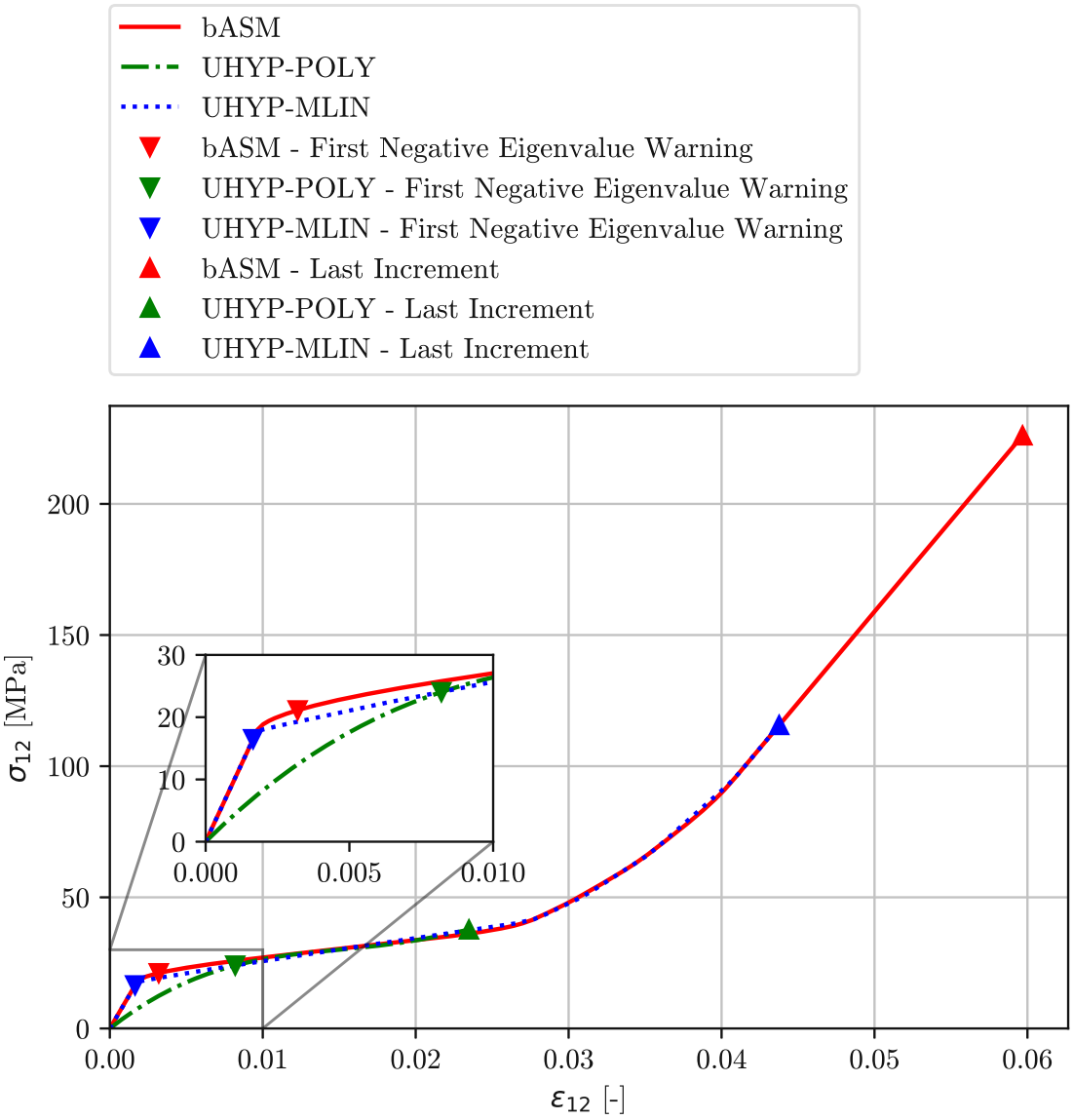

Figure 4.25: Stress-Strain curves of the three models, bASM, UHYP-POLY, and UHYP-MLIN for the pure shear load case of the *slender* unit cell. The markers indicate the first encountered negative eigenvalue warnings for each individual material model and the last computed increment of each analysis.

The results obtained in Figure 4.25 show that the low-loading regime is once again characterized by the same behavior as previously observed, i.e. the UHYP-POLY model differs from the other two by its nonlinear behavior.
Already in the early stages of the loading process, issues arise, with the UHYP-MLIN model being the first for which *ABAQUS* reports negative eigenvalue warnings at $\varepsilon_{12} = 0.00165$, followed by the bASM model at $\varepsilon_{12} = 0.0032$, and last the UHYP-POLY model at $\varepsilon_{12} = 0.0082$. Thus, for each material model, the first negative eigenvalue warning is reported that early in the loading process such that no full local transformation is present before the bifurcation point is reached. Regarding the completion of the analyses, none of the models reach the maximum strain value of $\varepsilon_{12} = 0.1$, but abort beforehand with the UHYP-POLY model being the first.
In Figure 4.26 to 4.28 the transformation strain state at the last computed increment of each analysis is shown. Here, the compressive strains spanning across the two struts from Node NW via Node SE indicate that the phenomenon of buckling is most likely the cause for the encountered warning messages.

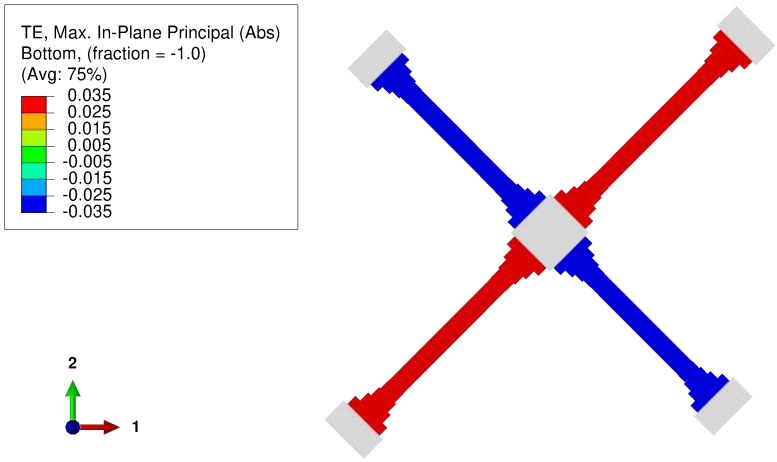

Figure 4.26: Pure shear - Maximum in-plane principal transformation strain contour of the bASM model for the *slender* unit cell with a deformation scale factor of 1. The contour is evaluated at the strain state of the last computed increment, $\varepsilon_{12} = 0.0598$. The upper and lower limit of the legend indicate full transformation.

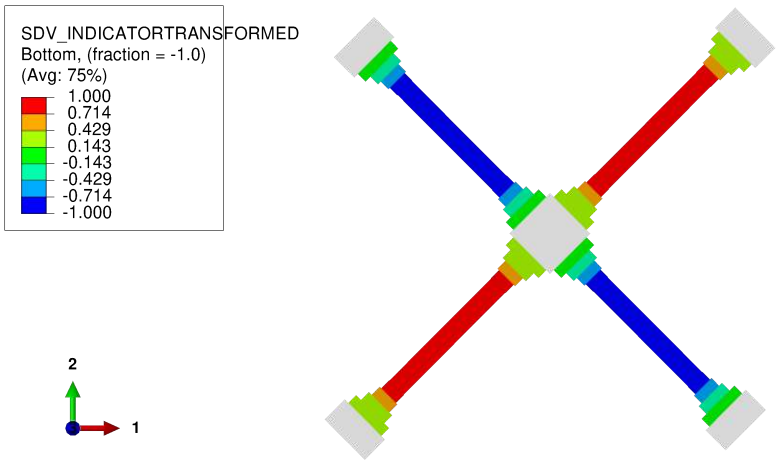

Figure 4.27: Pure shear - Maximum in-plane principal transformation strain contour of the UHYP-POLY model for the *slender* unit cell with a deformation scale factor of 1. The contour is evaluated at the strain state of the last computed increment, $\varepsilon_{12} = 0.0235$. The upper and lower limit of the legend indicate full transformation.

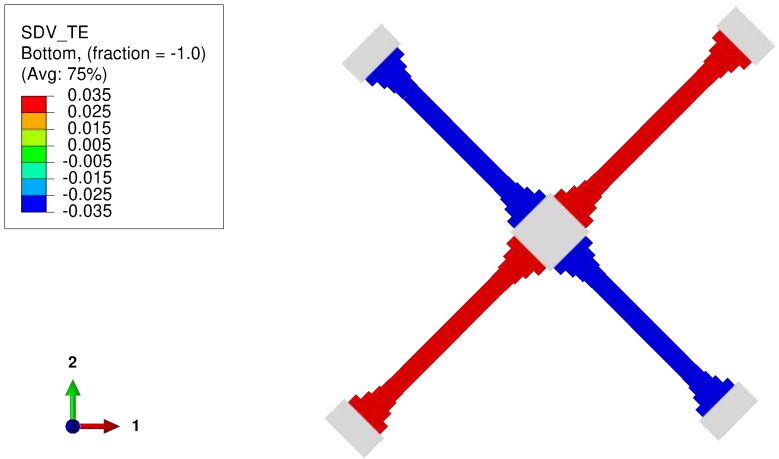

Figure 4.28: Pure shear - Maximum in-plane principal transformation strain contour of the UHYP-MLIN model for the *slender* unit cell with a deformation scale factor of 1. The contour is evaluated at the strain state of the last computed increment, $\varepsilon_{12} = 0.0438$. The upper and lower limit of the legend indicate full transformation.

4.5.2 Buckling Analysis

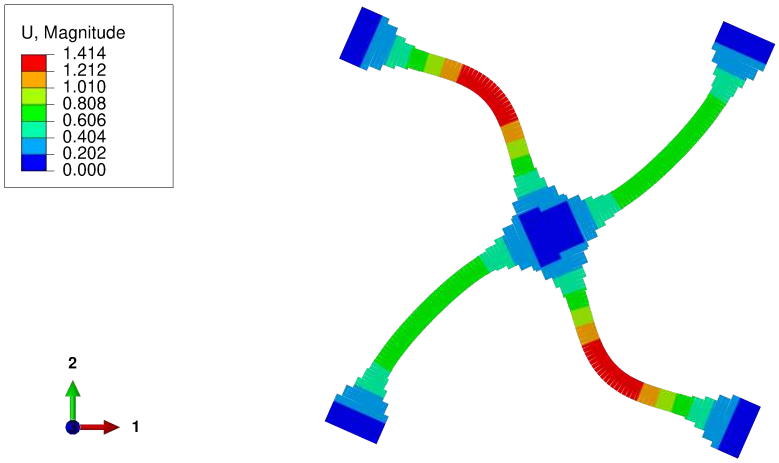

Figure 4.29: First Eigenform corresponding to the bASM model of the *slender* unit cell for the load case of pure shear.

In order to avoid the convergence issues and thus gain information on the behavior of the material models for this combination of unit cell geometry and load case, an imperfection affine to the first eigenform of the structure must be introduced.
This calls for the determination of the first eigenform, which is achieved through a buckling analysis performed on the bASM model of the *slender* unit cell. It should be noted that for this analysis, no preload is applied.
Its shape, shown in Figure 4.29, reveals that the application of the intended perturbation moment in the center of the unit cell is an appropriate choice for an imperfection.
Note that the buckling analysis is not performed for the `UHYPEL`-based material models, as equivalent results are expected there.

4.5.3 Sensitivity Analysis using the Post-load Amplitude

The sensitivity analyses which assess the effect of the imperfection on the response of the structure are presented in this section. Two sets of sensitivity analyses are performed for each material model. For the first set, the post-load amplitude is used, while for the second set, the pre-load amplitude is used. The sensitivity analysis starts with a perturbation moment of 20 Nmm. Then consequent analyses are performed, for which each time the perturbation moment is reduced by 5 Nmm until convergence issues arise again.

The results obtained for the bASM model show in Table 4.1, that a trouble-free reduction of the perturbation moment down to 10 Nmm is possible. At 5 Nmm convergence issues arise again and the analysis aborts. The influence of the imperfection

on the stress-strain curve of the structure is shown in Figure 4.30. The detailed view in Figure 4.31 reveals that the higher the perturbation moment, the further the curve diverts from the trivial solution path. As expected, the imperfection ensures that the bifurcation point, indicated as a black dot, is never reached.

The UHYP-POLY model performs in a comparable manner and shows successful analysis runs up to the perturbation moment of 5 Nmm, see Table 4.2. Figure 4.32 and 4.33 show the respective stress-strain curves. Once again, the effect of the perturbation moment is clearly visible, as the curves deviate from the trivial solution path before the bifurcation point is reached.

The UHYP-MLIN model performs considerably worse in contrast to the other two models, see Table 4.3. Already at 15 Nmm the analysis aborts, and even though it converges again at 10 Nmm negative eigenvalue warnings are reported, suggesting the existence of another instability. The stress-strain curve is given in Figure 4.34 and confirms that the overall response is close to that of the bASM model. The detailed view on the stress-strain relation in the low-loading regime in Figure 4.35 reveals that the UHYP-MLIN model is the only model where bifurcation of equilibrium occurs already in the austenite regime.

Table 4.1: Results of the sensitivity analysis for the bASM model with the post-load amplitude.

Perturbation Moment	Analysis Status	Remarks
20 Nmm	completed successfully	-
15 Nmm	completed successfully	-
10 Nmm	completed successfully	-
5 Nmm	aborted	stopped at the first increment

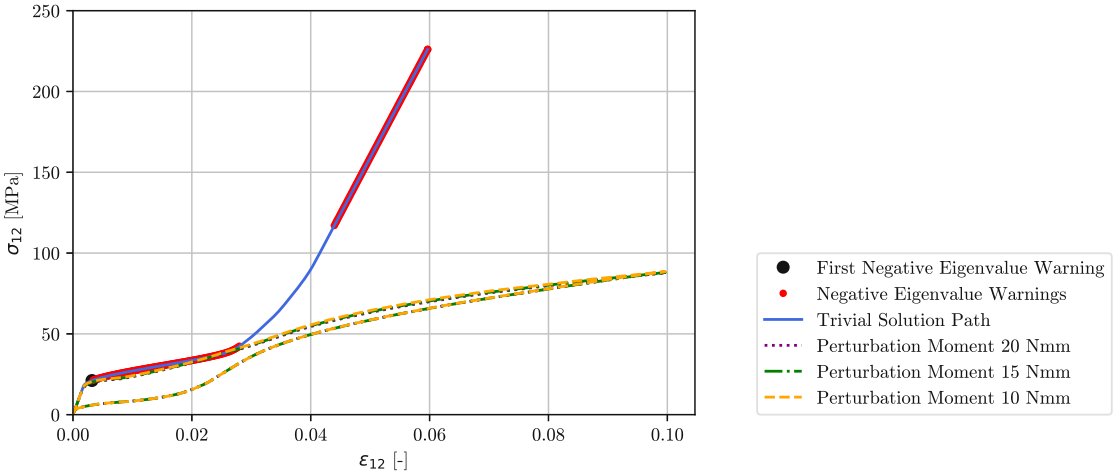

Figure 4.30: Stress-strain curves as a result of the sensitivity analysis of the bASM model with the post-load amplitude loading procedure. The black dot represents the strain state of the unperturbed model at the first negative eigenvalue warning and thus, the bifurcation point.

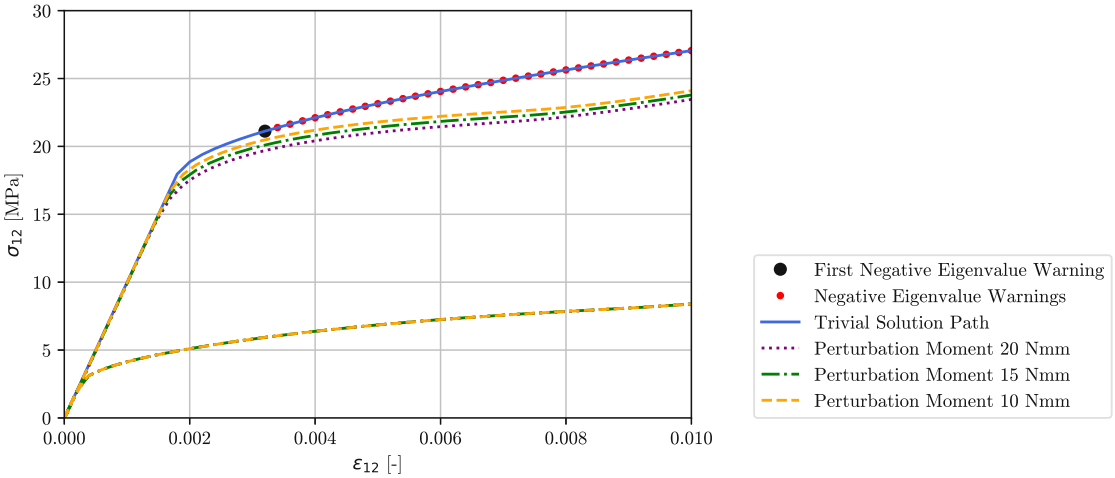

Figure 4.31: Detailed view of the stress-strain curves as a result of the sensitivity analysis of the bASM model with the post-load amplitude loading procedure.

Table 4.2: Results of the sensitivity analysis for the UHYP-POLY model with the post-load amplitude.

Perturbation Moment	Analysis Status	Remarks
20 Nmm	completed successfully	
15 Nmm	completed successfully	-
10 Nmm	completed successfully	-
5 Nmm	aborted	stopped at the first increment

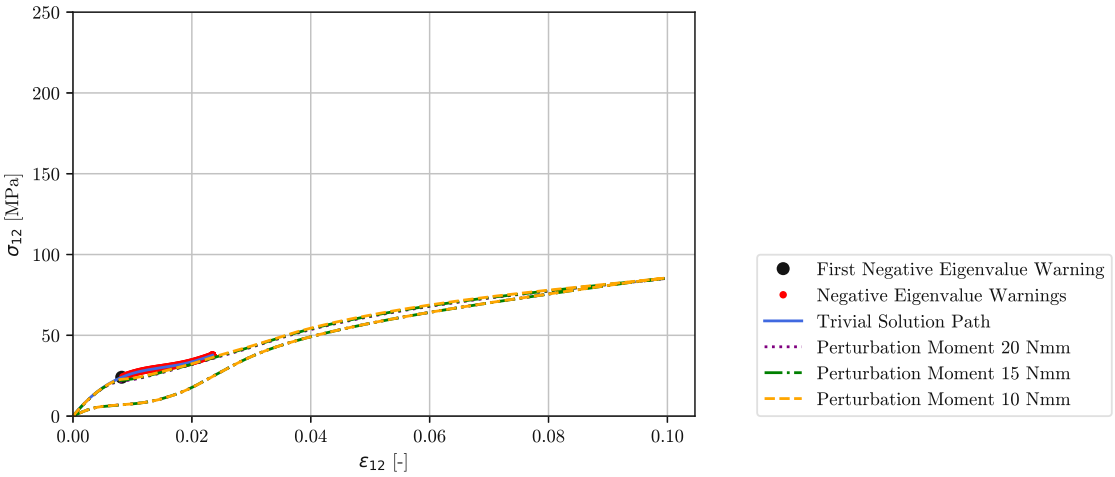

Figure 4.32: Stress-strain curves as a result of the sensitivity analysis of the UHYP-POLY model with the post-load amplitude loading procedure. The black dot represents the strain state of the unperturbed model at the first negative eigenvalue warning and thus, the bifurcation point.

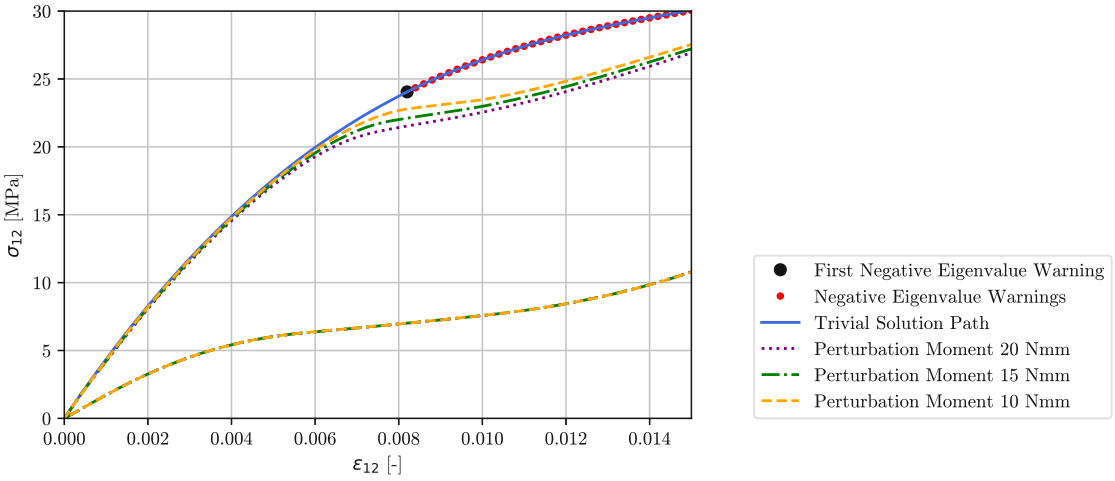

Figure 4.33: Detailed view of the stress-strain curves as a result of the sensitivity analysis of the UHYP-POLY model with the post-load amplitude loading procedure.

Table 4.3: Results of the sensitivity analysis for the UHYP-MLIN model with the post-load amplitude.

Perturbation Moment	Analysis Status	Remarks
20 Nmm	completed successfully	-
15 Nmm	aborted	first negative eigenvalue warning at $\varepsilon_{12} = 0.1$
10 Nmm	completed successfully	first negative eigenvalue warning at $\varepsilon_{12} = 0.0611$ in loading
5 Nmm	aborted	stopped at the first increment

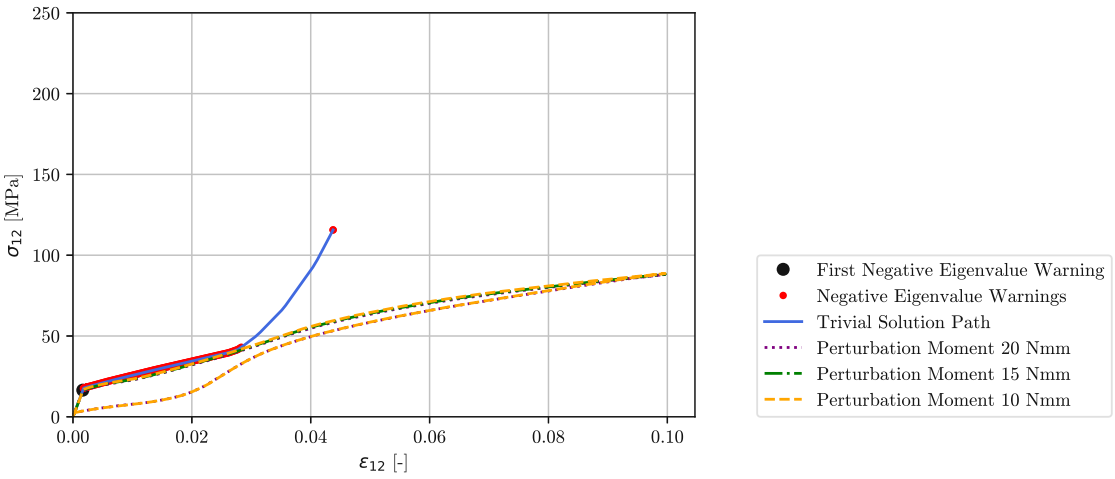

Figure 4.34: Stress-strain curves as a result of the sensitivity analysis of the UHYP-MLIN model with the post-load amplitude loading procedure. The black dot represents the strain state of the unperturbed model at the first negative eigenvalue warning and thus, the bifurcation point.

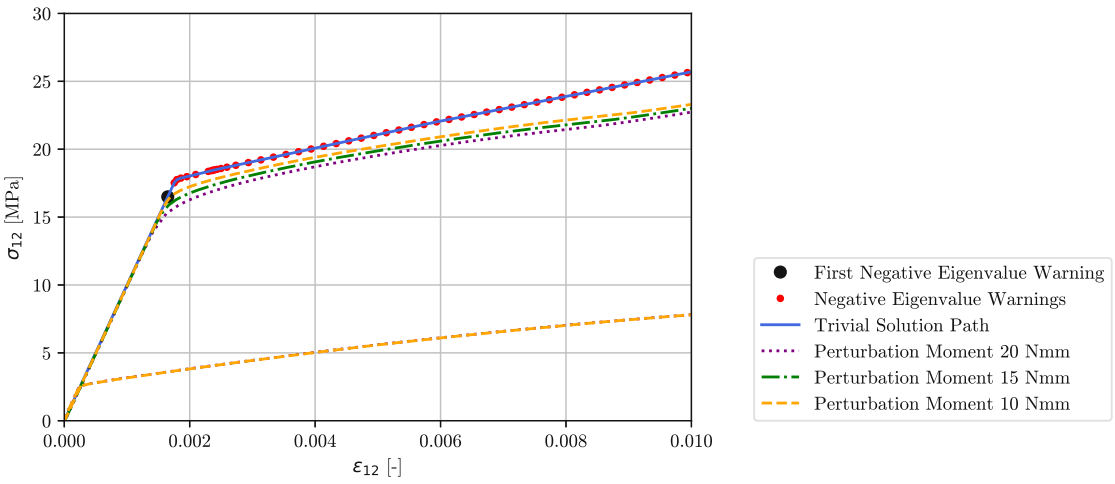

Figure 4.35: Detailed view of the stress-strain curves as a result of the sensitivity analysis of the UHYP-MLIN model with the post-load amplitude loading procedure.

4.5.4 Sensitivity Analysis using the Pre-load Amplitude

The results of the sensitivity analysis for the pre-load amplitude loading procedure are given condensed in Table 4.4. In the case of further interest, the figures displaying the results of each analysis can be found in the Appendix.
The evaluation of the results in Table 4.4 shows that the application of the pre-load amplitude performs considerably worse compared to the post-load amplitude for the `UHYPEL`-based material models. Significantly, for the UHYP-MLIN model, no analysis completed successfully.

Table 4.4: Results of the sensitivity analysis with the pre-load amplitude.

Perturbation Moment	Analysis Status	Remarks
bASM		
20 Nmm	completed successfully	-
15 Nmm	completed successfully	-
10 Nmm	completed successfully	-
5 Nmm	aborted	stopped at the first increment
UHYP-POLY		
20 Nmm	completed successfully	first negative eigenvalue warning at $\varepsilon_{12} = 0.1$
15 Nmm	completed successfully	-
10 Nmm	aborted	first negative eigenvalue warning at $\varepsilon_{12} = 0.1$
5 Nmm	aborted	stopped at the first increment
UHYP-MLIN		
20 Nmm	aborted	first negative eigenvalue warning at $\varepsilon_{12} = 0.1$
15 Nmm	aborted	first negative eigenvalue warning at $\varepsilon_{12} = 0.1$
10 Nmm	aborted	first negative eigenvalue warning at $\varepsilon_{12} = 0.0611$ in loading
5 Nmm	aborted	stopped at the first increment

The results of the two sets of sensitivity analyses show that the post-load amplitude loading procedure is considerably more stable. Especially, in the case of the pre-load amplitude loading procedure, many issues are reported at the load reversal point.
Of the three material models, the UHYP-MLIN model encounters the most issues with only completing the analysis successfully in two cases of which only one did not display any warnings. The UHYP-POLY model shows good stability for the post-load amplitude but struggles with the pre-load amplitude. The bASM model is the most reliable and shows consistent results down to a perturbation moment of 10Nmm for both post-load and pre-load amplitude.

4.5.5 Investigation with Perturbation Moment and Post-load Amplitude

As the introduced imperfection has provided access to the post-buckling regime, a closer look is taken on the pure shear load case with the post-load amplitude and a perturbation moment of 10 Nmm. This combination of imperfection and load amplitude is specifically chosen as the sensitivity analysis has shown that this is the only case with the lowest possible imperfection for which each model has not displayed any warning messages.
Analogous to the the previous cases, the three material models are once again compared with the aim of progressing in the verification of the `UHYPEL` models.

4.5.6 Investigation of the Stress-strain Relation

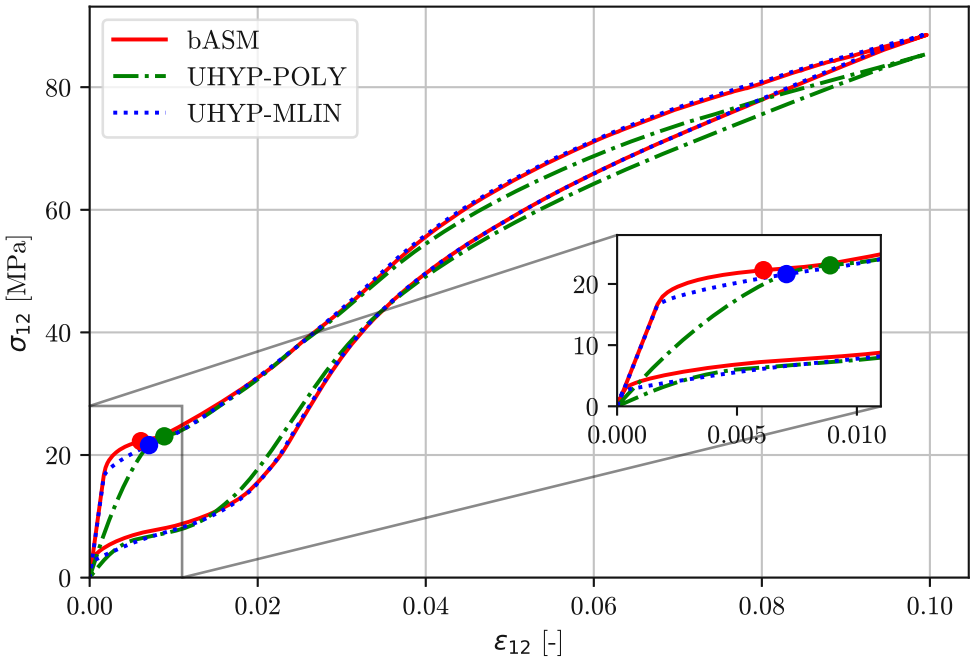

Figure 4.36: Stress-Strain curves of the three models, bASM, UHYP-POLY, and UHYP-MLIN for the pure shear load case of the *slender* unit cell. An imperfection in the form of a perturbation moment of 10 Nmm is applied to the center of the unit cell. The loading procedure for the perturbation moment is the post-load amplitude. The three point markers indicate the state of first full local transformation for each individual material model.

Figure 4.36 shows the stress-strain curve of the three material models, bASM, UHYP-POLY, and UHYP-MLIN. For the load case of pure shear, the three material models agree reasonably well. Again, as previously observed for the cases of uniaxial tension, the UHYP-POLY model shows nonlinear behavior in the low-loading regime. The nonlinearities are once again likely linked to the behavior of the parent material.

4.5.7 Evaluation of the Transformation Zone

Figure 4.37 to Figure 4.42 show the contour plots at the two distinct strain states, i.e. at the state of first full local transformation and at maximum strains.
The initial emergence of the transformation zone is identical throughout all three material models. The three contours in Figures 4.37 to 4.39 show the overlap of the bending moment and compressive stresses governing in the struts connecting NW and SE.
At maximum strains, the contours of the bASM and UHYP-POLY model look close to identical, see Figure 4.40 and 4.41. This is in stark contrast to the UHYP-MLIN

model where the maximum transformation strains are magnitudes higher in the regions in which maximum bending occurs, see Figure 4.42. The cause of these excessive strains might lie in the following: (1) the number of section points is too high, which amplifies numerical artifacts; (2) the Simpson integration, which is used in *ABAQUS* for the numerical integration through the thickness of the beam, is unfit in dealing with piecewise-linear constitutive material models.
Thus, the evaluation of the contour plots suggests analogous evolution of the transformation zone for both the bASM and the UHYP-POLY model. In the case of the UHYP-MLIN model, a clear assessment on how the transformation zone evolves is difficult to make due to the highly elevated strains.

4.5.8 Remarks

While the UHYP-POLY model has proven to be capable of handling the pure shear load case for the *slender* unit cell reasonably well, this does not hold true for the UHYP-MLIN model. The UHYP-MLIN model is the least robust even with the perturbation moment introduced, and in the cases in which the analysis completes, the irregularities regarding the transformation strains are observed. Thus, this effectively marks the first instance where the UHYP-MLIN model has failed to convincingly pass the verification.

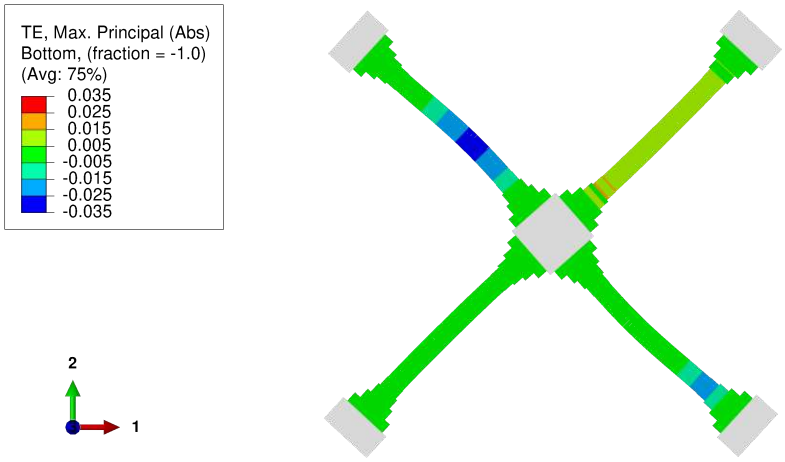

Figure 4.37: Pure shear - Maximum in-plane principal transformation strain contour of the bASM model for the *slender* unit cell with a perturbation moment of 10 Nmm and the post-load amplitude loading process. The contour is evaluated at $\varepsilon_{12} = 0.00611$. The upper and lower limit of the legend indicate full transformation.

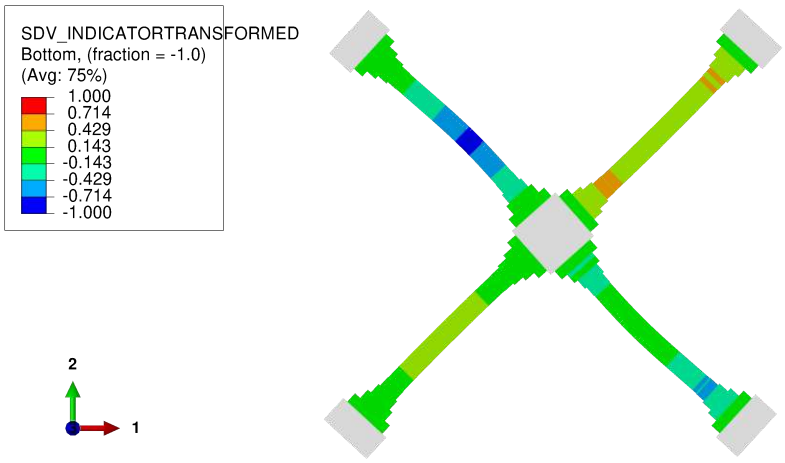

Figure 4.38: Pure shear - Maximum in-plane principal transformation strain contour of the UHYP-POLY model for the *slender* unit cell with a perturbation moment of 10 Nmm and the post-load amplitude loading process. The contour is evaluated at $\varepsilon_{12} = 0.00889$. The upper and lower limit of the legend indicate full transformation.

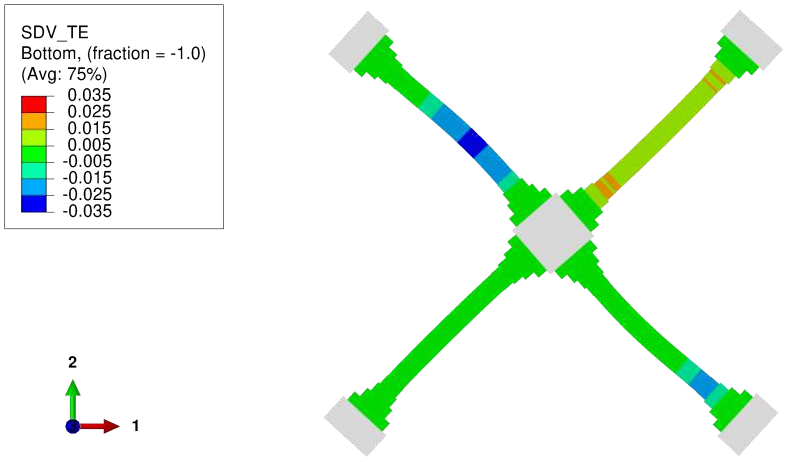

Figure 4.39: Pure shear - Maximum in-plane principal transformation strain contour of the UHYP-MLIN model for the *slender* unit cell with a perturbation moment of 10 Nmm and the post-load amplitude loading process. The contour is evaluated at $\varepsilon_{12} = 0.00706$. The upper and lower limit of the legend indicate full transformation.

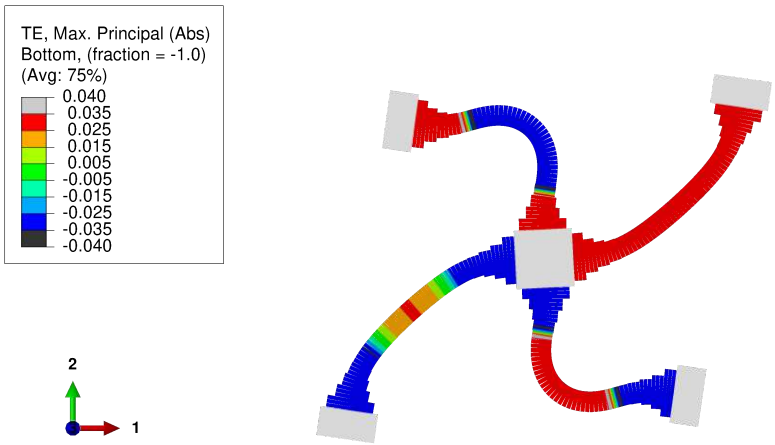

Figure 4.40: Pure shear - Maximum in-plane principal transformation strain contour of the bASM model for the *slender* unit cell with a perturbation moment of 10 Nmm and the post-load amplitude loading process. The defomration scale factor is 1. The contour is evaluated at $\varepsilon_{12} = 0.1$. The upper (red) and lower (blue) limit of the legend indicate full transformation.

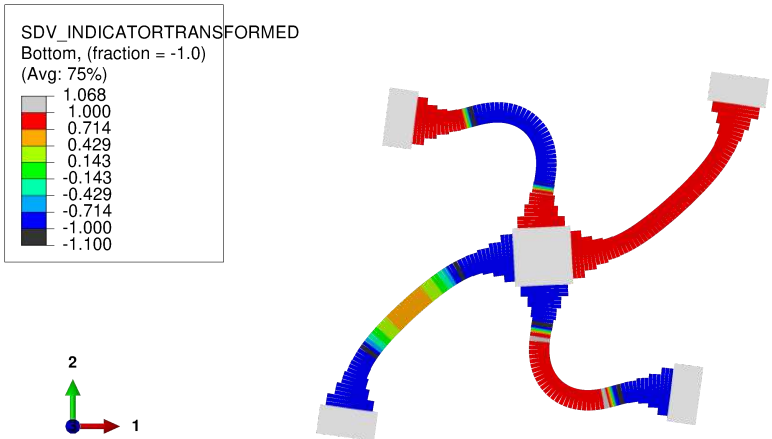

Figure 4.41: Pure shear - Maximum in-plane principal transformation strain contour of the UHYP-POLY model for the *slender* unit cell with a perturbation moment of 10 Nmm and the post-load amplitude loading process. The deformation scale factor is 1. The contour is evaluated at $\varepsilon_{12} = 0.1$. The upper (red) and lower (blue) limit of the legend indicate full transformation.

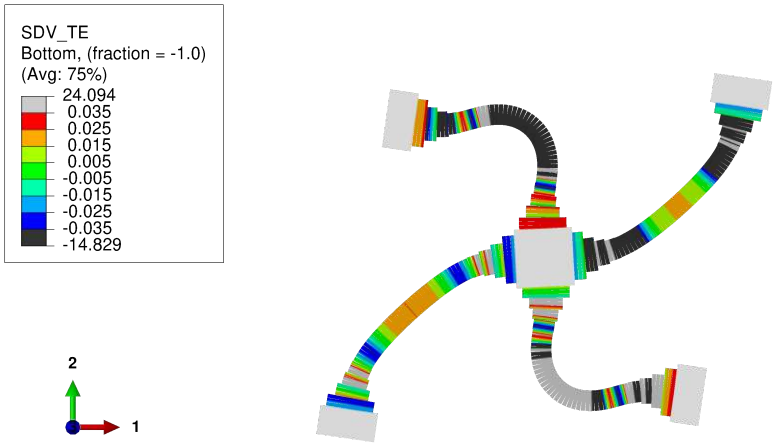

Figure 4.42: Pure shear - Maximum in-plane principal transformation strain contour of the UHYP-MLIN model for the *slender* unit cell with a perturbation moment of 10 Nmm and the post-load amplitude loading process. The deformation scale factor is 1. The contour is evaluated at $\varepsilon_{12} = 0.1$. The upper (red) and lower (blue) limit of the legend indicate full transformation.

4.6 Verification Step 6

To finalise the verification of the UHYPEL-based material model the last variant of unit cell, i.e. the *slender compliant* unit cell, is investigated for the load case of uniaxial tension. More specifically, the results of the UHYPEL-based models are once again compared to those of the bASM model.

4.6.1 Investigation of the Stress-strain Relation

The stress-strain relationship of each material model is shown in Figure 4.43. Consistent to the previous unit cell variants, the low-loading regime is characterized by the alignment of the bASM and UHYP-MLIN model, and the nonlinear behavior of the UHYP-POLY model. Regarding the behavior in the transformation regime, the three material models show approximately the same stiffness, whereas the curve of the UHYP-POLY model is shifted to lower stress levels. Owing to the increased rotational compliance introduced by the rotation of the center, the stresses at maximum applied strains are lower, and thus the fully transformed martensite phase is not reached for this loading scenario. The unloading regime shows consistent behavior to the previous models, with the retransformation starting first for the bASM model.

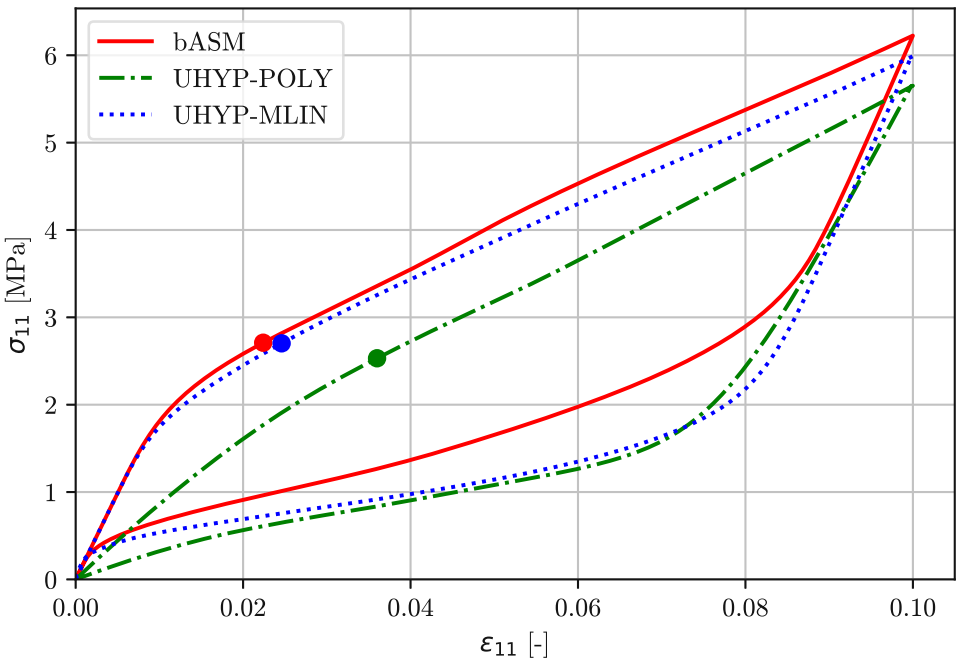

Figure 4.43: Stress-Strain curves of the three models, bASM, UHYP-POLY, and UHYP-MLIN for the uniaxial tension load case of the *slender compliant* unit cell. The three point markers indicate the state of first full local transformation for each individual material model.

4.6.2 Evaluation of the Transformation Zone

The contour plots in Figure 4.44 to 4.46 show that the transformation zone initiates in the same region for each material model. Furthermore, at maximum applied loads, the contours in Figure 4.47 to 4.49, display analogous strain distribution, suggesting that the development of the transformation zone is the same for the three models. However, different to the *slender* unit cell, here, the transformation zone no longer evolves with symmetric character but initiates at the center of the cell and spreads from there outwards to the center of the struts which connect node SW and NE.

4.6.3 Remarks

The evaluation of the results show that also for this variant of the unit cell, the `UHYPEL` models capture the response of the unit cell with adequate precision. Furthermore, the differences encountered are in line with the previously recorded results.

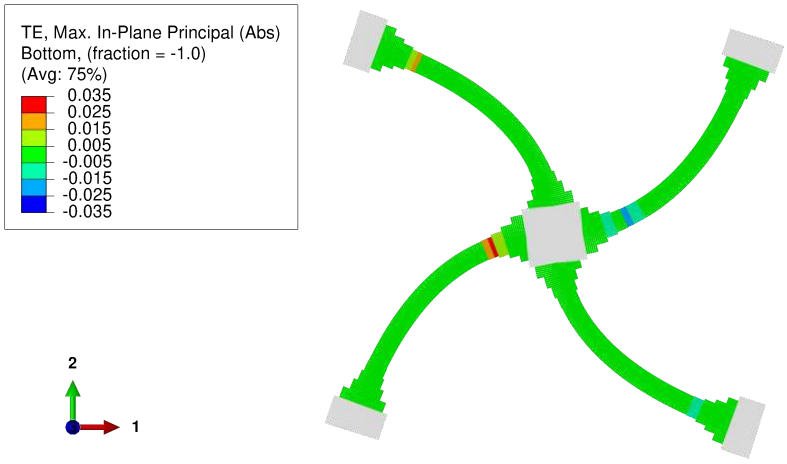

Figure 4.44: Uniaxial tension - Maximum in-plane principal transformation strain contour of the bASM model for the *slender compliant* unit cell with a deformation scale factor of 1. The contour is evaluated at $\varepsilon_{11} = 0.0224$. The upper and lower limit of the legend indicate full transformation.

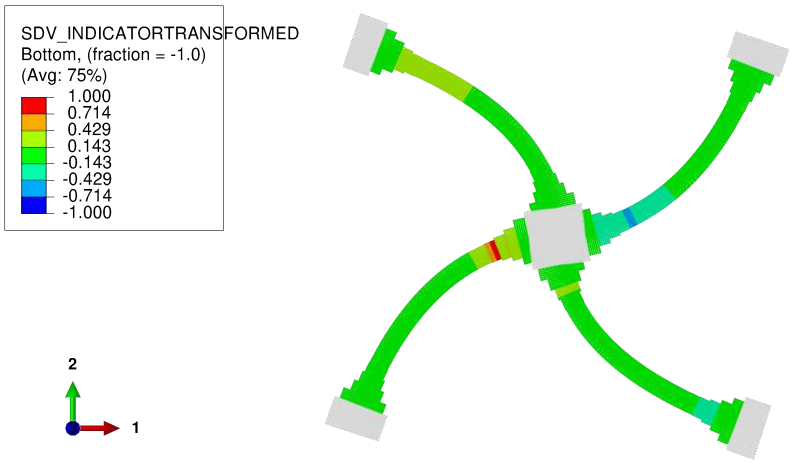

Figure 4.45: Uniaxial tension - Maximum in-plane principal transformation strain contour of the UHYP-POLY model for the *slender compliant* unit cell. The contour is evaluated at $\varepsilon_{11} = 0.036$. The upper and lower limit of the legend indicate full transformation.

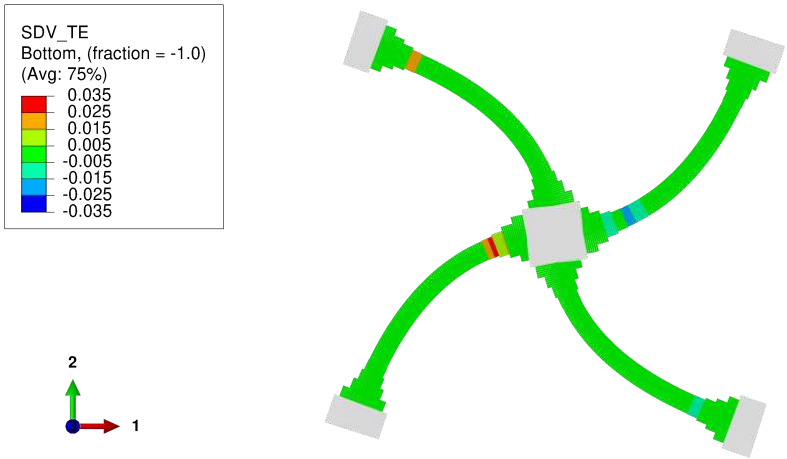

Figure 4.46: Uniaxial tension - Maximum in-plane principal transformation strain contour of the UHYP-MLIN model for the *slender compliant* unit cell with a deformation scale factor of 1. The contour is evaluated at $\varepsilon_{11} = 0.0246$. The upper and lower limit of the legend indicate full transformation.

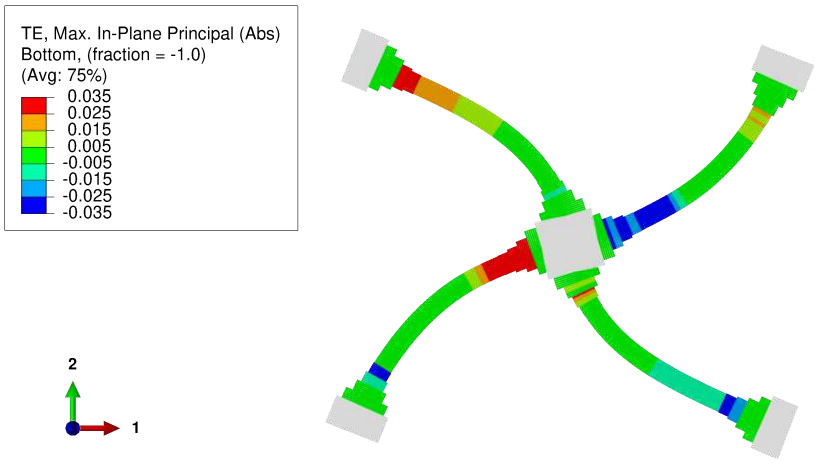

Figure 4.47: Uniaxial tension - Maximum in-plane principal transformation strain contour of the bASM model for the *slender compliant* unit cell with a deformation scale factor of 1. The contour is evaluated at $\varepsilon_{11} = 0.1$. The upper and lower limit of the legend indicate full transformation.

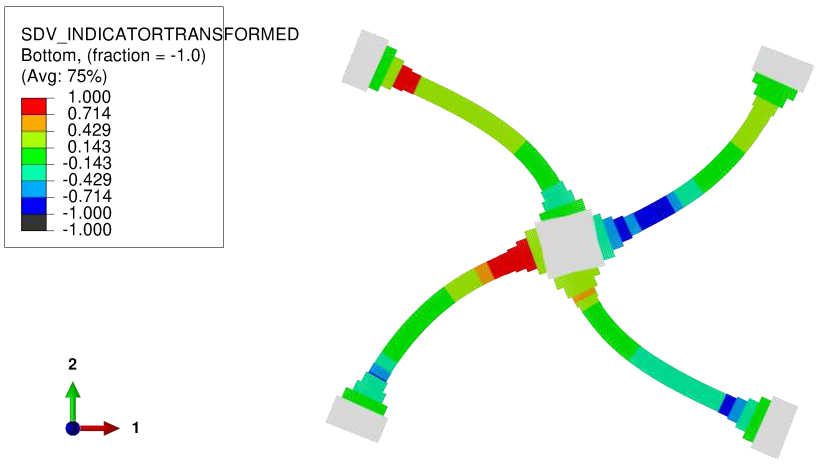

Figure 4.48: Uniaxial tension - Maximum in-plane principal transformation strain contour of the UHYP-POLY model for the *slender compliant* unit cell with a deformation scale factor of 1. The contour is evaluated at $\varepsilon_{11} = 0.1$. The upper (red) and lower (blue) limit of the legend indicate full transformation.

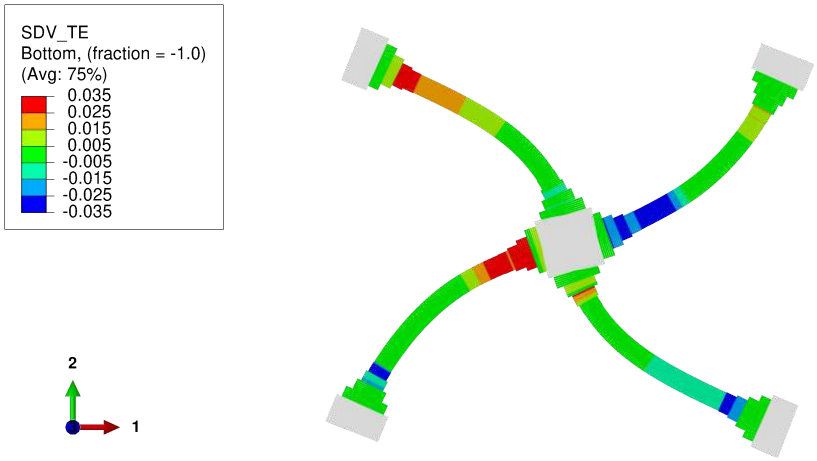

Figure 4.49: Uniaxial tension - Maximum in-plane principal transformation strain contour of the UHYP-MLIN model for the *slender compliant* unit cell with a deformation scale factor of 1. The contour is evaluated at $\varepsilon_{11} = 0.1$. The upper and lower limit of the legend indicate full transformation.

4.7 Verification Step 7

The following section comprises the last step of the verification process for which the *slender compliant* unit cell is subjected to pure shear and investigated for each of the three material models.

4.7.1 Investigation of the Stress-strain Relation

The stress-strain curves in Figure 4.50 reveal that opposed to the *slender* unit cell, the *slender compliant* unit cell does not suffer from any instabilities for the load case of pure shear, and that each analysis has been completed successfully. This comes as expected, since the curvature of the struts connecting NW and SE allows for their deformation without exclusive build-up of compressive strains. Owing to that, buckling does not occur.
The stress-strain curves of the three material models are in good agreement. Regarding their differences, they continue the same trend as seen in the results of the previous load cases, with the UHYP-POLY model being the only model showing nonlinear response in the low-loading regime.

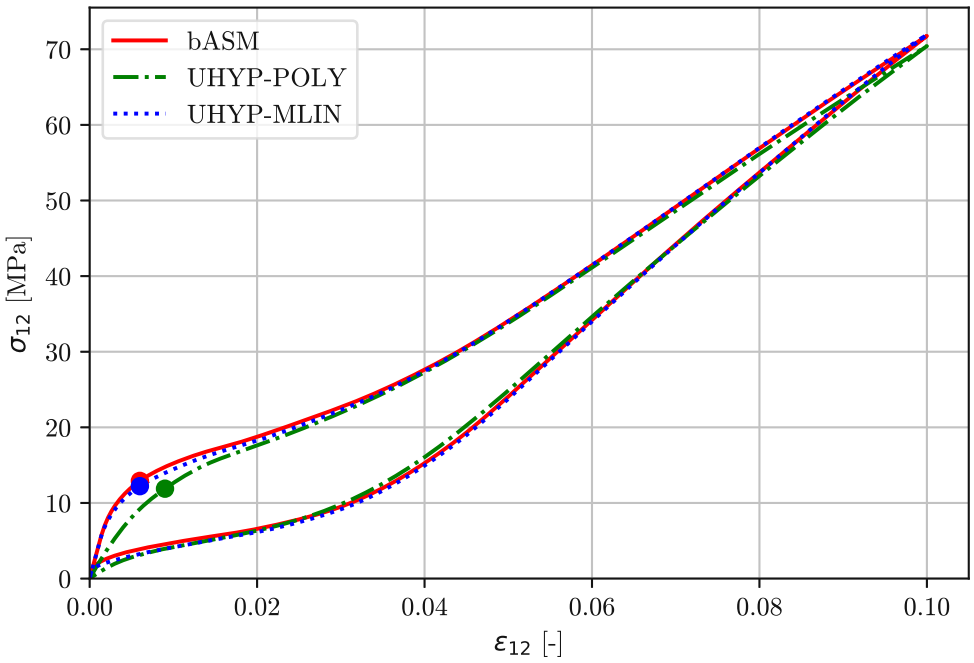

Figure 4.50: Stress-strain curves of the three models, bASM, UHYP-POLY, and UHYP-MLIN for the pure shear load case of the *slender compliant* unit cell with a deformation scale factor of 1. The three point markers indicate the state of first full local transformation for each individual material model.

4.7.2 Evaluation of the Transformation Zone

The contours of Figures 4.51 to 4.53 show that the narrow end of the roundings on strut end, NE and SE, mark for each material model the region of first full local transformation. Under maximum applied load, the contour of the bASM model agrees well with the UHYP-POLY model, see Figures 4.54 and 4.55. However, for the UHYP-MLIN model, Figure 4.56 shows that a similar issue arises as seen for the pure shear load case of the *slender* unit cell with the introduced imperfection. Namely, in the regions of maximum bending, strains of very high magnitude are recorded which are considerably exceeding the expected transformation strain of 0.034. This considerable deviation can be attributed to the same causes mentioned as for the pure shear load case of the *slender* unit cell, i.e the Simpson thickness integration struggles in handling the piecewise-linear constitutive material model.

4.7.3 Remarks

The evaluation of both the stress-strain curves and contour plots reveal that the UHYP-POLY model handles the load case of pure shear for the *slender compliant* unit cell well, and thus passes all steps of the verification process successfully. This, however, cannot be said for the UHYP-MLIN model due to the irregularities regarding the strain values observed in the region of high amounts of bending at maximum applied load.

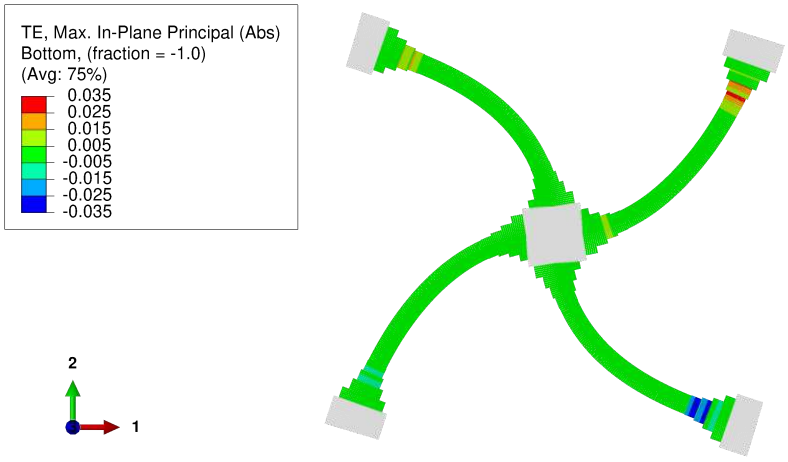

Figure 4.51: Pure shear - Maximum in-plane principal transformation strain contour of the bASM model for the *slender compliant* unit cell with a deformation scale factor of 1. The contour is evaluated at $\varepsilon_{12} = 0.006$. The upper and lower limit of the legend indicate full transformation.

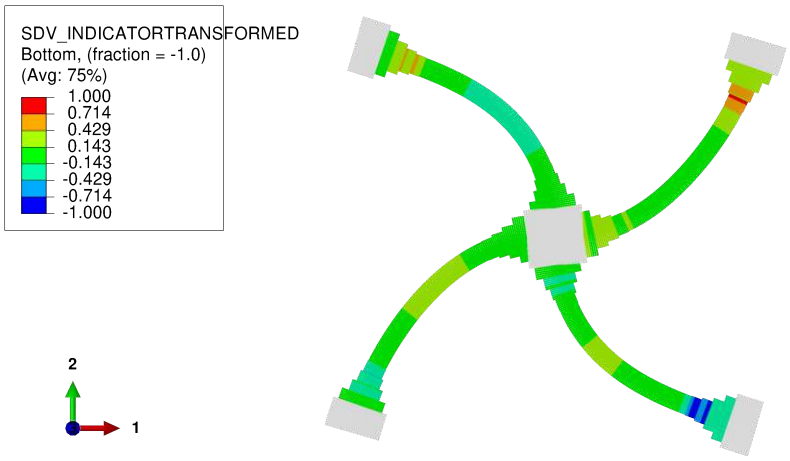

Figure 4.52: Pure shear - Maximum in-plane principal transformation strain contour of the UHYP-POLY model for the *slender compliant* unit cell with a deformation scale factor of 1. The contour is evaluated at $\varepsilon_{12} = 0.009$. The upper and lower limit of the legend indicate full transformation.

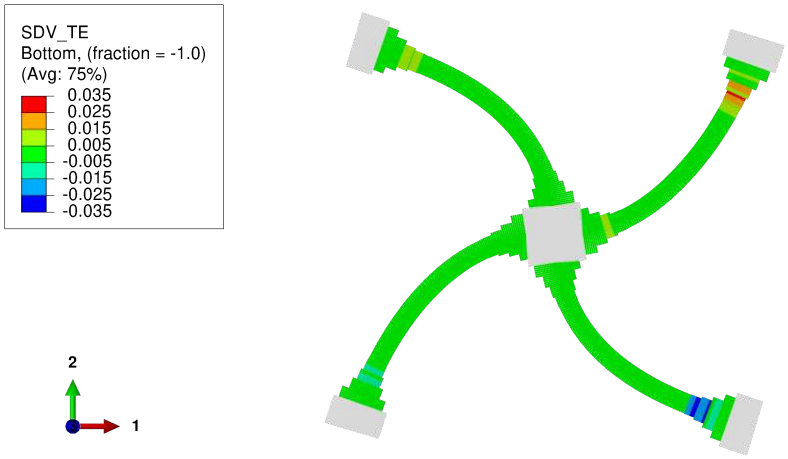

Figure 4.53: Pure shear - Maximum in-plane principal transformation strain contour of the UHYP-MLIN model for the *slender compliant* unit cell with a deformation scale factor of 1. The contour is evaluated at $\varepsilon_{12} = 0.006$. The upper and lower limit of the legend indicate full transformation.

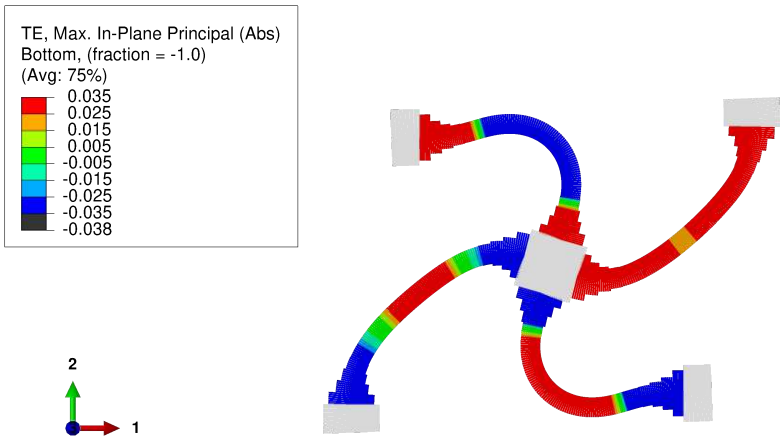

Figure 4.54: Pure shear - Maximum in-plane principal transformation strain contour of the bASM model for the *slender compliant* unit cell with a deformation scale factor of 1. The contour is evaluated at $\varepsilon_{12} = 0.1$. The upper (red) and lower (blue) limit of the legend indicate full transformation.

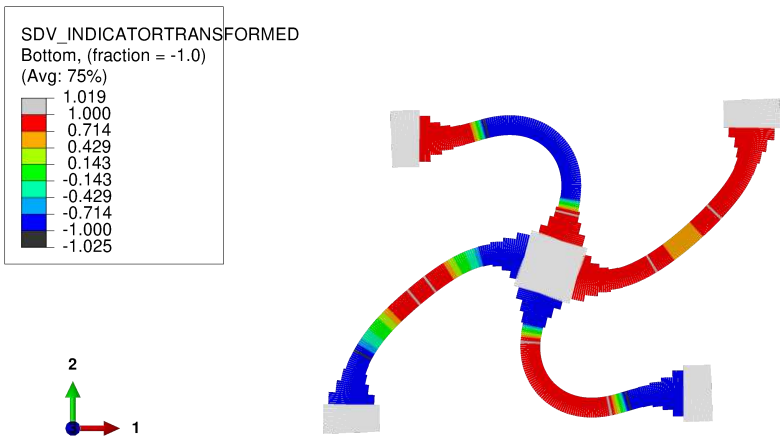

Figure 4.55: Pure shear - Maximum in-plane principal transformation strain contour of the UHYP-POLY model for the *slender compliant* unit cell with a deformation scale factor of 1. The contour is evaluated at $\varepsilon_{12} = 0.1$. The upper (red) and lower (blue) limit of the legend indicate full transformation.

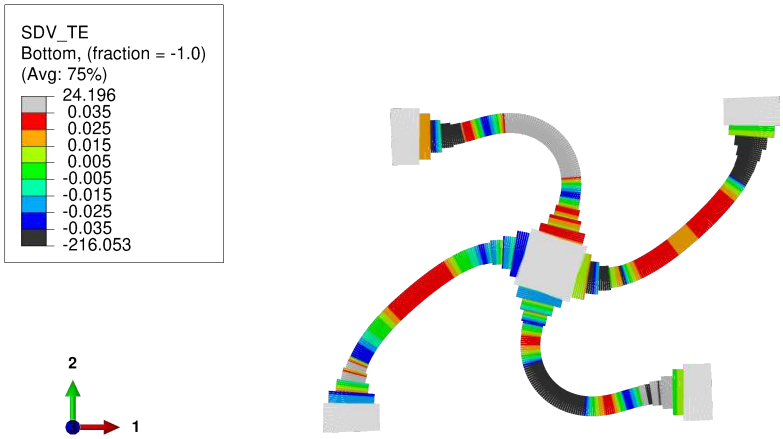

Figure 4.56: Pure shear - Maximum in-plane principal transformation strain contour of the UHYP-MLIN model for the *slender compliant* unit cell with a deformation scale factor of 1. The contour is evaluated at $\varepsilon_{12} = 0.1$. The upper (red) and lower (blue) limit of the legend indicate full transformation.

5 Conclusion

In this thesis, the two uniaxial hypoelastic material models developed by Schasching et al. [7] are investigated with the aim of verification. Based on a proposed framework, numerical simulations are conducted with the aid of the Finite Element Method on continuum and beam models of three different unit cell designs, i.e. the *cross*, *slender*, and *slender compliant* unit cell. Their modeling strategies are presented and the outcome of the comparisons confirm that the strategies are very well applicable for the chosen unit cell designs. Moreover, the comparisons between the continuum and beam models show that the latter, especially in conjunction with the proposed modeling strategies, is capable of reliably predicting the mechanical response of lattice structures of superelastic material.

The numerical results of the simulations show that for the uniaxial load case, the hypoelastic multilinear material model is in good agreement with the results of the material model for superelasticity provided by *ABAQUS*. As for the load case of pure shear, the contour plots depicting the transformation strain distribution show significant deviations at maximum applied loads. Namely, in the region of high bending, excessively high strains are observed that are well above the expected transformation strain values. While multiple factors might be at hand, a possible cause for this could be traced back to the Simpson integration since it is ill-suited for handling piecewise-linear functions and struggles, especially in the regions in which discontinuities are present. Thus, to properly determine the limits of applicability for that material model, further investigation is required. Nevertheless, the UHYP-MLIN model has provided significant supplementary information to better understand the results of the UHYP-POLY model, and thus, has helped in the progress of its verification.

The results of the polyfitted hypoelastic material model are in good agreement with those of the *ABAQUS* material model for superelasticity in each step of the verification process. Thus, its verification can be considered a success.
As already reported by Schasching et al. [7], slight deviations are observed in the

low-loading regime. However, these can be traced back to the implementation of the polyfitted hypoelastic material model and its closer connection to the experimental data of the parent material, an aspect which is of positive nature.

The successful verification of the uniaxial hypoelastic polyfitted material model in this thesis is a direct contribution to the work of Schasching et al. [7] as it extends its field of use for more challenging unit cell designs. The material model provides an efficient tool when faced with simulations of complex materials whose properties are based on experimental data. The calibration is flexible and inherently tied to the data set, which means that the risk of misinterpreting key material parameters is significantly reduced. Since the model is designed for beam elements, it is especially useful in computing large-scale lattices with complex parent material. Thus, it could find use cases in both the fields of structural optimization and additive manufacturing of superelastic material.

Appendix

For the sake of completion, the results of the sensitivity analysis of the *slender* unit cell are given for the pre-load amplitude loading procedure in Figures A.1 to A.6. The key aspects of each stress-strain curve are already contained in Table 4.4 of Section 4.5.4.

The figures first serve a supplementary role. Note that up to the load reversal point, the stress-strain curves are close to analogous to those in which the postload amplitude loading procedure is applied. As already mentioned in Section 4.5.4, Figure A.5 and A.6 show that in the case of the UHYP-MLIN material model, the analysis does not finish for any of the perturbation moments applied. More specifically, each analysis fails at the load reversal point.

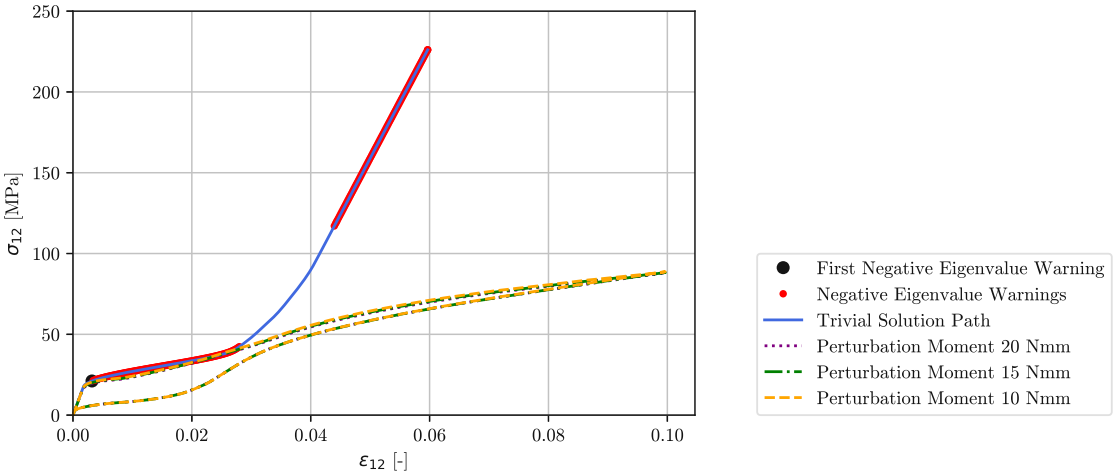

Figure A.1: Stress-strain curves as a result of the sensitivity analysis of the bASM model with the pre-load amplitude loading procedure. The black dot represents the strain state of the unperturbed model at the first negative eigenvalue warning and thus, the bifurcation point.

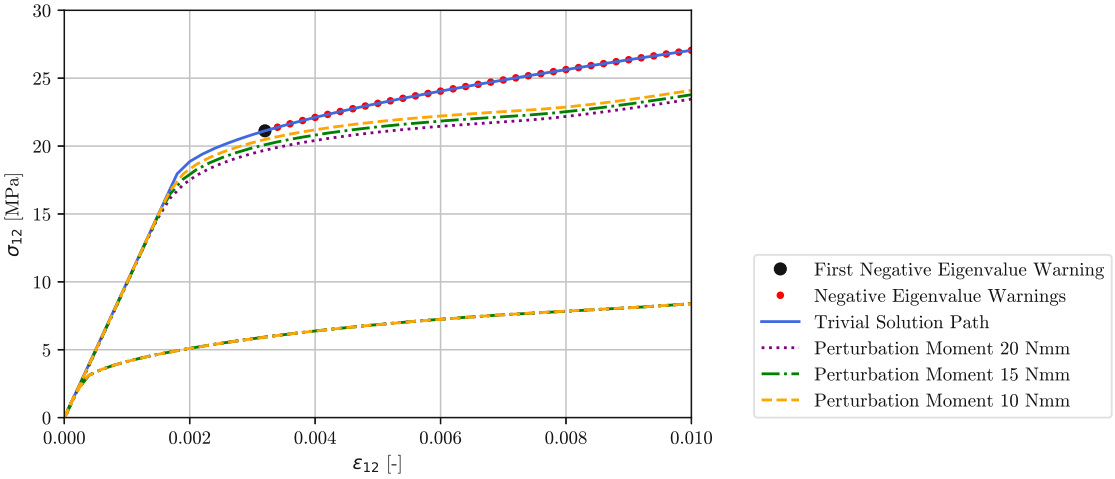

Figure A.2: Detailed view of the stress-strain curves as a result of the sensitivity analysis of the bASM model with the pre-load amplitude loading procedure.

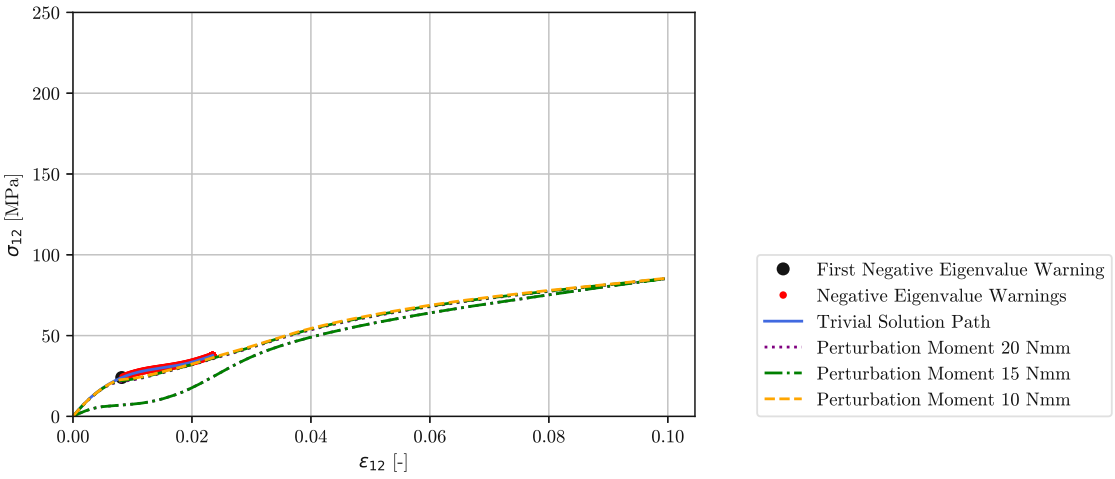

Figure A.3: Stress-strain curves as a result of the sensitivity analysis of the UHYP-POLY with the pre-load amplitude loading procedure. The black dot represents the strain state of the unperturbed model at the first negative eigenvalue warning and thus, the bifurcation point.

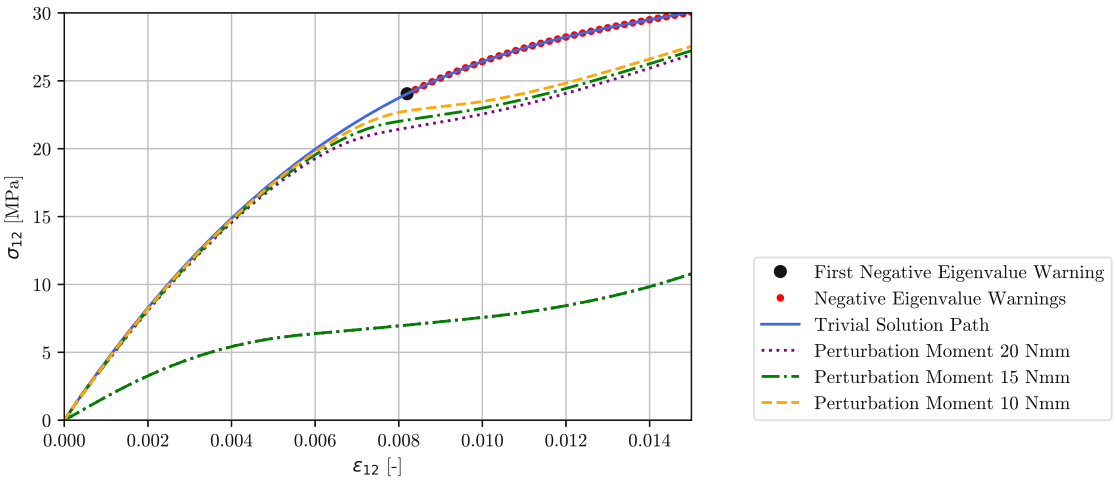

Figure A.4: Detailed view of the stress-strain curves as a result of the sensitivity analysis of the UHYP-POLY model with the pre-load amplitude loading procedure.

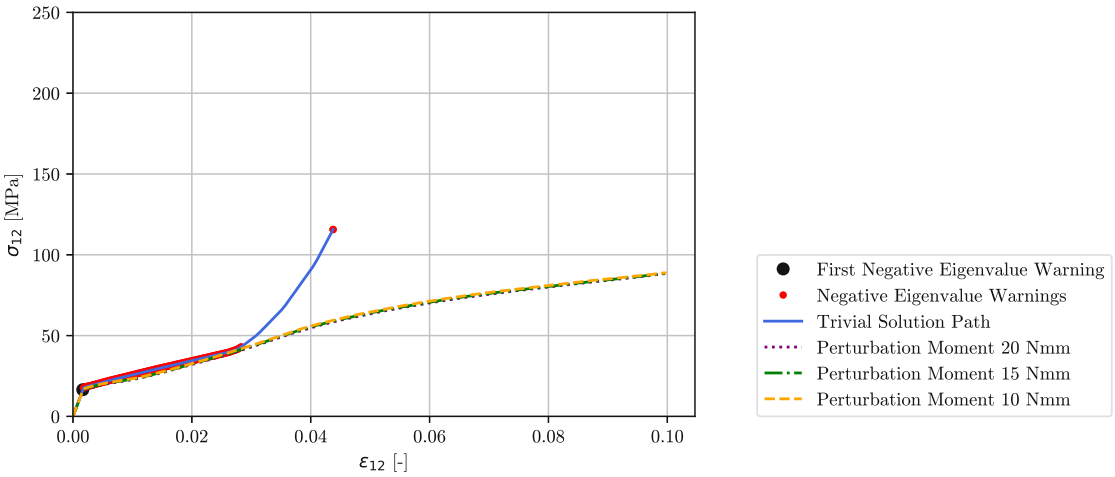

Figure A.5: Stress-strain curves as a result of the sensitivity analysis of the UHYP-MLIN with the pre-load amplitude loading procedure. The black dot represents the strain state of the unperturbed model at the first negative eigenvalue warning and thus, the bifurcation point.

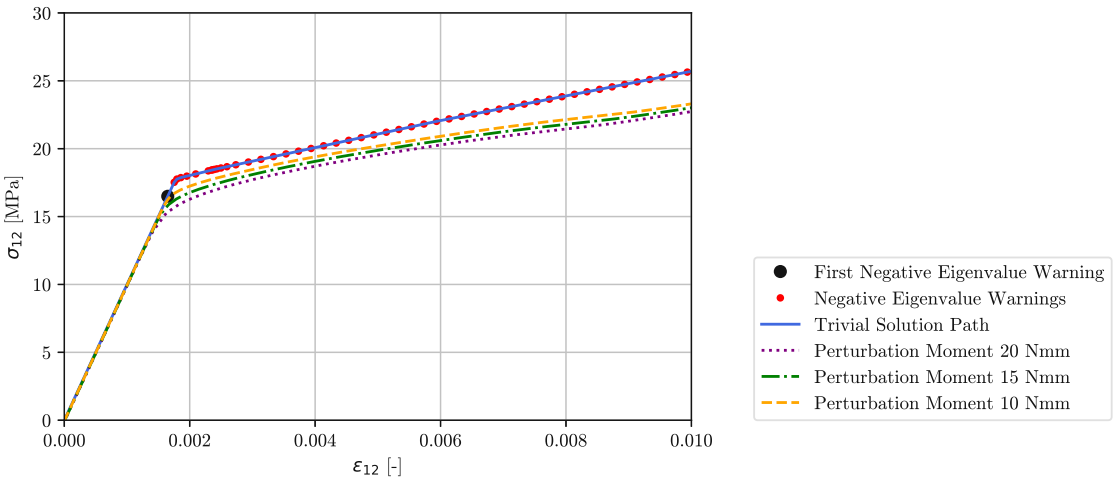

Figure A.6: Detailed view of the stress-strain curves as a result of the sensitivity analysis of the UHYP-MLIN model with the pre-load amplitude loading procedure.

Bibliography

[1] N. A. Fleck, V. S. Deshpande, and M. F. Ashby, "Micro-architectured materials: Past, present and future," *Proceedings of the Royal Society A: Mathematical, Physical and Engineering Sciences*, vol. 466, pp. 2495–2516, 2010.

[2] T. Maconachie, M. Leary, B. Lozanovski, *et al.*, "Slm lattice structures: Properties, performance, applications and challenges," *Materials and Design*, vol. 183, 2019.

[3] K. Bertoldi, P. M. Reis, S. Willshaw, and T. Mullin, "Negative poisson's ratio behavior induced by an elastic instability," *Advanced Materials*, vol. 22, 2010.

[4] S. Catchpole-Smith, R. R. Sélo, A. W. Davis, I. A. Ashcroft, C. J. Tuck, and A. Clare, "Thermal conductivity of tpms lattice structures manufactured via laser powder bed fusion," *Additive Manufacturing*, vol. 30, 2019.

[5] J. Zhang, Y. Shen, Y. Sun, *et al.*, "Design and mechanical testing of porous lattice structure with independent adjustment of pore size and porosity for bone implant," *Journal of Materials Research and Technology*, vol. 18, 2022.

[6] C. Yang and Q. M. Li, "Advanced lattice material with high energy absorption based on topology optimisation," *Mechanics of Materials*, vol. 148, 2020.

[7] M. M. Schasching, O. Červinek, D. Koutný, H. E. Pettermann, and M. Todt, "A uniaxial hysteretic superelastic constitutive model applied to additive manufactured lattices," *PAMM*, vol. 25, 2025.

[8] F. Auricchio and R. L. Taylorb, "Computer methods in applied mechanics and englnserlng shape-memory alloys: Modelling and numerical simulations of the finite-strain superelastic behavior," *Computer Methods Appl. Mech. Engrg*, vol. 143, pp. 175–194, 1997.

[9] F. Auricchio, R. L. Taylor, and J. Lubliner, "Shape-memory alloys: Macromodelling and numerical simulations of the superelastic behavior," *Computer Methods Appl. Mech. Engrg*, vol. 146, pp. 281–312, 1997.

[10] M. Tebianian, S. Aghaie, N. S. R. Jafari, *et al.*, "A review of the metal additive manufacturing processes," *Materials*, vol. 16, 2023.

[11] A. Concilio, *Shape memory alloy engineering : for aerospace, structural and biomedical applications.* 2nd ed. Butterworth-Heinemann, 2021.

[12] K. Tsuchiya, "1 - mechanisms and properties of shape memory effect and superelasticity in alloys and other materials: A practical guide," in *Shape Memory and Superelastic Alloys*. Woodhead Publishing, 2011, pp. 3–14.

[13] L. Petrini and F. Migliavacca, "Biomedical applications of shape memory alloys," *Journal of Metallurgy*, vol. 2011, 2011.

[14] P. H. Mayrhofer, *Ingenieurwerkstoffe, Lecture Notes*. TU Wien: Institut für Werkstoffwissenschaft und Werkstofftechnologie, 2019.

[15] M. Elahinia, N. S. Moghaddam, M. T. Andani, A. Amerinatanzi, B. A. Bimber, and R. F. Hamilton, "Fabrication of niti through additive manufacturing: A review," *Progress in Materials Science*, vol. 83, pp. 630–663, 2016.

[16] K. Safaei, H. Abedi, M. Nematollahi, *et al.*, "Additive manufacturing of niti shape memory alloy for biomedical applications: Review of the lpbf process ecosystem," *JOM*, vol. 73, pp. 3771–3786, 2021.

[17] N. S. Moghaddam, S. Saedi, A. Amerinatanzi, *et al.*, "Achieving superelasticity in additively manufactured niti in compression without post-process heat treatment," *Scientific Reports*, vol. 9, 2019.

[18] H. J. Böhm, *Mechanics of Microstructured Materials*. Springer Wien New York, 2004.

[19] L. Anand and S. Govindjee, "Chapter 3 - kinematics," in *Continuum Mechanics of Solids*. Oxford University Press, 2020, pp. 35–65.

[20] C. Thiel, J. Voss, R. J. Martin, and P. Neff, "Shear, pure and simple," *International Journal of Non-Linear Mechanics*, vol. 112, pp. 57–72, 2019.

[21] A. Luongo, M. Ferretti, and S. D. Nino, "Chapter 2 - phenomenological aspects of bifurcation of structures," in *Stability and Bifurcation of Structures: Statical and Dynamical Systems*. Springer, 2023, pp. 13–33.

[22] M. Todt, *Nonlinear Finite Element Method, Lecture Notes*. TU Wien: Institut für Leichtbau und Struktur-Biomechanik, 2021.

[23] C. Cisse, W. Zaki, and T. B. Zineb, "A review of constitutive models and modeling techniques for shape memory alloys," *International Journal of Plasticity*, vol. 76, pp. 244–284, 2016.

[24] P. Junker and K. Hackl, "Calibration and finite element implementation of an energy-based material model for shape memory alloys," *Shape Memory and Superelasticity*, vol. 2, pp. 247–253, 2016.

[25] L. Xue, K. C. Atli, C. Zhang, *et al.*, "Laser powder bed fusion of defect-free niti shape memory alloy parts with superior tensile superelasticity," *Acta Materialia*, vol. 229, 2022.

[26] *Abaqus simulia user assistance*, Dassault Systèmes Simulia Corp., Providence, RI, USA, 2023.

[27] C. Mittelstedt, "Chapter 2 - plane stress state," in *Engineering Mechanics 2: Strength of Materials: An Introduction with Many Examples*. Springer Berlin Heidelberg, 2023, pp. 23–44.

[28] C. Wang, J. Reddy, and K. Lee, "Chapter 2 - bending of beams," in *Shear Deformable Beams and Plates*, C. Wang, J. Reddy, and K. Lee, Eds. Oxford: Elsevier Science Ltd, 2000, pp. 11–38.

[29] M. M. Schasching, "Micropolar continuum modeling of lattice materials," Ph.D. dissertation, TU Wien, 2023.

[30] M. R. Eslami, "Chapter 1 - concept of stability," in *Buckling and Postbuckling of Beams. Plates, and Shells*. Springer, 2017, pp. 1–6.